A NOVEL SHAPE MEMORY BEHAVIOR OF SINGLE-CRYSTALLINE METAL NANOWIRES

A Dissertation
Presented to
The Academic Faculty

by

Wuwei Liang

In Partial Fulfillment
of the Requirements for the Degree
Doctor of Philosophy in the
School of Mechanical Engineering

Georgia Institute of Technology
December, 2006

A NOVEL SHAPE MEMORY BEHAVIOR OF SINGLE-CRYSTALLINE METAL NANOWIRES

Approved by:

Dr. Min Zhou, Advisor
School of Mechanical Engineering
Georgia Institute of Technology

Dr. David L. McDowell
School of Mechanical Engineering
Georgia Institute of Technology

Dr. Jianmin Qu
School of Mechanical Engineering
Georgia Institute of Technology

Dr. Christopher S. Lynch
School of Mechanical Engineering
Georgia Institute of Technology

Dr. Karl I. Jacob
School of Polymer, Textile & Fiber
Engineering
Georgia Institute of Technology

Dr. David J. Srolovitz
Yeshiva College
Yeshiva University

Date Approved: July 12, 2006

To my wife, Yuqing, and my son, little Peter

ACKNOWLEDGEMENTS

I sincerely thank my advisor, Dr. Min Zhou, for his consistent support, guidance, understanding, and patience during my Ph.D. study. He was always there to listen and to give advice.

I also wish to thank my committee members, Dr. David McDowell, Dr. David Srolovitz, Dr. Christopher Lynch, Dr. Jianmin Qu, and Dr. Karl Jacob for reviewing my work and giving insightful comments. I would also like to thank Dr. Ken Gall and Dr. Ting Zhu for helpful discussions on my research.

My thanks also go to my wonderful friends and colleagues, Douglas Spearot, Vikas Tomar, Ambarish Kulkarni, Mahesh Shenoy, Remi Dingreville, Mark Tschopp, Nitin Patel, Jim Shepherd, and many other friends. Without their help and friendship, my research would not have progressed so well and my life would not have been as enjoyable as it has been.

TABLE OF CONTENTS

LIST OF TABLES

LIST OF FIGURES

SUMMARY

As functional nano building blocks, nanowires are of great technical importance because of their unique structures, properties, and potential applications in nanoscale electronic, photonic, biological, and chemical devices. These applications require a fundamental understanding of the structural characteristics and thermomechanical properties of nanowires.

This research focuses on the characterization of the structure and mechanical behavior of metal nanowires. To this end, molecular dynamics simulations with embedded-atom method (EAM) potentials are used. A novel shape memory effect and pseudoelastic behavior of single-crystalline FCC metal (Cu, Ni, and Au) nanowires are discovered. Specifically, upon tensile loading and unloading, these wires can recover elongations of up to 50%, well beyond the recoverable strains of 5-8% typical for most bulk shape memory alloys. This novel behavior arises from a reversible lattice reorientation driven by the high surface-stress-induced internal stresses at the nanoscale. It exists over a wide range of temperature and is associated with response times on the order of nanoseconds, making the nanowires attractive functional components for a new generation of biosensors, transducers, and interconnects in nano-electromechanical systems.

It is found that this novel shape memory behavior only exists at the nanometer scale but not in bulk metals. The reason is that only at the nanoscale is the surface-stress-induced driving force large enough to initiate the transformation. This size-dependence also explains why this novel behavior has not been discovered before, since extensive research on nanowires just started about one decade ago. The lattice reorientation process is also temperature-dependent because thermal energy facilitates the overcoming of the energy barrier for the transformation. Therefore, nanowires show either pseudoelasticity

or shape memory effect depending on whether the transformation is induced by unloading or heating. It is also found that not all FCC nanowires show shape memory behavior. Only FCC metals with higher tendency for twinning (such as Cu, Au, Ni) show the shape memory because twinning leads to the reversible lattice reorientation. On the other hand, FCC metals with low likelihood of twinning (such as Al) do not show shape memory because these wires deforms via crystal slip, which leads to irreversible deformation.

A micromechanical continuum model is developed to characterize the shape memory behavior observed. This model treats the lattice reorientation process as a smooth transition between a series of phase-equilibrium states superimposed with a dissipative twin boundary propagation process. This model captures the major characteristics of the unique behavior due to lattice reorientation and accounts for the size and temperature effects, yielding results which are in excellent agreement with the results of molecular dynamics simulations.

CHAPTER 1 INTRODUCTION

As functional nano building blocks, nanowires are of great technical importance because of their unique structures, properties, and potential applications in nanoscale electronics, photonics, biological or chemical sensors (Lieber 2003; Patolsky and Lieber 2005). In recent years, various nanocomponents have been developed from nanowires, such as nanolasers (Huang et al. 2001; Duan et al. 2003a), Field-effect transistors (FET) (Arnold et al. 2003; Wu et al. 2004), light emitting diodes (LED) (Duan et al. 2003b), and quantized conductance atomic switch (Terabe et al. 2005). Nanowire sensors have also been fabricated for highly sensitive and selective detection of biological and chemical species such as hydrogen (Walter et al. 2002), CO and NO2 gases (Comini et al. 2002), proteins, and DNA (Cui et al. 2001). These nanowires components have even been integrated as address decoders for nanosystems such as biological sensor arrays and nanocomputers (Zhong et al. 2003). Among all nanowires, metal nanowires have drawn a lot of interest because of their appealing properties such as high thermal and electrical conductivity, and quantized conductance (Landman et al. 1990; Stalder and Durig 1995). Particularly, metal nanowires are seen as a promising alternative to build electronic chips to solve the looming crisis in computing technologies as current fabrication methods of silicon wafer etching will fail well before the size of electronic components reaches atomic dimensions (Yang 2002). New logic gates such as crossbar latches recently built from Pt nanowires are expected to replace the transistor, the fundamental building block of all contemporary computing and electronics (Kuekes et al. 2005). Such development could lead to a major revolution in the electronics industry dominated by semiconducting materials.

The application of nanowires requires a fundamental understanding of the structural characteristics and thermomechanical properties, which is critical to the

fabrication, assembling, and functioning of nanowires. For example, nanowires often need to sustain drastic temperature changes and high thermo-stresses in fabrication processes such as chemical-electrical deposition or electron/ion lithography (Kondo and Takayanagi 2000; Konishi et al. 2003). Large mechanical or thermal stresses may be induced under working conditions as nanowire components are often assembled between substrates to form junctions and arrays (Zhong et al. 2003). In the past few years, significant progresses have been made in experimental, theoretical, and computational study of the structures and properties of nanowires. Single-atom chains, helical spiral strands, helical and cylindrical multi-shell structures, and crystalline wire structures have been observed in atomistic simulations and experiments (Wang et al. 2001; Rodrigues and Ugarte 2003). Because of the strong surface effect, unique behaviors such as surface-stress-induced phase transformation (Diao et al. 2003), lattice reorientation (Kondo and Takayanagi 1997; Diao et al. 2004) have also been observed.

This research focuses on the characterization of the structure and mechanical behavior of metal (Cu, Ni, Au, and Al) nanowires using molecular dynamics (MD) simulations with EAM interatomic potentials (Mishin et al. 1999; Mishin et al. 2001; Foiles 2005). We discovered a novel shape memory behavior in single-crystalline metal (Cu, Ni, and Au) nanowires. Nonexistent in the bulk form of metals, the behavior is associated with a reversible lattice reorientation driven by the high surface-stress-induced internal stresses at the nanoscale. Under tensile loading and unloading, the nanowires exhibit recoverable strains up to over 50%, well beyond the typical recoverable strains of 5-8% for most bulk shape memory alloys (SMAs) (Otsuka and Kakeshita 2002). The temperature-dependence of this behavior leads to a shape memory effect (SME). Moreover, the nanowires have very short response times which are on the order of nanoseconds due to their extremely small dimensions compared with bulk SMAs. These unique properties can lead to important applications at the nanoscale, including sensors, transducers, and actuators in nano-electromechanical systems (NEMS) (Gilbertson and

Busch 1996; Clements 2003; Lu and Panchapakesan 2004; Otsuka and Kakeshita February 2002).

The first part of this research focuses on the nanowire structure and stability because the novel SME is primarily derived from the unique 1D structure and high surface-to-volume ratios of nanowires. The stability of wire structures is significantly affected by axis orientations and surface types because surface energy constitutes a significant portion of the total free energy of nanowires. Structural transformation may occur between wire structures with different stabilities. It is important to obtain realistic wire structures to investigate the thermomechanical behavior. To this end, the wires are created by simulating the "top-down" fabrication of wires. Specifically, wires with <100> axis and {100} lateral surfaces are isolated from perfect bulk lattices and are allowed to relax at a constant temperature. Structural transformation occurs during relaxation, and the resulting free standing nanowires have <110> axis and {111} surfaces. This resulting structure represents a low energy state and has been frequently observed in experiments and MD simulations.

The second part concerns the response of metal nanowires to the quasistatic tensile loading and unloading. Three types of responses are observed. Specifically, Cu and Ni wires exhibit a shape memory behavior with large reversible strains of up to 50%. In comparison, the tensile deformations of Al wires are irreversible upon unloading. Au wires show a transition of behavior from pseudoelasticity at low temperatures to plasticity at high temperatures. The analysis here focuses on the deformation mechanism, driving force, and critical temperature for this SME, with a particular emphasis on the role of generalized stacking fault energies in determining the existence of the pseudoelastic behavior. Specifically, an explanation as to why this behavior is observed in some FCC metals (e.g., Cu, Au, Ni) but not in others (such as Al) is given. It is

observed that FCC metals showing this effect share the common attribute of having high twinnability, a parameter identified by (Tadmor and Hai 2003) for quantifying the tendency to form twins in FCC metals. The effect of wire size is discussed and the reason why this phenomenon exists only in nanowires but not in bulk single crystals of the same FCC metals is pointed out.

The third part focuses on the development of a micromechanical continuum model for the unique stress-strain behavior due to the lattice reorientation. Since the lattice reorientation is a dissipative process even under quasistatic loading conditions, this model treats the process as a reversible smooth transition between phase-equilibrium (metastable) states superimposed with an irreversible, energy-dissipating twin boundary propagation process. Specifically, the reversible smooth transition between phase-equilibrium states is modeled within the framework of strain energy function with multiple local minima (Abeyaratne et al. 2001). Detailed analysis of the dissipative twin boundary propagation shows that the energy dissipation results from the ruggedness of strain energy landscape associated with dislocation nucleation, gliding, and annihilation during lattice reorientation. The model captures the major characteristics of the unique behavior due to the lattice reorientation and accounts for the size and temperature effects. The model predictions show excellent agreement with the results of MD simulations.

The organization of this thesis is as follows. Chapter 2 briefly reviews the relevant topics such as nanowire structures, surface-stress-induced structural reconstruction, the transformation mechanisms and constitutive modeling of SME in bulk SMAs. Chapter 3 describes the MD computational framework used in this research including EAM potentials and their calibration, structural analysis techniques, and the quasistatic loading scheme. Chapter 4 concerns the nanowire structure and the lattice reorientation under a top-down fabrication process. The mechanical behaviors of nanowires are investigated in chapter 5. The focus is on the characterization of the novel shape memory behavior in

nanowires including the transformation mechanism, driving force, energy barrier, the quantification of the large reversible strains, and size and temperature effects. Based on the results of MD simulations and the analysis of deformation mechanisms, a micromechanical continuum model is developed in Chapter 6 to characterize the unique lattice reorientation process. Finally, the thesis is concluded with conclusions and recommendations for future research in chapter 7.

CHAPTER 2 BACKGROUND

Until recently, SME and pseudoelastic behaviors are usually considered unique to shape memory alloys, liquid crystal elastomers, and piezoelectric ceramics (Otsuka and Wayman 1998). In this research, a novel shape memory behavior is discovered in single-crystalline FCC metal nanowires. The novel behavior arises from reversible lattice reorientations through twin boundary propagation. This transformation mechanism is similar to, but not exactly the same as the martensitic transformation, which is responsible for the shape memory behavior in most bulk SMAs. The knowledge of SME in bulk SMAs can help understand the novel SME in nanowires because both behaviors share many common characteristics, such as large reversible strains, temperature-dependent, and diffusionless transformation. Therefore, this chapter briefly reviews the SME in bulk SMAs including the transformation mechanisms and constitutive modeling. Other topics also reviewed include the novel structures of nanowires, structural stability, and lattice reconstructions induced by surface stress, which are closely related to the novel SME in metal nanowires.

2.1 Shape Memory Effect and Pseudoelasticity

SME and pseudoelastic behavior refer to the phenomenon such that a specimen, after being severely deformed, can recover its original configuration through mechanical unloading or heating, respectively (Otsuka and Wayman 1998). The unique properties are usually observed in SMAs such as NiTi, Cu-Zn-Al, and Cu-Al-Ni. They have been used in a wide variety of applications such as transducers, sensors, and actuators. SMAs have also been regarded as smart materials because they can function as sensors and actuators simultaneously (Otsuka and Ren 1999; Otsuka and Kakeshita February 2002). Until recently, the shape memory effect and its underlying pseudoelasticity were considered unique to SMAs, liquid crystal elastomers, and piezoelectric ceramics (Otsuka and

Wayman 1998). More recent research has shown that pseudoelasticity may also be found at the nanoscale, in gold nanowires (Landman et al. 1996) and carbon nanotubes. For example, Yakobson et al. (1996) and Falvo et al. (1997) observed in experiments and atomistic simulations that carbon nanotubes can completely recover from sever deformations with strains up to 15% without inducing residual defects. Bilalbegović (2001) reported that Au nanowires can recover their initial lengths and radii after very large compressive strains. However, irreversible defects are nucleated under even small compressive strains, in contrast to the defect-free processes seen for carbon nanotubes. Landman et al. (1996, 1997) observed reversible changes in structural and electromechanical properties of gold nanowires under tensile loading and unloading. Although the aforementioned reversibility in the deformation of nanowires provides some evidence of pseudoelastic behavior, so far, no systematic research has been done on the SME and pseudoelastic behavior of nanowires regarding the transformation mechanism, constitutive modeling, and the thermomechanical conditions under which the behavior exists.

2.1.1 Martensitic Transformation

The key characteristic of all SMAs is the occurrence of a temperature-dependent martensitic phase transformation, a shear-dominant and diffusionless process through cooperative displacement of atoms in shear variants (Bhadeshia 2001; Bhattacharya et al. 2004; Otsuka and Kakeshita February 2002). Although most martensitic transformations occur in alloys, similar transformations have also been observed in other materials, such as A15 superconducting compounds and Ar-N2 solid solutions (Barrett 1976; Nakanishi 1980). The martensitic transformation is driven by the difference in the chemical free energies between the parent and product phases at a given temperature. The general mechanism of martensitic transformation has been studied from a number of viewpoints. One of the most successful theories is the phenomenological crystallographic theory,

7

developed independently by Lieberman et al. (1995) (the WLR theory) and Bowles and Makenzie (1954a, b) (the BM theory). According to the theory, all crystallographic parameters, such as habit plane, the orientation relationship between parent and martensite, and shape strain (the macroscopic change associated with the transformation), can be predicted from just three input parameters: the lattice parameters of the parent and martensite, the lattice correspondence between parent and martensite, and the lattice invariant shear. Although the theory is quite successful from a critical comparison of the theory with careful experimental results, it tells nothing about the actual paths taken by the atoms during transformation because it treats only the relation between the initial (parent) and final (martensite) states. It can not explain the time-dependence of the martensitic transformation despite that low response speed is a major drawback of SMAs (Shin et al. 2004). In this research, the lattice reorientation in the pseudoelastic behavior and SME of metal nanowires are found to have the diffusionless characteristic of martensitic transformations. In addition to the kinematics, the transformation mechanism is also analyzed in detail in terms of defect nucleation and propagation.

Some SMAs (including Au-Cd, Cu-Zn-Al, and Cu-Al-Ni) exhibit a strange rubber-like behavior without martensitic phase transformation after appropriate ageing (Ölander 1932; Cahn 1995; Ren and Otsuka 1997). While superelastic behavior is associated with martensitic phase transformation, the rubber-like behavior occurs solely in the martensitic state by the reversible movement of twin boundaries (Otsuka and Wayman 1998). This mechanism is very similar to the lattice reorientation responsible for the shape memory behavior because both mechanisms involve twin boundary propagation and the both mechanisms do not change the crystalline structures. However, It is known rubber-like behavior occurs in some bulk SMAs only after being aged for some time in martensitic state, and lattice imperfection is a necessary condition (Ren and Otsuka 1997). By contrast, neither ageing nor lattice imperfection is necessitated in metal nanowires for shape memory behavior.

2.1.2 Constitutive Models for Phase Transformation

Various constitutive models have been proposed to describe the stress-strain-temperature relations of shape memory materials. These models can be classified into three major categories: macroscopic phenomenological models, microscopic thermodynamics models, and micromechanics based macroscopic models.

Macroscopic phenomenological models are built on the basis of thermodynamics through curve-fitting of experimental data. Many are based on the phase diagrams of SMA transformation where the transition regions of martensite to parent phase or parent phase to martensite transformation are determined experimentally and plotted in stress-temperature space. The martensite volume fraction is often defined as an internal state variable (Sato and Tanaka 1988; Liang and Rogers 1990; Ivshin and Pence 1994; Bekker and Brinson 1997). These models are more suitable for engineering applications due to their simplicity and accuracy because the phase diagram is built on experimental data.

Microscopic thermodynamics models use phenomenological thermodynamics to describe an infinitesimal volume in an infinite domain (Abeyaratne and Knowles 1990; Ball and James 1987; Falk 1983). They concentrate on the micro-scale behavior such as nucleation, interface motion, and growth of a martensite phase. Microscopic models are extremely helpful for understanding the phenomenon, but are often too complex to apply for engineering applications.

Micromechanics based macroscopic models use thermodynamics laws to describe the transformation and uses micromechanics to estimate the interaction energy, a key factor in the transformation mechanism (Fischer and Tanaka 1992; Raniecki et al. 1992). Appropriate formulation of this interaction energy is very important and requires knowledge of the micro-structural evolution (Lu and Weng 1997; Huang and Brinson 1998). This class of models is accurate and helpful for understanding the phenomenon by combining the advantages of the first two classes of models.

In micromechanical models, the propagation of individual twin and phase boundaries is of particular interest because it is responsible for the phase transformation for most SMAs. In order to understand the factors that determine the mobility, Abeyaratne and Vedantam (2003b) developed a macroscopic kinetic law for twin boundary motion from a lattice dynamical model. This model is developed for compound and type-1 twins observed in Cu-Al-Ni SMA. It agrees well with experimental observations in predicting that compound twins are 10 times more mobile than type-1 twins. This model is derived for bulk SMAs and it does not consider the surface energy. Therefore, it can not be directly used for the twin boundary motion in nanowires in which surface energy plays a crucial part.

Abeyaratne and Knowles (1993), Abeyaratne and Kim (994), and Abeyaratne and Vedantam (2003) presented a framework for phase transformation based on theory of the strain energy functions with multiple local minima, with each local energy well corresponding to a phase or variant of the material. As the load is varied, the relative stability of each phase changes and the less stable phase transform into the more stable phase through the propagation of the phase boundary. The framework has been successful in modeling the martensitic transformations in bulk SMAs, especially for static problems. However, it is difficult to construct accurate strain energy functions essential for the framework. Moreover, accurate kinetic laws, which determine the relation of the driving force and phase boundary propagating speed, are difficult to obtain because they are determined by many factors which require analysis by lattice-scale models (Abeyaratne and Knowles 1991).

To avoid the difficulties in using the above framework, this research treats the quasistatic lattice reorientation process as a reversible part superimposed with an irreversible part. The reversible part is the smooth transition between a series of phase-equilibrium states, and the irreversible part deals with the dissipative phase boundary propagation process. The reversible part is analyzed using the above framework. Instead

of trying to construct complete strain energy functions, this research only calculate the local strain energy function around the stable states corresponding to the local minima. For the irreversible part, we do not attempt to explicitly calculate the driving force or derive an explicit kinetic law. Instead, we study the source of dissipation by analyzing the lattice scale deformation mechanism, which involves dislocation nucleation, gliding, and annihilation.

2.2 Nanowire Structures

The structural and mechanical properties of metal nanowires represent a fundamental issue for the understanding of various phenomena such as friction, fracture, adhesion, etc. Because nanoscale systems have only a small number of atoms and a significant portion of them are on the surfaces, this may lead to new and interesting mechanical, electrical, magnetic properties, as well as unexpected atomic arrangement and morphologies.

2.2.1 Size-dependence of Nanowire Structures

Various structures of metal nanowires have been observed in MD simulations and experiments (Liang et al. 2003). There is a clear size effect on the wire structure. For metals with FCC crystal structures, FCC crystalline structure represents a low-energy packing for bulk. Therefore, crystalline wires clearly prevail for large wires where most atoms are internal atoms. For very small wires, surface energies dominate the total free energy. Hence, weird structures make their appearance such that the surface energy is minimized. Overall, as the wire size increases, the metal wire morphologies primarily change from single-atom chains to helical spiral strands, helical and cylindrical multi-shell structures, and FCC crystalline structures.

So far, the thinnest metal wires are gold single-atom chains (Ohnishi et al. 1998; Yanson et al. 1998; Rubio-Bollinger et al. 2001). These single-atom chains are usually

formed between a scanning tunneling microscope (STM) tip and a gold substrate by driving the tip into the substrate and then retracting the tip. This structure is not of low energy state and can only exist under external tensile loading. At low temperatures, these wires can be as long as 5 atoms and is stable for a few seconds. At natural state without external load, atomistic simulations have predicted that helical spiral strands for the ultra thin metal wires such as Au (Wang et al. 2001), Pb, and Al wires (Gülseren et al. 1998). Usually, the critical lateral size for such structure is on the order of 2 or 3 lattice constants. At this size, more atoms are located on surfaces than in the core (or "bulk"). The "bulk" packing in this structure is not very good, but the surface packing is excellent (Gülseren et al. 1998). As the wire size increases, helical and cylindrical multi-shell structures make their appearance for metal nanowires such as Cu (Kang and Hwang 2002; Kang et al. 2002), Au (Bilalbegović 1998, 2000; Kondo and Takayanagi 2000; Wang et al. 2001), and Al nanowires (Gülseren et al. 1998). The critical size range for such structures is between 0.6 nm and 2.2 nm for Au nanowires (Wang et al. 2001). When the wire size further increases to a point where there are significantly more internal (bulk) atoms than surface atoms, FCC crystalline structures become dominant for metal nanowires such as Cu, Ag, and Au wires (Hong et al. 2001; Gao et al. 2002; Iijima and Qin 2002). Wang et al. (2001) found that Au wires with diameter greater than 3.0 nm are crystalline.

2.2.2 Surface-stress Induced Structural Reconstruction

The surface energy of nanowires constitutes a significant portion of the total free energy because of their extremely high surface-to-volume ratios compared to bulk materials. For example, the surface-to-volume ratio of a nanowire with a diameter of 4 nm is 10^6 times that of the typical macroscopic tensile specimen with a diameter of 4 mm. Therefore, crystalline metal nanowires tend to assume axes and surfaces in preferred orientations to lower the total energy. It has been observed that most metal wires have

{111} and {100} surfaces and axes in <111>, <001>, or <110> directions (Rodrigues and Ugarte 2002; González et al. 2004). Specifically, metal wires with <110> axes and {111} surfaces have been most frequently observed in experiments (Wang et al. 2000; Rodrigues et al. 2002; Liu and Bando 2003; Liu et al. 2003; Wang et al. 2004c) and atomistic simulations (Diao et al. 2004; Wang et al. 2004a; Liang and Zhou 2005). This configuration is more stable because it represents a lower energy state for FCC metal nanowires.

Due to the strong orientation preferences, lattice reconstruction or reorientation may occur in metal wires if the initial configurations do not have the preferred orientations when fabricated via a top-down approach. The lattice reconstruction usually causes high energy surfaces to reorganize into lower energy surfaces, e.g. from {110} to {001} surfaces (Wang et al. 2000), or from {001} to {111} surfaces (Kondo and Takayanagi 1997). According to Diao et al. (2003) and Gall et al. (2004), the driving force for the lattice reconstruction comes from surface-stress-induced internal compressive stress σ. It is worth pointing out that surface stress in this research is defined as the derivative of surface free energy w.r.t strain. Diao et al. (2003, 2004) quantified the effect of the surface stress. For wires with a square cross-section, the axial compressive stress due to surface stress is $\sigma = 4fd/d^2 = 4f/d$, where f is the axial component of the surface-stress as calculated by Streitz et al. (1994), and d is the side length of the cross-section. Obviously, σ increases as the wire size decreases and can be very high in small wires. For example, $\sigma = 5.95$ GPa in a 1.83×1.83 nm Au nanowire with the BCT crystalline structure (Diao et al. 2003). Such a high stress level can induce structural transformations, leading to a reduction in the system energy. Therefore, lattice reconstruction or reorientation is size-dependent and only occurs in wires below a critical size (Diao et al. 2004; Gall et al. 2004). For example, Kondo et al. (1999) discovered that the surfaces of Au nanofilms change from (100) into (111) when film thickness is decreased to less than eight atomic layers (Kondo et al. 1999). In addition, Kondo and

Takayanagi (1997) found that Au nanowires with <001> axes cut from (100) films whose thickness is smaller than 2 nm reconstruct into hexagonal prism shapes with <110> axes and {111} lateral surfaces. Such reconstructions do not occur when the thickness of the Au films is larger than the above values. Diao et al. (2003) observed a similar process in atomistic simulations. Specifically, when the cross-sectional areas are equal to or less than 1.83×1.83 nm, Au nanowires with initial face-centered-cubic (FCC) structures and <100> axes reorganize spontaneously into body-centered-tetragonal (BCT) structures.

On one hand, structural changes present a challenge for controlling the morphologies and dimensions of nanowires during the fabrication process. On the other hand, they also provide an important mechanism behind many attractive properties of nanowires. In order to obtain nanowires with desired properties, morphologies, and dimensions, it is important to understand the mechanisms and quantify the effects of the structural changes in the top-down fabrication process. The characterization of the structural changes also allows the behavior of the nanowires to be quantified.

CHAPTER 3 MOLECULAR DYNAMICS COMPUTATIONAL FRAMEWORK

At the nanoscale, there are many practical difficulties in experimental study of the structures, properties and behaviors of nanowires. Although today's cutting-edge high-resolution transmission electron microscope (HRTEM) can resolve individual atoms, the real 3D structures are often inferred based on many 2D images through tedious try-and-error methods. Particularly, it is extremely difficult to experimentally monitor the real-time evolution of nanostructures during dynamic deformations. However, in MD simulations, the structure and defect evolution can be easily captured by tracking the movement of individual atoms. Moreover, MD simulations can predict the structures and behaviors of nanostructured materials even before they are actually fabricated. The computational findings can provide useful information for interpreting experimental results and help to design experiments to study the behavior of nanowires in specific directions.

This research uses MD simulations to characterize the structure and mechanical behavior of metal nanowires. The parallel MD code WARP developed by Plimpton (1995) is used to carry out the computations. This code offers excellent scalability by using spatial-domain decomposition and a fast link-cell algorithm to build neighbor lists. EAM interatomic potentials are chosen for metal systems including Cu, Ni, Al (Mishin et al. 1999; Mishin et al. 2001), and Au (Foiles 2005). The Graphics package visual molecular dynamics (VMD) is used to visualize the simulation results (Humphrey et al. 1996). All computations are carried out at NAVO HPCRC, ERDC, and ARL MSRCs high performance computing centers.

This chapter discusses some important aspects of the MD simulation framework including interatomic potentials and their calibration, calculations of generalized stacking fault energies, structural analysis techniques, and quasistatic loading scheme.

3.1 EAM Potentials and Their Calibration

The validity and accuracy of MD simulation results are primarily determined by the accuracy of the interatomic potentials. In this research, EAM interatomic potentials are selected because of their proven successes in simulating simple FCC metals. Specifically, the EAM potentials for Cu, Ni, and Al are developed by Mishin et al. (1999, 2001), and the potential for Au is developed by Foiles (2005), c.f., (Park and Zimmerman 2005). The selected potentials predict accurate surface energies and generalized stacking fault energies (Zimmerman et al. 2000), which are critical for the novel SME in metal nanowires.

EAM is a semi-empirical many-body potential model first proposed by Daw and Baskes (1984). It is loosely based on the local density functional theory, and the parameters are fit to the experimental values of bulk properties and sometimes, properties of the defects. It has been applied successfully to bulk and nanostructured problems in simple close-packed metals (e.g. Cu, Au), such as phonons, thermodynamic functions and melting point, defects, grain boundary structures, surface structures, surface order-disorder transitions (Daw et al. 1993). One major appealing aspect of the EAM is its physical picture of metal bonding. In this method, each atom is embedded into the local electron density provided by it neighboring atoms. In this way, the embedding function incorporates important many-body interactions. Moreover, there are electrostatic interactions between atoms. The functional form of the total energy is given by

$$E = \sum_i F_i \left(\sum_{j(\neq i)} \rho_j^a \left(\mathbf{r}_{ij} \right) \right) + \frac{1}{2} \sum_{\substack{i,j \\ (j \neq i)}} \phi_{ij} \left(\mathbf{r}_{ij} \right) \tag{3.1}$$

where i refers to the atom in question and j refers to a neighboring atom. F is the embedding energy, ρ^a is the spherically averaged atomic density, and ϕ is an electrostatic, two-body interaction. $\mathbf{r}_{ij}$ is distance between atoms i and j.

In choosing the EAM potentials, special attention is placed on the surface energies and the generalized stacking fault energy (GSFE) because of their important roles in the deformation mechanisms responsible for the shape memory behavior in nanowires. Specifically, the surface energies constitute a significant portion of the total free energy and greatly affect the relative stability of nanowires. The surface energies predicted by the selected EAM potentials are reasonably accurate compared to experimental results and Density Function Theory (DFT) calculations, as shown in Table 3.1.

Table 3.1 Comparison of the surface energies of EAM potentials for Cu, Au, Ni, and Al with experimental and DFT calculation results

	{111}		{100}		{110}		Experimental
	EAM	DFT	EAM	DFT	EAM	DFT	average
Cu	1239	1300[a]	1345	1450[a]	1475	1530[a]	1790
Al	870	810[b]	943	890[b,f]	1006	1050[b]	980
Ni	1629		1878		2049		2280
Au	1090	1040[c]	1180	1444[d]	1309	1700[e]	

[a](Gross 2003), [b](Ooi 2005), [c](Vitos et al. 1998), [d](Takeuchi et al. 1991), [e](Fiorentini et al. 1993), [f](Siegel et al. 2001)

As will be discussed in chapter 5, whether a metal nanowire exhibits SME or not is primarily determined by the competition of the nucleation of dislocations or microtwins, which is primarily determined by the generalized stacking fault energies (GSFE) including the stable stacking fault energy (γ_{sf}), the unstable stacking fault energy (γ_{us}), and the unstable twinning energy (γ_{ut})(Zimmerman et al. 2000; Swygenhoven et al. 2004). Rice (1992) has shown that γ_{us} is an important parameter in the characterization of dislocation emission. Tadmor and Hai (2003) and Swygenhoven et

al. (2004) have demonstrated that the ratios of γ_{sf}/γ_{us} and γ_{us}/γ_{ut} are critical in determining whether deformation occurs via slip or twinning. Since some older EAM potentials have been known to provide relatively poor approximations of γ_{sf} of FCC metals, it is important to point out that the γ_{sf} predicted by the EAM potentials used in our current analysis are in excellent agreement with experimental measurements or the results of first-principle calculations, as shown in Table 3.2.

Table 3.2 Comparison of generalized stacking fault energies with experiments and DFT calculations

	γ_{sf} (mJm^{-2})		γ_{us} (mJm^{-2})	γ_{ut} (mJm^{-2})	γ_{sf}/γ_{us}	γ_{us}/γ_{ut}	Twinnability τ_a	d_{sep} (nm)	Behavior
	EAM	Experiments	EAM	EAM	EAM	EAM	EAM		
Cu	45	45[a]	180	202	0.249	0.896	1.040	4	PE[*] & SME
Ni	125	125[b]	402	460	0.317	0.878	1.020	0.7	PE
Au	31	32[c]	101	122	0.307	0.828	0.991	10	Transitional
Al	146	120-166 [d, e]	189	240	0.836	0.788	0.896	0.3	Irreversible

[a](Carter and Ray 1977), [b](Balluffi 1978), [c](Stobbs and Sworn 1971), [d](Murr 1975), [e](Westmacott and Peck 1971; Rautioaho 1982), PE[*]—Pseudoelasticity

3.2 Calculation of Generalized Stacking Fault Energies

While γ_{sf} can be experimentally measured, there are no currently available experimental methods to measure γ_{us} and γ_{ut} directly. Therefore, γ_{us} and γ_{ut} is usually obtained from GSFE curves through MD or first principle calculations. GSFE curves represent the continuous energy cost of rigidly shifting two semi-infinite blocks of crystals on a (111) plane in the [11$\bar{2}$] direction (Zimmerman et al. 2000; Swygenhoven et al. 2004). Specifically, the simulation geometry is shown in Figure 3.1(a). A single, rigid block of atoms is oriented with faces in the <110>, <111>, and <112> directions. Periodic boundary conditions are applied in the <110> and <112> directions. The block is then sectioned between two between {111} planes. Note that the gap shown between the two blocks in Figure 3.1(a) is only for clarity. We do not artificially introduce a gap

into the energy calculation — the undeformed configuration is the bulk lattice. A shear displacement is applied to the top block of atoms in the [112] direction, while the bottom block remains stationary during the simulation. The GSFE curve is the excessive energy per unit cross-sectional area of the shearing plane plotted against the shearing displacement. γ_{us} is defined as the maximum value on the GSFE curve. γ_{sf} is the local minimum between the two γ_{us} peaks. Figure 3.1(c) illustrates the variation of the lattice configurations during the shearing process.
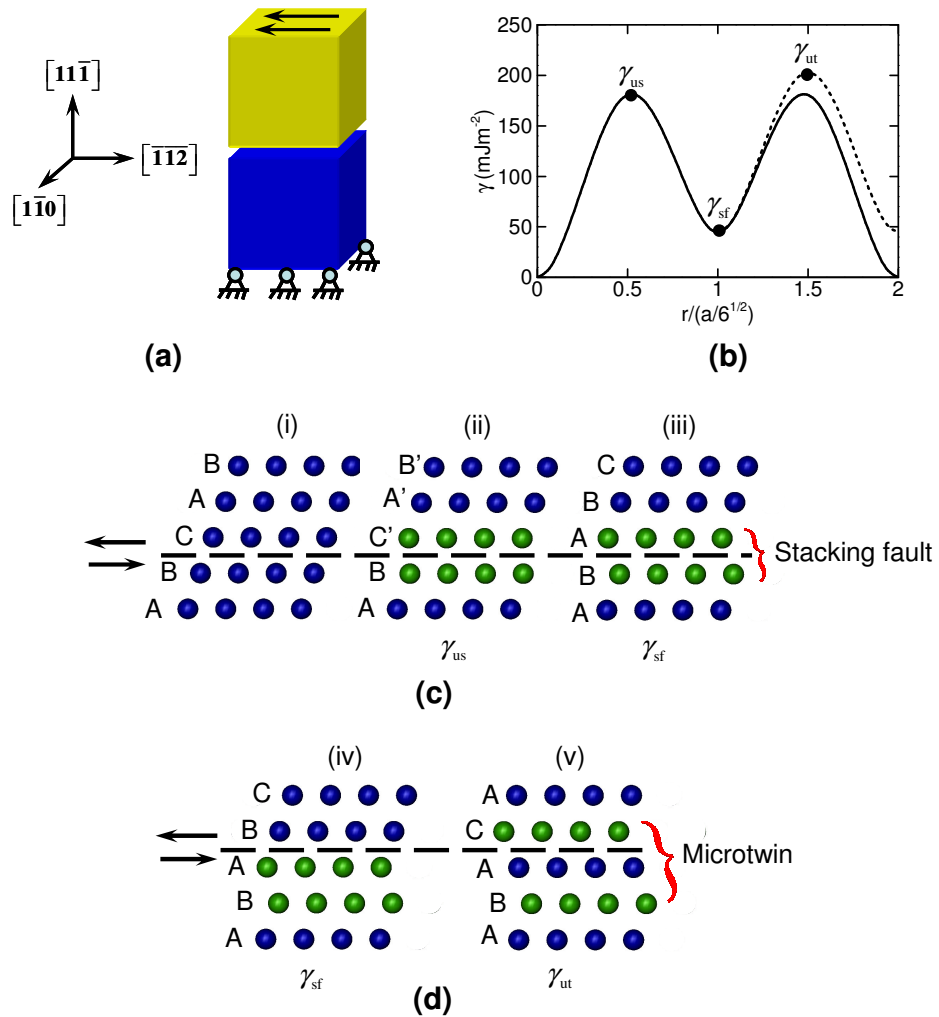
Figure 3.1 Calculation of GSFE, (a) the geometry to calculate GSFE curves, (b) a typical GSFE curve, (c) the change of lattice stacking sequences during shearing process: (i) the

initial undeformed bulk lattice with normal stacking sequence for FCC crystals, ABCABC…, (ii) the lattice stacking sequence corresponding to the unstable stacking fault energy, (iii) the lattice stacking sequence with a stable stacking fault, (d) the change of lattice stacking sequences for calculation of unstable twinning energy, (iv) the initial stacking sequence with a stable stacking fault, the same as configuration (iii) except the shearing plane is one layer up, (v) the lattice stacking sequence with a microtwin.
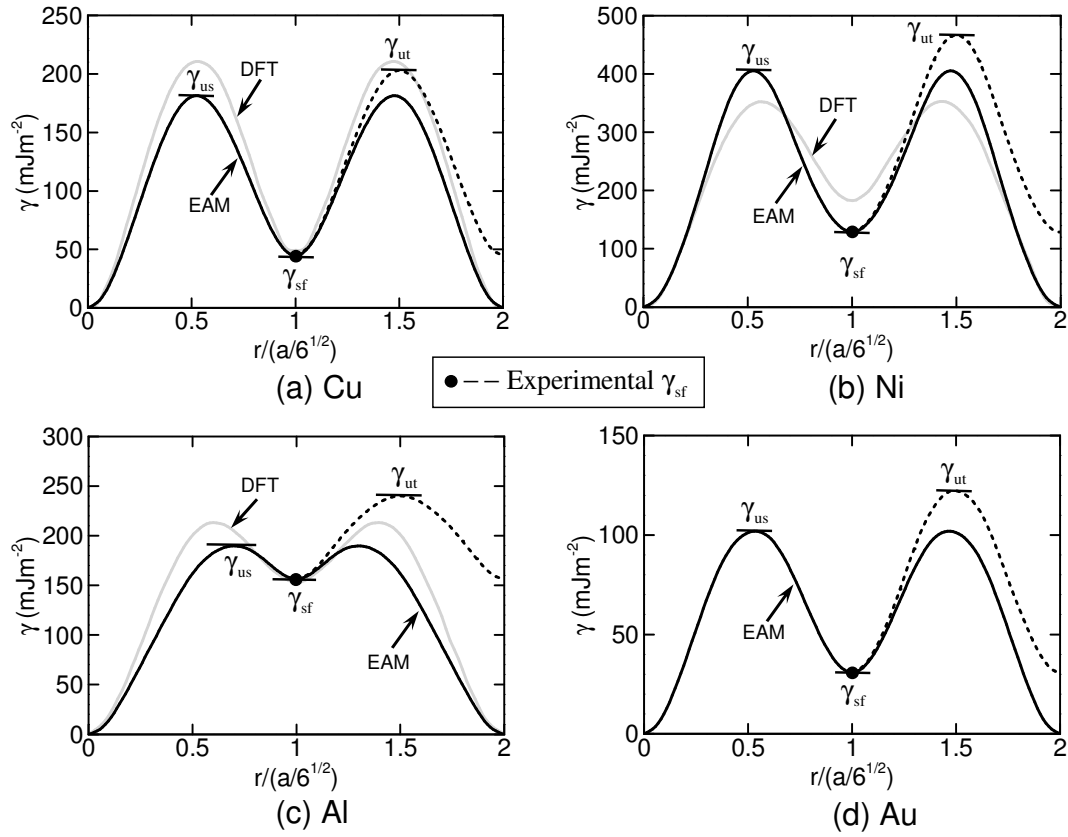
Figure 3.2 GSFE curves of Cu, Ni, Al, and Au. The DFT data is from (Zimmerman et al. 2000).

Similar to γ_{us}, γ_{ut} characterizes the energy barrier for creating a micro-twin, or a defect in the form of a new extrinsic stacking fault by shifting a layer adjacent to an existing intrinsic stacking fault. Specifically, Figure 3.1(d) illustrates the lattice configurations during the shearing process. Note that the initial configuration has an existing stacking fault generated in the preceding shearing process, and the shearing

plane is one-layer above the shearing plane in the preceding shearing process in Figure 3.1(c). The energy variation associated with this process is shown by the dotted lines in Figure 3.2 and γ_{ut} is the maximum value on the dotted curve (Tadmor and Hai 2003; Tadmor and Bernstein 2004).

Figure 3.2 compares the GSFE curves calculated using the EAM potentials with those DFT calculations. Obviously, the GSFE curves predicted by the EAM potentials are in good agreement with the results of DFT calculations. The comparison for Au is incomplete because no DFT results are available.

3.3 Structural Analysis Techniques

Two structure techniques are used to investigate the structures of nanowires, radial distribution function (RDF) to identify overall lattice type and centrosymmetry to identify local structural defects.
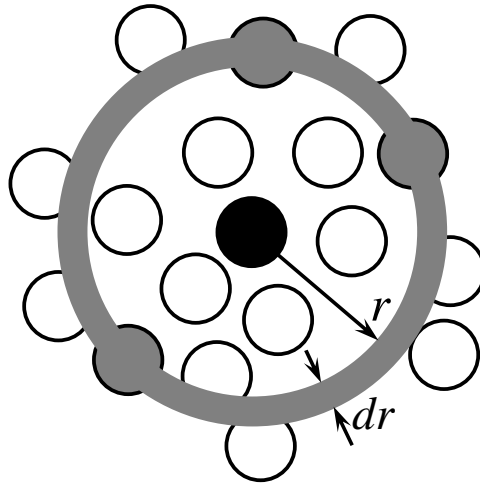
Figure 3.3 A schematic illustration of the RDF, the black atom at the center is the reference atom, and the circles around it represent the other atoms. A ring centered on the reference is drawn with radius r and thickness dr, in this example three other atoms are positioned within this ring and are colored grey.

3.3.1 Radial Distribution Function

Various forms of structural changes or phase transformations have been observed in nanowires. For example, metal nanowire structures change from non-crystalline to FCC crystalline as the lateral size increases. At ultra high strain rates, nanowire structures transform from a crystalline state to an amorphous state. Therefore, it is very important to identify wire structures to characterize nanowire behavior. In this research, radial distribution function (RDF) is chosen for this purpose.

RDF describes fluctuations in density around a given atom. It can also be considered as the average number of atoms found at a given distance in all directions. For an atomistic system, the RDF g(r) is determined from (Gutie´rrez and Johansson 2002),

$$g(r) = \frac{\langle n(r, r+dr) \rangle}{4\pi r^2 dr} \frac{V}{N}. \tag{3.2}$$

Here, $n(r, r+dr)$ denotes the average number of atoms surrounding the center atom in a spherical shell between r and $r+dr$, N is the total number of atoms in the system, and V is the volume of system, as shown in Figure 3.3. The RDF of a liquid is usually smooth and fluctuates around 1 after the first large peak. The RDF of a solid has many sharp peaks with the RDF going to zero between them. By analyzing the pattern of peaks, not only can RDF tell if a structure is crystalline or not, but also what type of crystalline structures it is (e.g., FCC or HCP). Furthermore, the RDF can be measured experimentally using neutron-scattering techniques, makes it possible to correlate simulations with experimental results.

3.3.2 Centrosymmetry

Although RDF is good to identify the overall average structure, it is not appropriate for identifying local structure changes or structural defects, which is very important to investigate the mechanisms in plastic deformations or phase transformations. There are several techniques to separate the defects from the extensive deformation, for

example, techniques relying on the electron density, the potential energy, the dislocation density tensor, or the atomic level stress tensor. Kelchner et al. (1998) used a parameter called centrosymmetry to identify defects. This technique is based on the fact that a centrosymmetric material (such as Cu or other FCC metals) will remain centrosymmetric under homogeneous elastic deformation. In centrosymmetric material, each atom has pairs of equal and opposite bonds to its nearest neighbors. As the material is distorted, these bonds will change direction and/or length, but they will remain equal and opposite. When a defect is introduced nearby, this equal and opposite relation no longer holds for all of the nearest neighbor pairs.
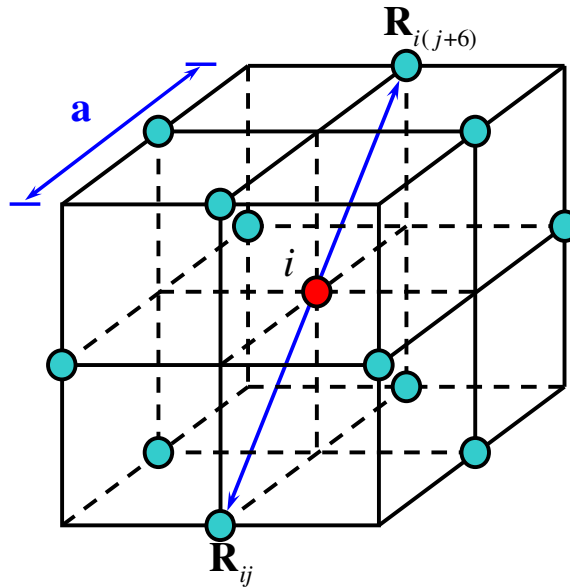
Figure 3.4 A Schematic illustration of a unit cell of centrosymmetric materials

The centrosymmetry is defined by

$$P = \sum_{i=1,6} \left| \mathbf{R}_i + \mathbf{R}_{i+6} \right|^2 \tag{3.3}$$

where $\mathbf{R}_i$ and $\mathbf{R}_{i+6}$ are the vectors or bonds corresponding to the six pairs of opposite neighbors in the FCC lattice, as shown in Figure 3.4. Centrosymmetry is zero for

homogeneous elastic deformation but nonzero for any plastic deformation of the material. In the above definition, the value of centrosymmetry depends on not only the amount of the plastic deformation but also the lattice constant, which is different from material to material. In this research, we normalize the centrosymmetry by the lattice constant, i.e.

$$C = \sqrt{P}\big/a \qquad (3.4)$$

where P is centrosymmetry defined by equation (3.3), a is the crystal lattice constant. The normalized centrosymmetry C only depends on the amount of plastic deformation, while is independent of the type of materials.

3.4 Displacement-controlled Quasistatic Loading Scheme

So far, the strain rates considered in MD simulations (at or above 10^7 s^{-1}) are much higher than what can be obtained in controlled experiments. These artificially high strain rates are, to a degree, necessitated by the speed of computers available. The time scale that can be reached in many simulations is of the order of 100 nanoseconds, partly limited by the time step size needed to resolve the high frequency thermal vibrations of atoms in MD calculations which is of the order of 1 femtosecond. To achieve significant deformation within such a short time, high strain rates are needed. High deformation rates cause rapid and extremely high temperature increases, sometimes causing shear localization (Ikeda et al. 1999). It should be noted that this is purely a computational necessity and is not part of any realistic physical deformation process. Therefore, special algorithms are needed to allow physically interpretable results to be obtained using available computer resources and to avoid the artificially high rates of deformation.

To this end, we use a displacement-controlled quasistatic loading and unloading scheme introduced by Gall et al. (2004). In this method, the nanowires are relaxed to reach equilibrium states between loading steps. Hence, the deformation proceeds through a series of equilibrium states, which essentially simulates a quasistatic process. Specifically, in each load step, all the atoms are first displaced according to a prescribed uniform strain increment of $\Delta\varepsilon = 0.125\%$ in the length direction, as shown in Figure 3.5. This proportional scaling of atom coordinates in the axial direction is carried out to all atoms, no matter the atom is involved in defects or not. The wires are then equilibrated with their ends fixed at constant temperature for 15 picoseconds (ps) to obtain a macroscopic equilibrium configuration at

Figure 3.5 Displacement-controlled quasistatic loading scheme for a nanowire, the blue atoms on both ends are boundary atoms, which are held fixed during relaxation between loading steps.

the prescribed strain. This relaxation process allows structural changes to occur, if the conditions so dictate. This process usually takes less than 12 ps and the average stress over the last 3 ps of the relaxation period at each load step is taken as the stress in the wire at the current strain. Unloading is implemented in the same manner, with a negative strain increment of $\Delta\varepsilon = -0.125\%$. The results from the quasistatic loading and unloading method are compared with those from dynamic and static simulations. It is

found that as long as the maximum atom displacement is less than $0.2a$ (where a is the lattice constant), this quasistatic method does not artificially affect deformation mechanisms.

CHAPTER 4 STRUCTURES OF NANOWIRES AND STRUCTURAL RECONSTRUCTION

Since the surface energy constitutes a significant portion of the total free energy, metal nanowires tend to assume surfaces in specific orientations to lower the total surface energy. Lattice reconstruction or reorientation may occur in wires fabricated via top-down approach if the initial configurations do not have the preferred orientations (Kondo and Takayanagi 1997; Wang et al. 2000). On one hand, structural changes present a challenge for controlling the morphologies and dimensions of nanowires during the fabrication process. On the other hand, they also provide an important mechanism behind many attractive properties of nanowires. In order to obtain nanowires with desired properties, morphologies, and dimensions, it is important to understand the mechanisms and quantify the structural changes in the top-down fabrication process. The characterization of the structural changes also allows the behavior of the nanowires to be quantified.

In this research, realistic wires structures are generated by simulating a "top-down" fabrication process of wires. Specifically, wires with <100> axis and {100} surfaces (hereafter called <100>/{100} wire structure or configuration) are isolated from perfect bulk lattices and are allowed to relax at a constant temperature. During relaxation, lattice reconstruction occurs and {100} surfaces reorganize into lower-energy {111} surfaces. Meanwhile, the <100> axis reorients into a new <110> direction. The resulting free standing nanowires have <110> axis and {111} surfaces (hereafter called <110>/{111} wire structure or configuration). This new structure represents a low energy state and has been frequently observed in experiments and MD simulations. The deformations during the relaxation are also quantified by a phenomenological continuum

approach and a crystallographic in the next chapter. The discussions here focus on Cu nanowires, but similar behavior is also found in Ni and Au wires.
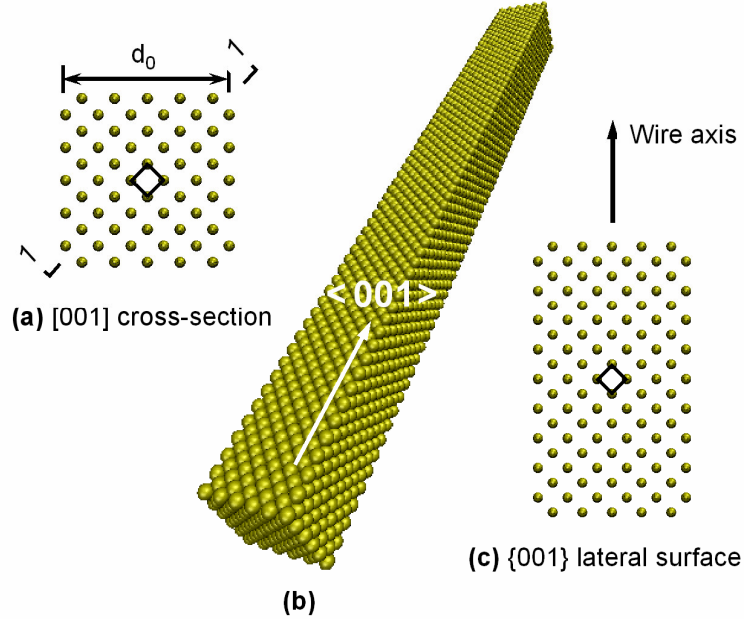
Figure 4.1 The structure of an 1.81×1.81 nm (5×5 lattice constants) Cu nanowire before relaxation: (a) {001} square lattice on square cross-sections; (b) external view of the nanowire; (c) {001} square lattice on lateral surfaces

4.1 Simulation of Top-down Fabrication Process

The wires are created by simulating a top-down fabrication process for nanowires in the spirit what is described in Kondo and Takayanagi (1997). Specifically, the wires are created by "slicing" square columns of atoms from single-crystal bulk Cu along the [001], [010], and [100] directions and by subsequent computational relaxation following the slicing. The nanocolumns initially isolated from bulk have the perfect FCC crystal structure of single-crystalline bulk Cu at 300 K with a lattice constant of 0.3615 nm. The initial length of the columns is 21.69 nm (or 60 lattice constants). The lateral dimensions of the columns vary from 1.45×1.45 nm (or 4×4 lattice constants) to 2.89×2.89 nm (or 8×8 lattice constants). The axes of the nanocolumns are in the [001] direction and both

28

their cross-sections and lateral surfaces are {001} planes with the same square lattice, as illustrated in Figure 4.1.

Because higher-energy free surfaces are created during the top-down fabrication process, the wires are not at equilibrium when they are initially sliced out of the bulk lattice. In order to obtain more stable structures, the nanowires are allowed to relax, with one end fixed in the axial direction and the other end free of constraints. Temperature is kept constant at 300 K during relaxation by rescaling atomic velocities. The structural transformation during relaxation and the structure after an equilibrium state is reached are analyzed.

| Time: | 0 ps | 30 ps | 40 ps | 50 ps | 60 ps |
| ε_1 : | 0.0% | 9.2% | 14.4% | 24.1% | 28.2% |
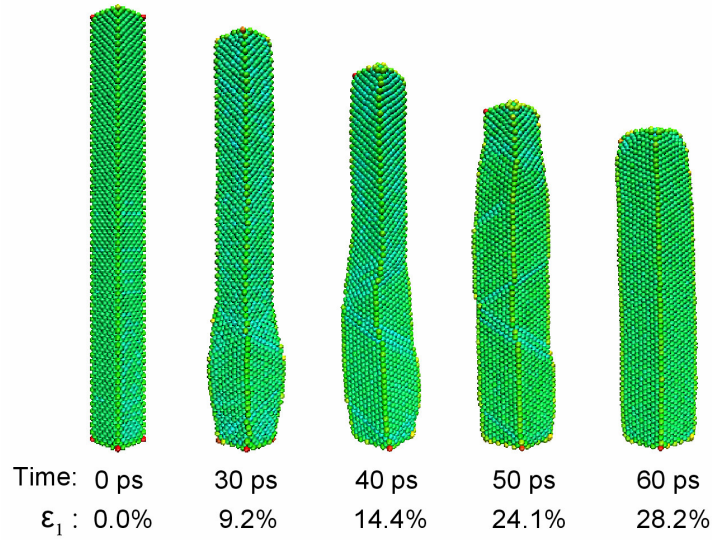
Figure 4.2 The progression of the structural transformation in a 1.81×1.81 nm (5×5 lattice constants) Cu nanowire at 300 K

4.2 Lattice Reorientation during Relaxation

The {001} surfaces of some FCC transition and noble metals are known to reconstruct into {111} planes with a close-packed hexagonal lattice to reduce their energy (Hove et al. 1981; Binnig et al. 1984). At the nanoscale, such a surface change can extend into the substrate. In this research, a similar structural transformation is observed in Cu nanowires during relaxation. The process involves the complete wire, from the

surfaces to the interior. It is a structural reconstruction process that transforms the wires from an <100>-axis/{001}-surfaces configuration to an <110>-axis configuration with {111} side surfaces and {110} cross-sectional planes. Both configurations have the same FCC structure albeit different lattice orientations and different shapes. Moreover, a strong size-dependence of the transformation is also observed. Specifically, wires smaller than 2.17×2.17 nm (6×6 lattice constants) undergo a spontaneous lattice reconstruction to lower their energy. Figure 4.2 shows the progression of the transformation of a 1.81×1.81 nm (5×5 lattice constants) wire. The process initiates from one end and propagates to the other end, resulting in a reduction in the wire length and increase in its lateral dimensions. The complete transformation yields an axial strain of approximately −29%

and an increase in cross-sectional area of approximately 13.3%. Wires with cross-sections larger than 2.17×2.17 nm (6×6 lattice constants) do not undergo such a spontaneous lattice reconstruction at 300 K without external stimuli. The morphologies of these larger wires remain very similar to their state as part of a bulk crystal. The most noticeable change is in the length which shows a

Figure 4.3 Axial strain ε_1 after relaxation at 300K as a function of wire size

contraction of less than 1% due to elastic lattice straining. Figure 4.3 summarizes the length changes of wires of different sizes, clearly identifying the critical size for transformation as 2.17×2.17 nm (6×6 lattice constants). A more detailed analysis of the conditions for the initiation of the spontaneous transformation will be given shortly. For now, the discussion focuses on the mechanisms of the transformation at 300 K without external stimuli.

The structural characteristics of the wires before and after the transformation are analyzed by comparing their RDF with that of bulk crystals. Figure 4.4 shows the three RDFs of Cu nanowires and bulk crystals at 300 K. The peaks in the curves indicate that the first, second, and third nearest neighbor distances are $r_A = 2.547$ Å, $r_B = 3.615$ Å, and $r_C = 4.426$ Å, respectively. The peaks in all three curves have essentially the same positions, indicating that the relaxed nanowires have the same FCC crystalline structure as that for bulk Cu crystals and the unrelaxed wires. The curves also show that the lattice constant of the transformed nanowires is approximately the same as that of bulk Cu crystals (3.615 Å). The peaks for the nanowires are lower than those for bulk Cu crystals because the wires have a large proportion of surface atoms which have fewer neighbors. The structure of the reconstructed nanowires has also been analyzed using the centrosymmetry parameter. The results are consistent with the conclusions from Figure 4.4, showing that the transformed wires have a defect-free, single-crystalline FCC structure.
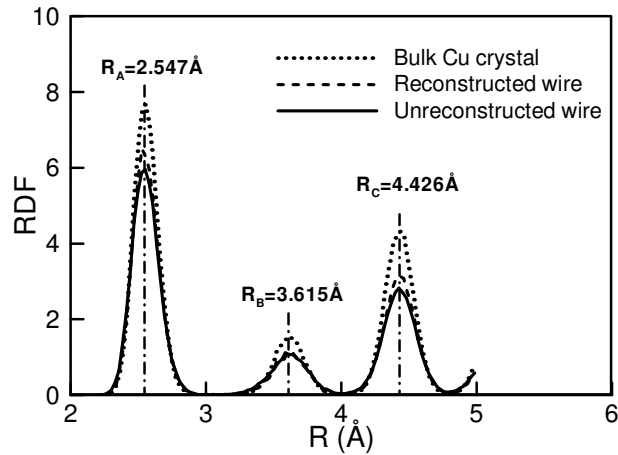
Figure 4.4 The RDFs for Cu nanowires before and after reconstruction and bulk Cu crystal at 300 K

Although maintaining the FCC crystalline structure, the reconstructed wires have clearly different morphologies with their axes and surfaces coincide with different

crystalline directions and planes from those of the un-reconstructed wires. Specifically, the initially <001>-oriented nanowires (with <001> axes and all around {100} surfaces with square lattices) reorient to assume <110> axes, {111} lateral surfaces, and {110} cross-sections, as illustrated in Figure 4.5. While the new side surfaces have perfect hexagonal lattices typical of {111} crystalline planes, the reconstructed cross-sections are characterized by elongated hexagonal lattices indicative of {110} planes as illustrated in Figure 4.6 (Rodrigues and Ugarte 2003). Also, as shown in Figure 4.1(a) and Figure 4.5(a), the shape of the cross-sections changes from square to rhombic. This shape change is associated with the reorganization of the side surfaces into {111} atomic planes, resulting in a reduction in the surface energy. A quantification of the morphological changes is listed in Table 4.1. Note that the data for the transformed configurations of wires with different sizes are for different temperatures. Discussions on the temperature required for the transformation as a function of wire size will be given in the next chapter. For the wire sizes analyzed here, the measured angles of the rhombic cross-sections (α and β in Figure 4.5(a)) are consistent with the angles between the $(\bar{1}11)$ and $(\bar{1}1\bar{1})$ crystalline planes viewed from the [110] axis, as illustrated in Figure 4.6. Specifically, the angles are approximately 109.5° and 70.5°, respectively. Also, the side length of the cross-sections increases 21.0% from 1.81 to 2.19 nm for a 1.81×1.81 nm (5×5 lattice constants) wire. The lateral surface area decreases 12.3% from 156.82 to 137.06 nm^2, resulting in an increase in the atomic density of 14.5% (from 15.2 atoms/nm^2 to 17.4 atoms/nm^2) on the surfaces. Overall, the number of surface atoms remains the same (2380) after the transformation, indicating that there is no atomic diffusion between the surfaces and the interior. This observation is consistent with the characteristics of a diffusionless martensitic transformation (Bhadeshia 2001; Otsuka and Kakeshita February 2002) and is in contrast to surface reconstructions in bulk materials which involve atomic migration from substrate to surfaces (Trimble et al. 2003).
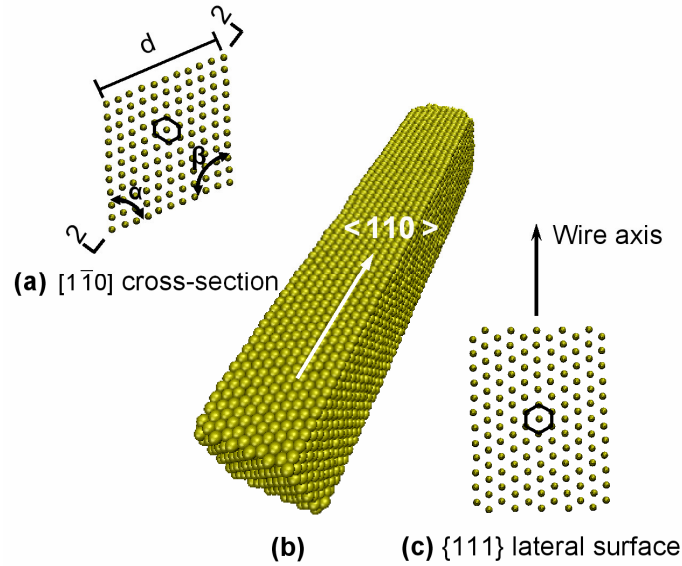
Figure 4.5 The reconstructed structure of a Cu nanowire with initial dimensions of 1.81×1.81 nm (5×5 lattice constants): (a) <110> elongated hexagonal lattice on a rhombic cross-section, (b) external view of the reconstructed nanowire, (c) {111} hexagonal lattice on lateral surfaces
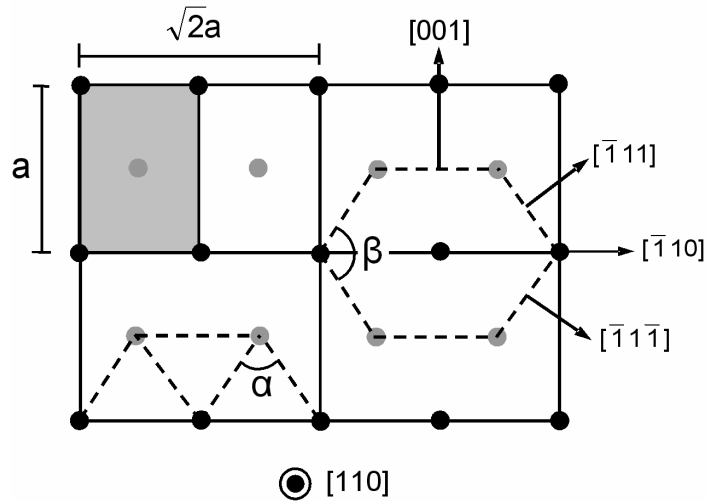
Figure 4.6 A schematic illustration of the projections of two (110) planes (black and gray atoms) in an FCC structure observed along the [110] directions; the (110) plane is characterized by elongated hexagonal lattice with $\alpha = 70.5°$ and $\beta = 109.5°$ (Rodrigues and Ugarte 2003).

Table 4.1 Morphological change of nanowires associated with reconstruction

d_0 (lattice const)	d_0 (nm)	d (nm)	α	β	Wire length l (nm)	Lateral surface area A_0 (nm^2)	Lateral surface area A (nm^2)	Temperature (K)
4	1.45	1.76	70.5°	109.5°	15.33	125.45	110.46	100
5	1.81	2.19	70.0°	110.0°	15.61	156.82	137.06	300
6	2.17	2.65	69.7°	110.3°	15.87	188.18	168.42	450
7	2.53	3.07	70.7°	109.3°	16.04	219.55	196.67	600
8	2.89	3.39	68.3°	111.3°	16.41	250.91	222.28	900
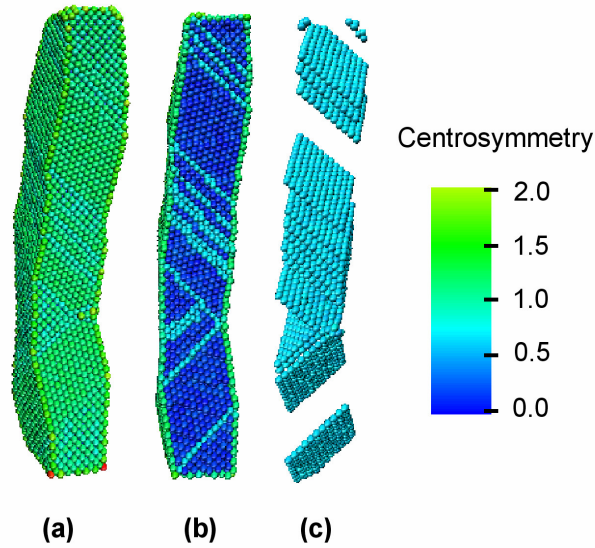
Figure 4.7 The configuration of a Cu nanowire with initial lateral dimensions of 2.17×2.17 nm (6×6 lattice constants): (a) external view; (b) section view; (c) Defects (twin boundaries) only. Atoms are colored according to their centrosymmetry values.

The partially reconstructed configuration in Figure 4.7 provides an illustration of the twinning process responsible for the transformation. Although at the bulk level twinning is usually observed in BCC and HCP materials which have fewer slip systems, it has been observed in nanostructured FCC materials such as Cu (Molares et al. 2001; Wang et al. 2004b), Ag (Sauer et al. 2002), and Au (Wang et al. 2004b)). For example, Wang et al. (2004) observed micro-twinning in electrochemically deposited Cu

nanowires with diameters of 30-50 nm (Wang et al. 2004b). Molares et al. (2001) found twin structures in Cu nanowires with a diameter of 70 nm. In the simulations here, twin boundaries initially nucleate at the fixed end and propagate toward the free end via the gliding of {111}<112> partial dislocations under the compressive stress induced by surface-stress. This twinning process causes a 90° lattice rotation and transforms the wire from the <001>/{001} configuration to the <110>/{111} configuration as the twin boundaries sweep through the wire length.
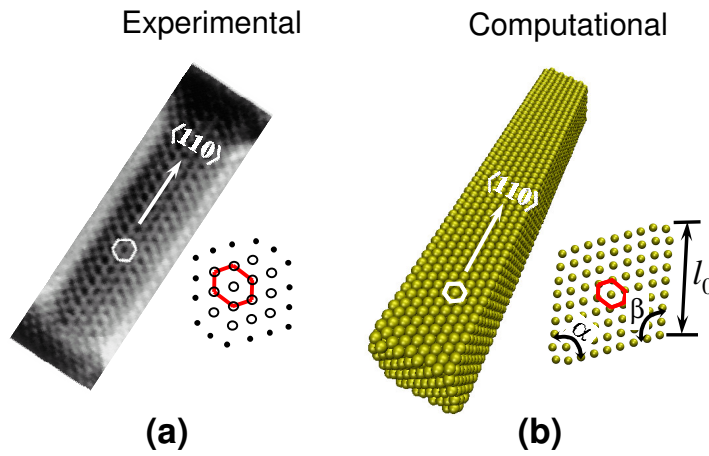
Figure 4.8 Comparison of wire structures obtained from MD simulations and experiments, (a) a <110>/{111} Au wire cut from a <001>/{001} Au nanofilm by electron beam irradiation (reproduced from Ref. [10]), (b) a <110>/{111} Au wire with rhombic cross-sections ($\alpha = 70.5°$ and $\beta = 109.5°$) as predicted by atomistic calculations as the result of the same top-down fabrication process in (a)

The structures of the fully reconstructed wires reported above are in good agreement with those of the laboratory fabricated wires including Cu, Au, and Pt nanowires, e.g., the Cu wires fabricated by vacuum vapor deposition (Liu and Bando 2003) and by a complex surfactant-assisted hydrothermal reduction process (Liu et al. 2003), and Au wires fabricated by cutting Au nanofilms using electron beam eradiation (Kondo and Takayanagi 1997). Just like what is seen above in the simulations, the

laboratory nanowires also have defect-free single-crystalline FCC structures with <110> axes and {111} surfaces, indicating that <110> is the preferred growth orientation and {111} planes are preferred lateral surfaces, as shown in Figure 4.8.
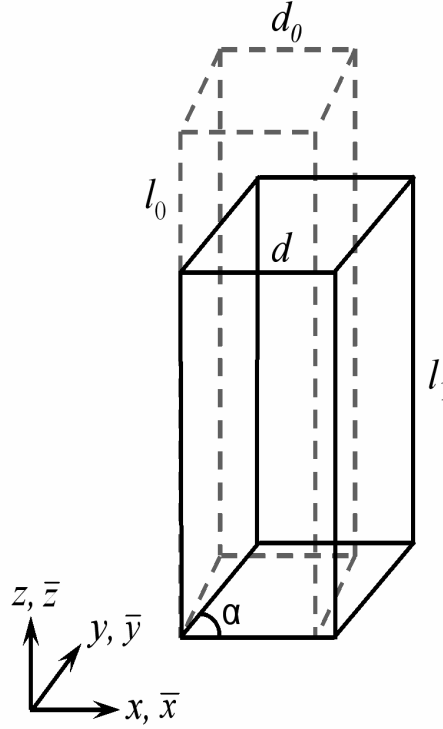
Figure 4.9 A schematic illustration of the deformation of a wire associated with the lattice transformation; the gray dash lines indicate the wire configuration before the transformation, the solid lines denote the configuration after the transformation.

4.3 Quantification of Large Deformation

To quantify the deformation associated with the transformation, the deformation function is evaluated. This analysis is a phenomenological quantification by considering the wire as a continuum and by focusing on the overall deformation outcome. As illustrated in Figure 4.9, the relations between the coordinates before the transformation (x, y, and z) and the coordinates after the transformation ($\bar{x}$, $\bar{y}$, and $\bar{z}$) can be written as

$$\begin{cases} \bar{x} = \dfrac{d}{d_0}(x + y\cos\alpha), \\[2mm] \bar{y} = \dfrac{d}{d_0}\, y\sin\alpha,\ \text{and} \\[2mm] \bar{z} = \dfrac{l_1}{l_0}\, z; \end{cases} \tag{4.1}$$

where d_0 and d are the side lengths of the cross-sections before and after the transformation respectively and l_0 and l_1 are the wire lengths before and after the transformation, respectively. The deformation gradient corresponding to Eq. (4.1) is

$$\mathbf{F} = \begin{bmatrix} \dfrac{d}{d_0} & \dfrac{d}{d_0}\cos\alpha & 0 \\[3mm] 0 & \dfrac{d}{d_0}\sin\alpha & 0 \\[3mm] 0 & 0 & \dfrac{l_1}{l_0} \end{bmatrix} \tag{4.2}$$

For the 1.45×1.45 nm (4×4 lattice constants) wire in Table 1,

$$\mathbf{F} = \begin{bmatrix} 1.220 & 0.407 & 0 \\ 0 & 1.150 & 0 \\ 0 & 0 & 0.707 \end{bmatrix} \tag{4.3}$$

yielding a volume ratio of

$$\frac{\Omega}{\Omega_0} = \det(\mathbf{F}) = 0.992 \tag{4.4}$$

for the transformation. In the above expression, Ω_0 and Ω are, respectively, the volumes before and after the transformation and $\det(\mathbf{F})$ denotes the determinant of $\mathbf{F}$. The volume change associated with the transformation is small because the wire maintains the same

FCC structure after the transformation. The Lagrangian strain tensor for the deformation from the initial configuration to the transformed configuration is

$$\mathbf{E} = \frac{1}{2}\left(\mathbf{F}^T \cdot \mathbf{F} - \mathbf{I}\right) = \begin{bmatrix} 0.244 & 0.250 & 0 \\ 0.250 & 0.244 & 0 \\ 0 & 0 & -0.250 \end{bmatrix} \qquad (4.5)$$

where $\mathbf{I}$ is the identity tensor. The corresponding Eulerian strain tensor or the negative of the Lagrangian strain for the inverse deformation from the transformed configuration to the initial (or stretched) configuration is

$$\mathbf{E}^* = \frac{1}{2}\left(\mathbf{I} - \mathbf{F}^{-T} \cdot \mathbf{F}^{-1}\right) = \begin{bmatrix} 0.164 & 0.119 & 0 \\ 0.119 & 0.080 & 0 \\ 0 & 0 & -0.500 \end{bmatrix} \qquad (4.6)$$

where, $\mathbf{F}^{-1}$ denotes the inverse and $\mathbf{F}^{-T}$ denotes the inverse transpose of $\mathbf{F}$. $\mathbf{E}$ and $\mathbf{E}^*$ allow the forward and reverse deformations to be fully quantified. In particular, the axial strains associated with the relaxation is $E_{zz} = -0.250$. This corresponds to an engineering strain of $\varepsilon_1 = (l_1 - l_0)/l_0 = F_{zz} - 1 = \sqrt{2E_{zz} + 1} - 1 = -0.293$ (relative to the original unrelaxed length l_0). For the reverse (tensile) deformation from the relaxed state which will be discussed in the next chapter, the axial strain is $-E^*_{zz} = 0.500$ when the wire recovers its original length prior to relaxation, corresponding to an engineering strain of $\varepsilon_2 = (l_0 - l_1)/l_1 = 1/F_{zz} - 1 = \sqrt{-2E^*_{zz} + 1} - 1 = 0.414$. It will be illustrated in the next chapter by a crystallographic analysis that this large strain is due to a 90º lattice rotation.

4.4 Chapter Summary and Insights

The structure and mechanical behavior of Cu nanowires fabricated via a top-down approach are analyzed. The calculations use MD simulations to model the relaxation process during the fabrication. At a temperature of 300 K, spontaneous lattice reorientation is observed in wires smaller than 2.17×2.17 nm (6×6 lattice constants) but not in wires with larger sizes. The wires change from the <001>/{001} configuration to

the <110>/{111} configuration through a lattice reorientation, with the cross-sectional shape changing from square to rhombic and the wire length decreasing approximately 29.3%. The calculated structure of the reconstructed wires is in good agreement with what has been observed experimentally in laboratory FCC metal nanowires.

As will be further discussed in the next chapter, the lattice reconstruction during relaxation process is similar to the spontaneous lattice reorientation process during unloading. The reconstruction occurs because the <110>/{111} configuration is always energetically favored over the <001>/{001} configuration regardless of the size of the nanowire. This transformation progresses through the propagation of twin boundaries driven by surface stress-induced stress. Furthermore, the transformation process is both size and temperature dependent because of the existence of an energy barrier for the initiation of the transformation.

CHAPTER 5 SHAPE MEMORY IN METAL NANOWIRES

This chapter reports the discovery of a novel SME in <110>/{111} metal nanowires (including Cu, Ni and Au) obtained from the lattice reconstruction during relaxation discussed in the previous chapter. Under tensile loading and unloading, these metal wires can recover elongations of up to 50%, well beyond the recoverable strains of 5-8% typical for most bulk SMAs. This behavior arises from a reversible lattice reorientation within the face-centered cubic (FCC) crystalline structure and is driven by the surface stress and high surface-to-volume ratios of the one-dimensional nano-materials, a unique and hitherto unknown mechanism which is different from that for SMAs (Liang and Zhou 2005; Liang et al. 2005; Liang and Zhou 2006). This SME exists over a wide range of temperature and is associated with response times on the order of nanoseconds, making the nanowires attractive functional components for a new generation of biosensors, transducers, and interconnects in NEMS (Büttgenbach et al. 2001; Patolsky and Lieber 2005).

This research focuses on the transformation mechanism, driving force, and critical temperature for the SME, with a particular emphasis on the role of generalized stacking fault energies in determining the existence of the pseudoelastic behavior. Specifically, an explanation as to why this behavior is observed in some FCC metals (e.g., Cu, Au, Ni) but not in others (such as Al) is given. It is observed that FCC metals showing this effect share the common attribute of having high twinnability, a parameter identified by Tadmor and Hai (2003) for quantifying the tendency to form twins in FCC metals. For the metals that exhibit this behavior, the levels of recoverable strain and the critical temperature associated with the SME are quantified. Finally, the effect of wire size is

discussed and the reason why this phenomenon exists only in nanowires but not in bulk single crystals of the same FCC metals is pointed out.

5.1 Mechanical Behavior

Starting from the <110>/{111} equilibrium configuration, quasistatic tensile loading and unloading are applied on the wires to study their mechanical behaviors. Depending on the material, three types of behaviors are observed. Specifically,

(1)   above a critical temperature T_{cr} (discussed later), Cu and Ni wires exhibit a pseudoelastic behavior with reversible strains up to 51%, well beyond the 5-8% reversible strains typical for most bulk SMAs. Below T_{cr}, the deformation is not spontaneously recoverable and the wires retain their deformed configurations after unloading. For Cu wires, subsequent heating to a temperature above T_{cr} activates the SME and allows the wires to return to their original configurations. For Ni wires, the wires return to their original configurations only when an external compressive stress is applied;

(2)   in contrast, the tensile deformation of Al nanowires is irreversible upon unloading, regardless of temperature;

(3)   Au wires exhibit transitional behaviors from pseudoelasticity like that of Cu and Ni wires at low temperatures to irreversible deformation like that of Al wires at high temperatures.

The different behaviors reported here are associated with, respectively, twinning and slip which are two different but related deformation mechanisms in FCC metals.

(a)

(b)
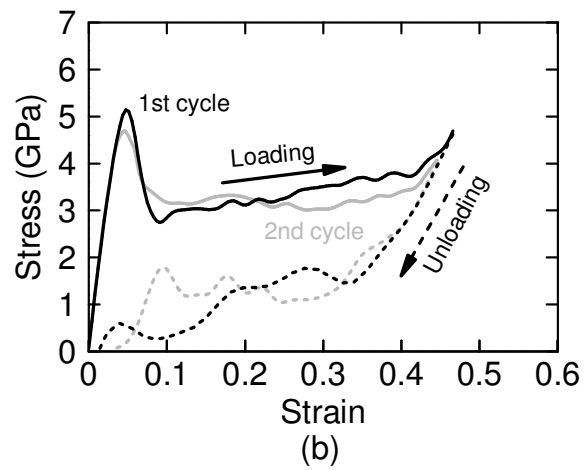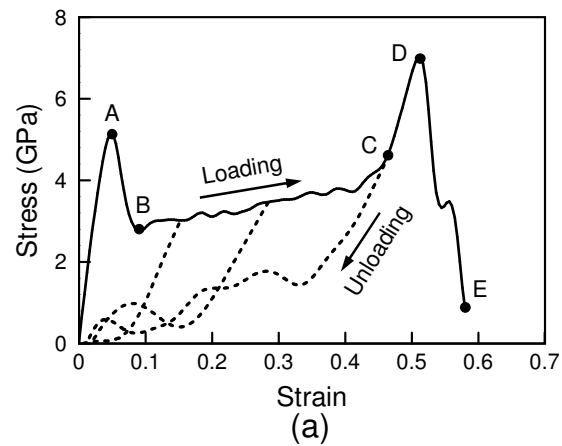
Figure 5.1 The stress-strain curves of a 1.8×1.8 nm Cu wire at 200 K during loading and unloading, (b) the same wire under cyclic loading and unloading
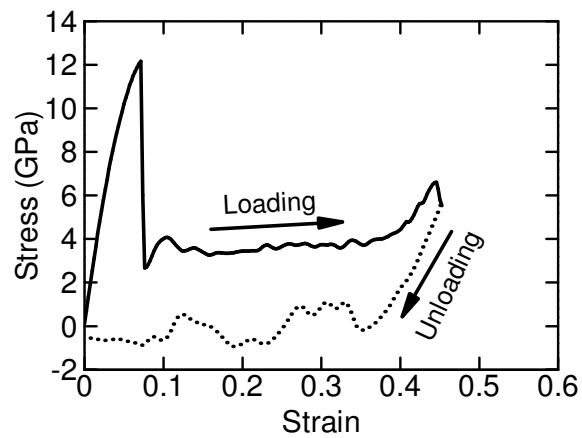
Figure 5.2 The stress-strain curve of 2.1×2.1 nm Ni nanowire during loading and unloading at 300 K

5.1.1 Pseudoelasticity of Cu and Ni Wires

The stress-strain curves in Figure 5.1 and Figure 5.2 show the pseudoelastic behavior upon loading, unloading and cyclic loading/unloading of Cu and Ni wires. Clearly, the responses are drastically different from those of the corresponding bulk metals. Specifically, the nanowires seem highly ductile with fracture strains of approximately 58%. In comparison, the fracture strains of most bulk FCC metals are usually less than 15%. In Figure 5.1(a), the loading path of the stress-strain curves consists of two elastic deformation stages (O→A and C→D) followed by two yield points (A and D, respectively), a stage of slow strain hardening over a wide range of strain (B→C), and a stage of precipitous stress drop (D→E). This behavior arises from a unique underlining deformation process. Between O and A, the <110>/{111} wire undergoes elastic stretching. Point A corresponds to the beginning of a lattice reorientation process which leads to a new configuration with a <001> axis and {001} side surfaces, as shown in Figure 5.3. Between C and D, the newly formed <001>/{001} wire undergoes elastic stretching. Further loading beyond D causes the wire to yield through the formation and propagation of full dislocations which ultimately lead to necking and fracture of the nanowire at E (Liang and Zhou 2004).

The unique lattice reorientation process (A→C in Figure 5.1 (a)) is the key to the shape memory behavior of the wires. The lattice reorientation progresses with the propagation of a single twin boundary. The twin boundary nucleates at one end and propagates to the other end until the whole nanowire recovers its <001> orientation. Figure 5.3 shows a sectional view of the 1.81×1.81 nm Cu wire while the twin boundary is in the middle of the transforming wire. The twin boundary separates the transformed

43

(<001>/{001}) region from the untransformed (<110>/{111}) region. Clearly, the transformed region has square lattices on both cross-sectional and lateral surfaces. The untransformed region retains the <110> elongated hexagonal lattice on cross-sections and {111} hexagonal lattice on lateral surfaces. The cross-section at the interface clearly shows the transition from the <110> orientation to the <001> orientation, as shown in Figure 5.3. The reorientation is completed through the propagation of a {111} twin boundary, which involves repetitive nucleation, gliding, and annihilation of $\frac{1}{6}$<112> Shockley partial dislocations, as shown in Figure 5.4. Specifically, the partial dislocation is nucleated from one edge, glides across
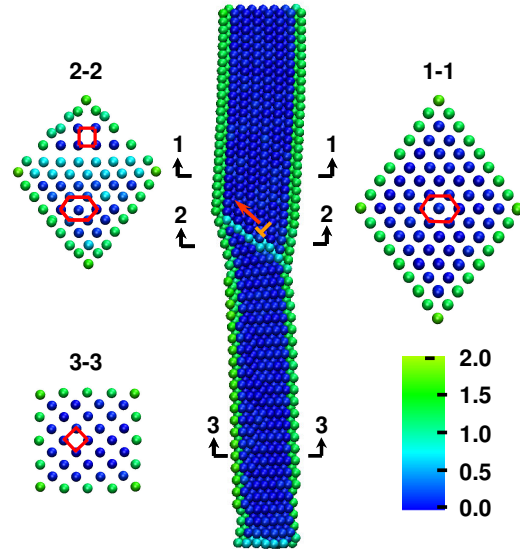
Figure 5.3 Lattice orientations on the cross-sections of a 1.8×1.8 nm Cu nanowire at a strain of 0.24, the middle image shows a sectional view along the wire axis and the $[\bar{1}\bar{1}0]$ diagonal of the cross-section, cross-section 1-1 shows the elongated hexagonal lattice in the unrotated domain with the <110>/{111} configuration, cross-section 2-2 is in the transition region containing both the <001>/{001} and the <110>/{111} configurations, and cross-section 3-3 shows the square lattice in the reoriented domain with the <001>/{001} configuration,

the wire on the {111} plane adjacent to the twin plane, and finally annihilates at the other edge. This process repeats itself and at each cycle the twin boundary propagates by an

inter-planar distance between two neighboring {111} planes. As the twin boundary sweeps through its length, the wire is progressively transformed into the new <001> orientation. Upon the arrival of the twin boundary at the top end of the wire (corresponding to point C in Figure 5.1(a)), the whole wire is in the <001>/{100} state. This lattice reorientation process has been directly observed in experiments during the stretching of Au nanowires (Rego et al. 2003).
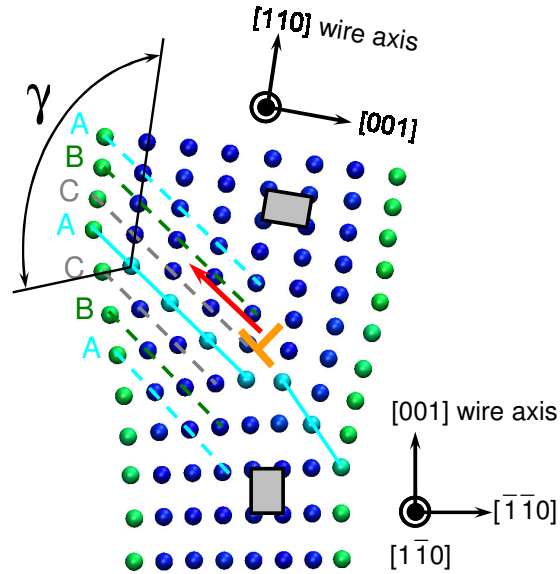
Figure 5.4 The details of the {111} twin boundary and the $\frac{1}{6}$<112> Shockley partial dislocation in Figure 5.3, the misorientation angle γ = 109.5°. Atoms are colored according to their centrosymmetry values.

The mobile twin boundary is formed by mismatch defects between the <110>/{111} lattice and the <001>/{001} lattice, as illustrated in Figure 5.4. The stacking sequence within each region is ABCABC in the direction perpendicular to the boundary. At the interface, the stacking sequence is ABC|A|CBA where the middle A is the mirror plane. Crystallographically, this is a coherent {111} twin plane with its misorientation axis

aligned in the $[\bar{1}1\bar{2}]$ direction. The misorientation angle γ between the lattices is measured to be 109.5°. The boundary is essentially a $\Sigma 3$ coherent grain boundary separating two nanoscale grains with <001> and <110> orientations, respectively (Rittner and Seidman 1996). The lattice reorientation essentially progresses through the migration of such $\Sigma 3$ boundaries. This deformation mechanism has been confirmed experimentally in nanocrystalline Cu (Field et al. 2004) with grain sizes between 10 to 20 nm.
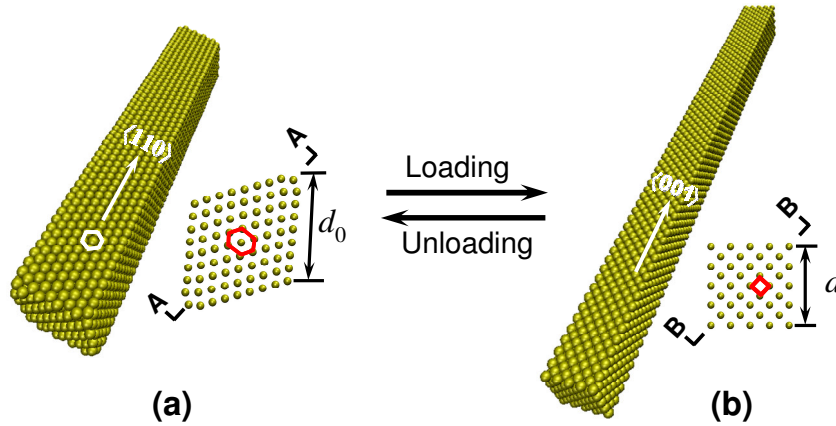
Figure 5.5 Reversible lattice reorientations upon loading and unloading in metal nanowires; (a) a <110>/{111} Cu wire with rhombic cross-sections, (b) stretched <001>/{001} wire with square cross-sections

Upon unloading at temperatures above T_{cr}, the <001>/{001} wire spontaneously transforms back to the original <110>/{111} configuration via a lattice reorientation process in reverse to what is described above for loading. The reversibility of the lattice reorientation from <110>/{111} to <001>/{001} allows the associated deformation to be fully recovered, giving rise to a pseudoelastic behavior of the wire, as shown in Figure 5.5. This reorientation process is driven by the high surface-stress-induced internal stresses in the nanowires and has been observed in experiments and computations for Au nanowires and nanofilms (Kondo and Takayanagi 1997; Kondo et al. 1999; Hasmy and

Medina 2002; Diao et al. 2003; Diao et al. 2004; Liang and Zhou 2005). Specifically, spontaneous lattice reorientation from <001> to <110> is observed in Au wires when they are cut from Au nanofilms and their free standing configuration is the <110>/{111} structure in Figure 4.8 (Kondo and Takayanagi 1997; Ohnishi et al. 1998). Furthermore, the same result is also obtained in computations when different atomistic potentials (including an EAM, a modified embedded atom method (MEAM), and a surface embedded atom potential (SEAM) are used (Diao et al. 2004). The spontaneous reverse lattice reorientation allows the tensile deformation to be fully recovered without residual defects. The dash lines in Figure 5.1 and Figure 5.2 represent the unloading paths from different strains. The loading and unloading paths together form hysteretic loops typical of shape memory materials. Since the wires recover their original configurations after unloading, the same behavior is observed in subsequent cycles of loading and unloading, as shown in Figure 5.1(b). The minor differences between cycles can be attributed to random thermal oscillations and possible residual defects (discussed later).

If the two wire configurations are considered as the "0" and "1" states in logic circuits, the pseudoelastic behavior of nanowires can be potentially utilized for applications in information technologies. In such applications, the heat dissipation is an important factor to consider because the state-switching rates are usually very high (up to 10^9 s^{-1}). As shown in Figure 5.1(a), the pseudoelastic behavior of nanowires has a large hysteresis loop, indicating a considerable amount of heat is generated in one cycle. Specifically, the heat dissipation is 0.93 J/m^3 when the wire in Figure 5.1(a) is unloaded from $\varepsilon = 0.47$. Such heat dissipation can cause fast temperature increase if the heat is not transferred out of the wire promptly, eventually killing the pseudoelastic behavior. In

order to increase the switching rates without excessive heat generation, it is more efficient to unload the wires from strains (such as 10%) smaller than the maximum reversible strains (usually 50%). As long as the lattice reorientation has started, these small deformations cause detectable state changes because the formation of the twin boundary. At the same time, the heat dissipation is much lower due to smaller hysteresis loops. Furthermore, the small sizes of nanowires facilitate heat transfer through conduction and convection because of the large surface-to-volume ratios. Overall, the rates of heat generation and transfer together determine the rate of temperature increase, which is affected by the state-switching rates, wire sizes, and strains. Further study is necessitated to characterize the influence of these factors on the temperature increase during cyclic loading and unloading processes.

(a) (b)
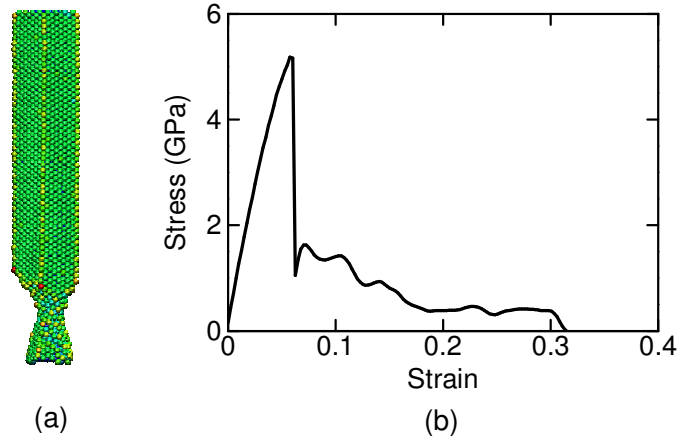
Figure 5.6 The tensile deformation behavior of an Al wire at 300 K: (a) the deformed configuration at $\varepsilon = 0.13$, (b) the stress-strain curve. Atoms are colored according to their centrosymmetry values.

5.1.2 Irreversible Deformation of Al Wires

Al wires do not show the pseudoelastic behavior seen for Cu and Ni wires. This difference arises from a different deformation mechanism. Specifically, Al wires first deform elastically during loading. Upon yielding, a necking process starts and quickly leads to thinning and eventual rupture of the wire, as shown in Figure 5.6. While twinning is responsible for the lattice reorientation in Cu and Ni wires, slip via full dislocations of the $\frac{1}{2}\langle 110 \rangle$ type is primarily responsible for the necking process in Al wires. The slip mechanism involving full dislocations causes the tensile deformation to be permanent and irreversible upon unloading. Consequently, no shape memory behavior is possible for such wires.

5.1.3 Temperature-dependent Transition Behavior of Au Wires

Au wires show a temperature-dependent transitional behavior between the pseudoelasticity and the plasticity described above. Specifically, at low temperatures, Au wires show similar forward and reverse lattice reorientations through the propagation of twin boundaries as in Cu and Ni wires. However, the reorientation process during loading may not sweep through the entire wire length and necking can occur at the twin boundary before the reorientation process is complete, as shown in Figure 5.7(a). The stress plateaus between points A and B for T = 5 K and between points C and D for T = 50 K in Figure 5.7(b) correspond to the lattice orientation from the <110>/{111} configuration to the <100>/{100} configuration. The necking process starts at point B (T = 5 K) and D (T = 50 K) and leads to the precipitous drop of stresses following these points. If unloading occurs before necking, the Au wires can recover their original <110>/{111} configuration through a reverse lattice reorientation process which is the same as what is

seen in Cu and Ni wires. Once necking occurs, however, the deformation is no longer

$\varepsilon = 35.3\%$

$\varepsilon = 20.6\%$

$\varepsilon = 15.7\%$

$\langle 110 \rangle / \{111\}$

$\langle 100 \rangle / \{100\}$

(a) T=5 K

(b) T=50 K

(c) T=200 K

(a)

(b)
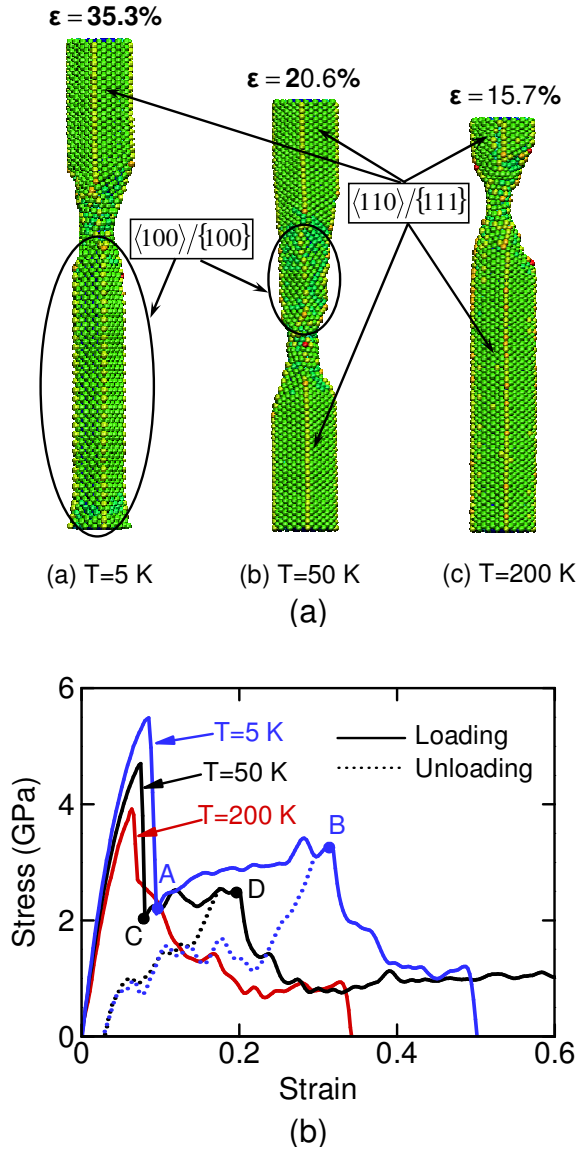
Figure 5.7 The tensile loading and unloading behavior of Au wires at different temperatures: (a) deformed configurations, (b) stress-strain curves. Atoms are colored according to their centrosymmetry values.

fully reversible. Consequently, the maximum reversible strains of Au wires are less than those of Cu and Ni wires because of the incomplete reorientation process during loading.

The fraction of reoriented lattice (<100>/{100}) at the onset of necking decreases as temperature increases, as shown in Figure 5.7(a). At T = 200 K, no reorientation is observed and necking starts immediately after yielding. This scenario corresponds to the case of Al wires discussed above, with the deformation progressing via slip and being irreversible.

5.2 Deformation Mechanism: Twinning or Slip

The different behaviors of Cu, Ni, Au, and Al wires result from different deformation mechanisms. The pseudoelasticity of Cu and Ni is due to the reversible lattice reorientation associated with twin boundary propagation. The irreversible plasticity of Al wires is primarily due to the slip of full dislocations. The mixed occurrence of twinning and slip explains the transitional behavior of Au wires between pseudoelasticity and plasticity. In summary, for the nanowires analyzed twinning leads to pseudoelasticity and slip leads to permanent deformation.

Being two competitive mechanisms in FCC metals, twinning and slip are known to occur under different conditions. Conventional wisdom suggests that metals with low γ_{sf} are more likely to deform through twinning. However, γ_{sf} alone may not be enough to determine whether a metal would deform via twinning or slip. For example, Ni wires deform via twinning while Al wires deform via slip, even though Ni and Al have similar levels of γ_{sf}. Swygenhoven et al. (2004) have shown that the competition between twinning and slip is primarily determined by the energy ratio of γ_{sf}/γ_{us}. Specifically, metals with lower γ_{sf}/γ_{us} values are more likely to deform via twinning than slip. This understanding is consistent with the observation that twinning is more likely to occur in Ni wires than in Al wires since $(\gamma_{sf}/\gamma_{us})_{Ni} = 0.317$ and $(\gamma_{sf}/\gamma_{us})_{Al} = 0.836$, see Table 3.2.

51

Even though γ_{sf}/γ_{us} provides a better criterion than γ_{sf} for assessing the competition between twinning and slip, it can not explain all cases and a higher order effect ap pears to exit. For example, as previously shown, twinning is more likely in Ni wires than in Au wires despite the fact that Ni has a slightly higher ratio of γ_{sf}/γ_{us} (0.317) than Au (0.307). The reason is that the competition is determined by the energy barriers associated with both slip and twinning. While γ_{sf}/γ_{us} only quantifies the energy barrier for slip, the energy barrier for twinning must also be considered.
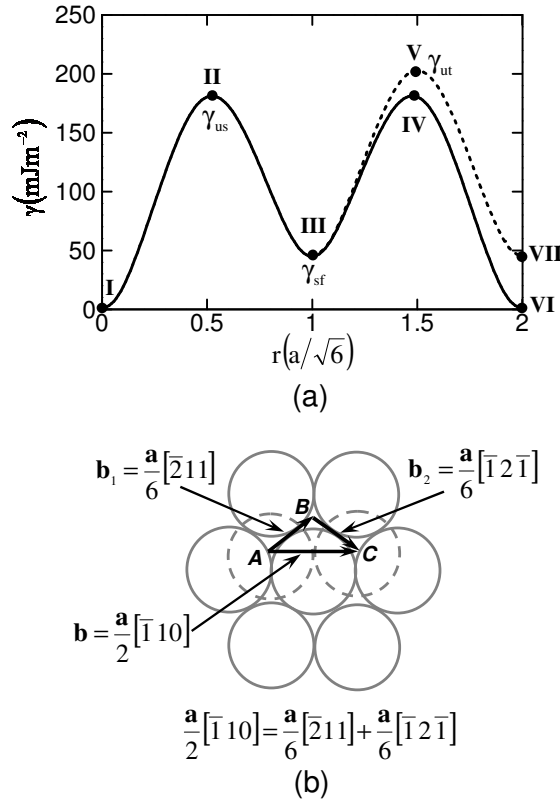
Figure 5.8 A schematic illustration of the relationship between a dissociated full location and two partial dislocations, (a) generalized stacking fault energy curve showing the energy variation during dislocation nucleation, (b) the relationship between Burger's vectors

The competition between twinning and slip can be better explained by the dislocation nucleation criterion of Rice (1992) and the twin nucleation criterion of Tadmor and Hai (2003). In Rice's theory, a full $\frac{1}{2}\langle 110 \rangle$ type dislocation can be considered as being formed by two $\frac{1}{6}\langle 112 \rangle$ type Shockley partial dislocations in two successive steps. This sequence of events is illustrated in Figure 5.8. At point I (corresponding to position A of the dashed layer of (111) atoms in Figure 5.8 (b)), the system is in a stress-free state. The GSFE (vertical axis in Figure 5.8(a)) increases as the shear displacement (horizontal axis in Figure 5.8(a)) between the two neighboring (111) planes increases. At point II (position B in Figure 5.8(b)), the system is at an unstable state and a leading partial dislocation with Burger's vector $\frac{a}{6}\left[\overline{2}11\right]$ is formed. In Figure 5.4, the emission of this partial is from the right-hand edge (surface) of the cross-section of the nanowire shown. Obviously, the nucleation of this leading partial must overcome the energy barrier γ_{us}. Following the emission, a degree of stress relaxation and energy release occurs, as indicated by the portion of the GSFE curve between points II and III in Figure 5.8(a). The stacking fault between the two neighboring (111) planes behind the partial dislocation line corresponds to an elevated energy level of γ_{sf} (Point III in Figure 5.8(a) and position B in Figure 5.8(b)) relative to the perfect FCC stacking sequence at point I in Figure 5.8(a) and position A in Figure 5.8(b). As loading continues and sufficient energy is imparted to overcome the second energy barrier at the level of γ_{us} (point IV in Figure 5.8(a)), a trailing partial dislocation with the Burger's vector $\frac{a}{6}\left[\overline{1}2\overline{1}\right]$ is emitted between the same pair of (111) slip planes. The leading and the trailing partials combine to form a

full dislocation with the Burger's vector $\frac{a}{2}\left[\bar{1}10\right]$. This deformation process can be expressed as

$$\frac{\mathbf{a}}{6}\left[\bar{2}11\right]+\frac{\mathbf{a}}{6}\left[\bar{1}2\bar{1}\right]\rightarrow\frac{\mathbf{a}}{2}\left[\bar{1}10\right]. \tag{5.1}$$

Obviously, the energy barrier for the nucleation of the trailing partial is $\gamma_{us}-\gamma_{sf}$. The full dislocation represents a permanent unit shift in the FCC stacking sequence and returns the lattice to the original low energy state of point I (or VI). This mechanism is what is responsible for the irreversible deformation in Al wires and Au wires at high temperatures.

Based on Rice's theory, Tadmor and Hai (2003) have shown that in the twinning mode, a leading partial is first nucleated from a sharp edge of a surface. Instead of the emission of a trailing partial, a second leading partial (twinning partial) is nucleated on a neighboring slip plane next to the original pair of slip planes. The emission of the twinning partial can be analyzed by the dotted curve in Figure 5.8(a). While the solid GSFE curve in Figure 5.8(a) characterizes the interplanar energy associated with a slip discontinuity introduced in a perfect crystal; the dotted curve in Figure 5.8(a) characterizes the energy to form a microtwin by shearing of a plane adjacent to an existing intrinsic stacking fault formed by the passage of a leading partial. The shearing begins at point III at an elevated energy state (γ_{sf}). A twinning partial is emitted at point V where the energy reaches a maximum of γ_{ut} or the unstable twinning energy. The interplanar energy reaches a new minimum at point VII after the slip of a full Burgers vector. This process allows the twin plane to move one layer in the direction perpendicular to the slip planes. For the nanowires, this process of the nucleation of

54

twinning partials on adjacent layers repeats itself and progressively moves the twin plane along the wire axis, layer by layer. It also results in the reorientation of the $\langle 110 \rangle / \{111\}$ wire into the $\langle 100 \rangle / \{100\}$ wire.

Clearly, the deformation mode (twinning or full dislocation motion) is determined by the competition between the nucleation of the trailing partial needed to complete the dissociated full dislocation and the nucleation of the twinning partial needed to form a microtwin. Based on the aforementioned dislocation nucleation process, Tadmor and Hai (2003) developed a criterion for the onset of deformation twinning which quantifies the competition between slip and twinning. The related twinnability is

$$\tau_a = \left[1.136 - 0.151 \frac{\gamma_{sf}}{\gamma_{us}} \right] \sqrt{\frac{\gamma_{us}}{\gamma_{ut}}} \, . \tag{5.2}$$

This parameter depends on both γ_{us}/γ_{ut} and γ_{sf}/γ_{us} which measure the energy barriers associated twinning and slip, respectively. On one hand, twinning is favored when γ_{sf}/γ_{us} is small and γ_{us}/γ_{ut} is large (as in the case of Cu and Ni) because small values of γ_{sf}/γ_{us} indicate higher barriers of $\gamma_{us} - \gamma_{sf}$ for the nucleation of the trailing partial and large γ_{us}/γ_{ut} values indicate lower barriers for the nucleation of a twinning partial. On the other hand, slip is favored when γ_{sf}/γ_{us} is large and γ_{us}/γ_{ut} is small (as in the case of Al). As shown in Table 3.2, the twinnability ranking based on interatomic potentials for the metals analyzed is

$$\tau_a^{Cu} > \tau_a^{Ni} > \tau_a^{Au} > \tau_a^{Al} \, . \tag{5.3}$$

This is in good agreement with the results of experiments and first principle calculations (Tadmor and Bernstein 2004). Furthermore, it clearly explains the different behaviors of the FCC nanowires reported here. Cu and Ni exhibit reversible deformations

through twinning because it is favored over slip. On the other hand, the deformation of Al wires is irreversible because slip is the favored over twinning.

The above analysis does not account for the effect of temperature which is important for Au because it has a twinnability in the transition regime. Our observation of Au wires showing twinning (and therefore, pseudoelasticity and SME) at low temperatures and slip (and therefore, plasticity) at high temperatures is consistent with the experimental observation that twinning tends to occur at lower temperatures (Meyers 1984; Hertzberg 1989).
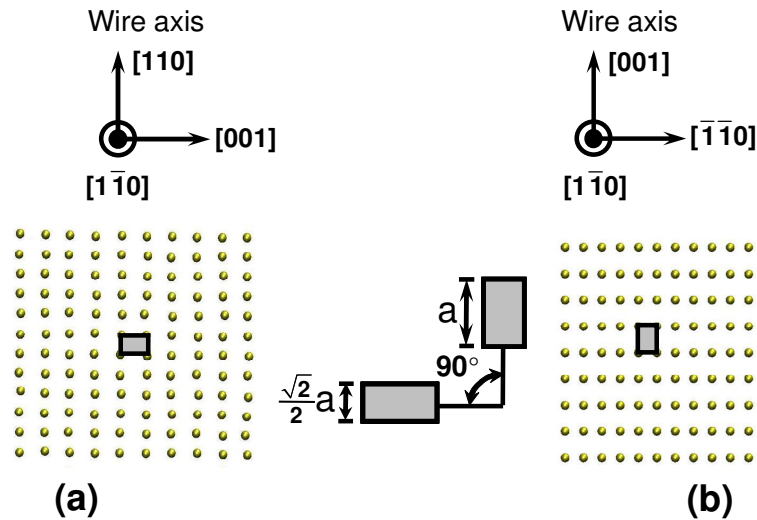
Figure 5.9 Reversible lattice rotation illustrated by the unit cells on $(1\bar{1}0)$ atomic plane, (a) section A-A in Figure 5.5(a) which is a $(1\bar{1}0)$ atomic plane containing the [110] wire axis and the long diagonal ([001]) of the rhombic cross-section in the original wire, and (d) section B-B in Figure 5.5(b), which is the same $(1\bar{1}0)$ atomic plane as in (a) after lattice reorientation, containing the new wire axis ([001]) and a diagonal ($[\bar{1}\bar{1}0]$) of the new square cross-section.

5.3 Quantification of the Large Transformation Strains

The large strains associated with the forward and reverse lattice reorientations can be quantified by a simple crystallographic analysis. The analysis shows that the reversible strains are proportional to the volume fraction of the reoriented lattice, and the maximum strain is 41% for a complete lattice reorientation. Specifically, Figure 5.9(a, b) compares the same $(1\bar{1}0)$ plane in the <110>/{111} (at point A in Figure 5.1(a)) and the <001>/{001} configurations (at point C in Figure 5.1(a)). Clearly, the forward (loading) and backward (unloading) lattice reorientations manifest as 90° rotations in opposite directions of the unit cell in the $(1\bar{1}0)$ plane. The length and width of the rectangular unit cell in both cases are, respectively, a and $\frac{\sqrt{2}}{2}a$; where a is the lattice constant in the stressed states and is assumed to be the same at A and C. Hence, the axial strain associated with the lattice reorientation between A and C is given by

$$\varepsilon_{<110>\to<001>} = \left(a - \tfrac{\sqrt{2}}{2}a\right)/\tfrac{\sqrt{2}}{2}a = 0.414 . \qquad (5.4)$$

On the other hand, if we consider the reverse lattice reorientation from <100>/{100} to <110>/{111} configuration with the <100>/{100} configuration being the reference state, then the strain is given by,

$$\varepsilon_{<001>\to<110>} = \left(\tfrac{\sqrt{2}}{2}a - a\right)/a = 0.293 \qquad (5.5)$$

Both the strains associated with the forward and reverse lattice reorientations are consistent with the phenomenological continuum quantification in chapter 4.

Clearly, $\varepsilon_{<110>\leftrightarrow<001>}$ is an attribute of the FCC structure and is independent of a. Consequently, the pseudoelastic strain associated with the lattice reorientation which constitutes the primary part of the total recoverable strain (ε_r) is the same for wires of all FCC metals and of all sizes. Equation (5.4) gives the recoverable strain associated with full transformations without residual defects and agrees well with the results of atomistic

simulations for Cu and Ni wires. Au wires show smaller $\varepsilon_{<110>\leftrightarrow<001>}$ because of the incomplete lattice reorientation. In that case, $\varepsilon_{<110>\leftrightarrow<001>}$ is proportional to the volume fraction of the transformed lattice.

In addition to $\varepsilon_{<110>\leftrightarrow<001>}$, ε_r also includes the elastic strain $\varepsilon^e_{<110>}$ associated with the lattice stretching in the <110>/{111} configuration between O and A (Figure 5.1(a)) and the elastic strain $\varepsilon^e_{<001>}$ associated with the lattice stretching in the <001>/{001} configuration between C and D, i.e.,

$$\varepsilon_r \approx \varepsilon^e_{<110>} + \varepsilon_{<110>\leftrightarrow<001>} + \varepsilon^e_{<001>} . \tag{5.6}$$

$\varepsilon^e_{<110>}$ and $\varepsilon^e_{<001>}$ are small compared with $\varepsilon_{<110>\leftrightarrow<001>}$, and they also vary with material and wire size. As shown in Figure 5.1(a) and Figure 5.2, ε_r are approximately 51% and 45% for Cu and Ni wires, respectively. In particular, for the 1.8×1.8 nm Cu nanowire in Figure 5.1, $\varepsilon_r \approx 0.048 + 0.415 + 0.049 = 0.512$. The ε_r for Au wires depends on temperature and is 0.32, 0.20, 0.07 at 5, 50, and 200 K, respectively.

5.4 Driving Force

The pseudoelastic behavior of SMAs arises from two related but somewhat different mechanisms which yield very similar stress-strain relations like those in Figure 5.1. The first mechanism is superelastic and involves a martensitic phase transformation driven by the free energy difference between the parent and product phases. The second mechanism is rubber-like and occurs solely within the martensitic state through reversible movement of twin boundaries (Cahn 1995; Otsuka and Wayman 1998). This mechanism is driven by a general tendency for the equilibrium symmetry of the short-range order configuration of lattice imperfections to conform to the symmetry of the lattice. Hence,

58

aging in the martensitic state and the existence of lattice imperfections are necessary conditions (Ren and Otsuka 1997). Clearly, the mechanism responsible for the pseudoelastic behavior of the nanowires analyzed here is more rubber-like than superelastic because the deformation occurs solely within the FCC structure, without any phase change. However, neither aging nor lattice imperfections are involved. Then, what causes the <001>/{001} wire to spontaneously revert back to its original <110>/{111} configuration upon unloading, since both states have the same FCC crystalline structure and, perhaps, the same "stability"? The answer lies in the surfaces and the extremely high surface-to-volume ratios of nanowires which can significantly affect structural stability. Specifically, {111} surfaces in FCC metals have the lowest energy among all surfaces. For example, the surface energies of Cu {001} and {111} planes are 1.35 Jm^{-2} and 1.24 Jm^{-2}, respectively. This difference in surface energy causes the <110>/{111} configuration to have a lower energy and to be more stable compared with the <001>/{001} configuration.

A quantification of the difference in the potential energy as a function of wire size between the two configurations is given in Figure 5.10(a) for Cu. Specifically, the quantification is carried out by "slicing" <001>/{001} wires and <110>/{111} wires out of bulk Cu crystals with appropriate orientations and dimensions. The potential energy of the two configurations is computed after they reach their equilibrium states through conjugate gradient energy minimization using molecular statics (Payne et al. 1992). The potential energy difference primarily results from the difference in surface energy densities between {111} and {001} surfaces. The average potential energy per atom decreases with increasing wire size for each configuration because smaller wires have

larger surface-to-volume ratios. On the other hand, regardless of size, <110>/{111} wires always have lower energy levels compared with their deformed counterparts with the <001>/{001} configuration. Therefore, the <001>/{001} wire has a natural tendency for spontaneous reorientation back to the <110>/{111} configuration upon unloading. The reorientation essentially lowers the surface energy as a result of the increase in atomic density on surfaces when {001} surfaces reorganize into closely-packed {111} surfaces.
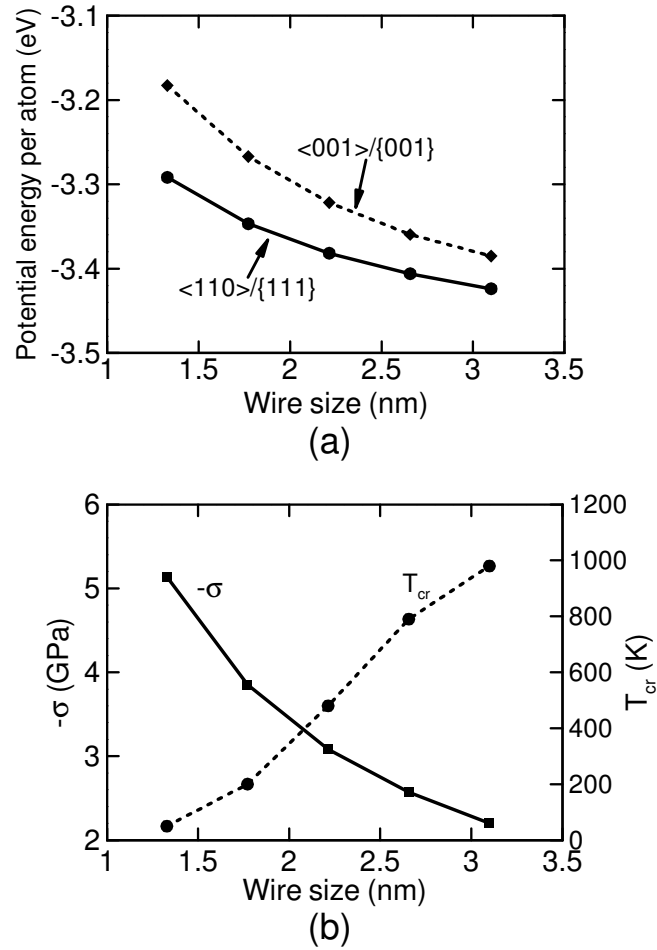
Figure 5.10 (a) a comparison of the potential energy per atom of Cu wires with the <110>/{111} and <001>/{001} configurations, (b) variations of the surface-stress-induced compressive stress σ and the critical temperature T_{cr} with wire size for Cu.

The driving force for the spontaneous reorientation can also be viewed as coming from the surface stress which induces a compressive stress in the interior of the wire. This compressive stress is $\sigma = -4fl/A$, where f is the surface stress of the {001} planes in the <001>/{001} configuration, l is the side length of the square cross-section (Figure 5.5(b)), and A $(=l^2)$ is the corresponding cross-sectional area. Obviously, the magnitude of σ increases as the wire size decreases and can be very high at the nanoscale, as shown in Figure 5.10(b). For example, $\sigma = -3.85$ GPa for a <001>/{001} Cu wire with l=1.45 nm (l_0=1.8 nm in the <110>/{111} state), sufficient for initiating the reverse reorientation at temperatures above 200 K, even in the absence of externally applied forces. Note, however, that σ is only on the order of Pascals in bulk materials and is negligible, providing an explanation as to why a similar behavior is not seen in bulk metals.

5.5 Shape Memory Effect

5.5.1 Critical Temperatures for Spontaneous Transformation

Like the behavior of normal bulk SMAs, the pseudoelastic behavior of Cu wires reported here is strongly temperature-dependent. Specifically, the reverse lattice reorientation from <001> to <110> occurs only above a size-dependent critical temperature T_{cr} (Figure 5.10(b)). If unloading takes place at temperatures below T_{cr}, the reverse lattice reorientation does not occur and the wire retains the <001>/{001} configuration. When subsequently heated above T_{cr}, the unloaded <001>/{001} wire spontaneously returns to its original <110>/{111} configuration through the reverse lattice reorientation. This is a novel SME driven by surface stress and the high surface-to-

volume ratios of the nanowire. It is a one-way SME that has the <110>/{111} configuration as the parent state, as illustrated in Figure 5.11.
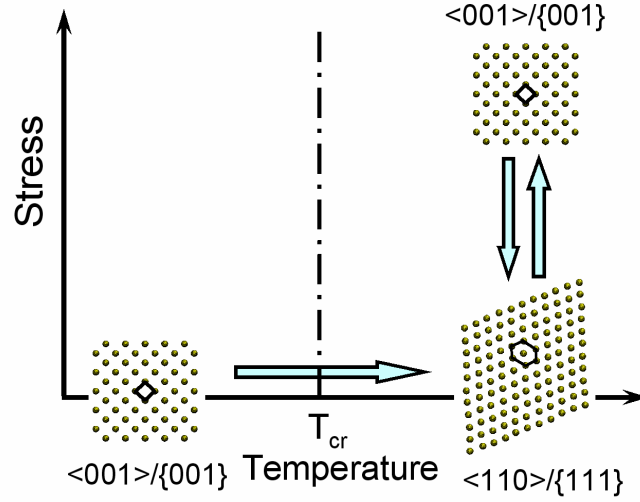
Figure 5.11 An illustration of the shape-memory effect in Cu nanowires, T_{cr} is the critical temperature for a Cu nanowire of a certain size to fully reconstruct or show the effect.

The value of T_{cr} is obtained by gradually heating a <001>/{001} wire until lattice reorientation occurs. The heating starts at 0 K and the temperature is increased by 10 K in each heating step. At each temperature, the wire is relaxed for 150 ps. The reorientation is identified by monitoring the potential energy change during heating. Specifically, the potential energy increases proportionally with temperature if there is no lattice reorientation. However, the potential energy drops precipitously at the occurrence of the lattice reorientation, allowing the onset of the latter to be determined, as shown in Figure 5.12.
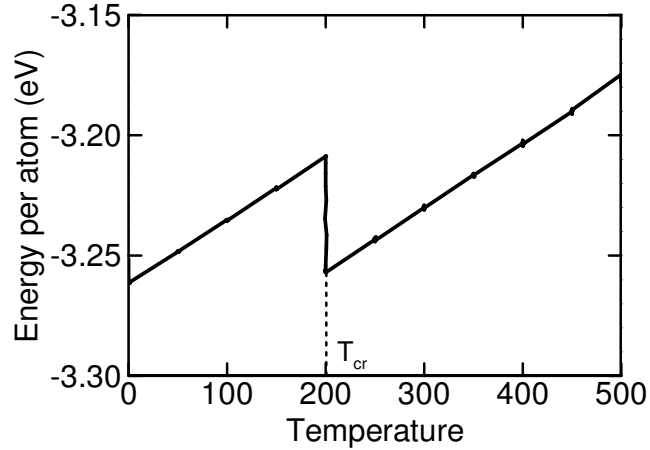
Figure 5.12 The variation of energy per atom with temperatures during heating for a 1.45×1.45 nm Cu wire, the precipitous energy drop at T_{cr} indicates the onset of lattice reorientation.

It is important to point out that, like in all MD models, the accuracy of the simulations carried out here depends on the atomic potential used. Since the critical temperatures and sizes for transformation are closely related to {111} and {001} surface energies and surface stresses and different atomic potentials for Cu predict different surface energies for {111} and {001} surfaces (Foiles et al. 1986; Baskes 1992; Wang et al. 1999), the predicted critical condition in terms of temperature and size may vary from potential to potential. However, the overall trend and dependence are expected to be the same regardless of which potential is used. More importantly, it must be noted that it is the *difference* in the surface energies for {111} and {001} surfaces, not the absolute surface energy values, that determine the nature of the observed transformation. Since the difference is found to be of the same order in all the Cu potentials (Foiles et al. 1986; Baskes 1992; Wang et al. 1999; Zhang et al. 2004), it is expected that different potentials would still lead to predictions of similar structural behaviors. Indeed, the same transformation mechanism and behavior have been observed in simulations carried out using the EAM potential for Cu in reference (Foiles et al. 1986). In addition, similar

transformation mechanisms are observed by Diao et al. for surface stress driven lattice reorientation in Au nanowires when different atomistic potentials, including an EAM, a modified embedded atom method (MEAM), and a surface embedded atom potential (SEAM), are used (Diao et al. 2004).

If the <110>/{111} state always has a lower energy than the corresponding <001>/{001} state regardless of size, why does the reverse reorientation only occur above T_{cr}? The answer has to do with the energetic barrier and driving force for the process. To initiate the reorientation, partial dislocations nucleate and propagate to accommodate mobile twin boundaries. These defects are of higher energies and thus constitute an energy barrier for the reorientation, which is closely related to unstable stacking fault energy. Thermal energy can provide the necessary energy for overcoming the barrier. As wire size increases, σ decreases and higher temperatures are needed to initiate the spontaneous reverse reorientation, as shown in Figure 5.10(b). This size- and temperature- dependence is frequently observed in experiments. For example, at a given temperature <001>/{001} Au nanowires and nanofilms are observed to reorient into the <110>/{111} configuration only when their size is reduced to less than 2 nm by electron beam irradiation (Kondo and Takayanagi 1997; Kondo et al. 1999). On the other hand, because of the high energy barrier in Ni, the surface stress induced compressive stress alone can not initiate the spontaneous lattice reorientation in Ni wires upon unloading even at very high temperatures. Therefore, external compressive stress is needed for the reverse lattice reorientation. Similar to the temperature effect in Cu wires, less external compressive stresses is needed as temperature increases in Ni wires.

It is illustrative to point out that the behavior discovered here is likely to be specific to the <110>/{111} and <001>/{100} configurations. Experiments and

computations have shown that the axes of most FCC metal nanowires are in the <001>, <110>, or <111> orientations (Rodrigues and Ugarte 2003). The first two orientations are involved in the reorientation processes discussed in this paper. The third orientation involves nanowires with <111> axes and {111} cross-sections. Calculations carried out in this work show that such wires do not exhibit the pseudoelasticity and SME the <110>/{111} and <001>/{100} wires show. This is perhaps partly because the <111> axes and {111} cross-sections of these wires give rise to smaller resolved shear stresses (RSS) on the $\frac{a}{6}\{111\}\langle11\overline{2}\rangle$ slip systems which are a driving force for the partial dislocation nucleation and lattice reorientations responsible for the SME observed here.

The T_{cr} and wire size for relaxation are closely related to the {111} and {001} surface energies, surface stresses, and unstable stacking fault energy of each metal. Therefore, the size-dependent T_{cr} varies from material to material. For example, Cu wires with lateral dimensions between 1.3 and 3.1 nm exhibit SME with T_{cr} ranges from 50 to 1000 K. However, T_{cr} for Ni wires of the same size range are so high that it approaches a significant fraction of the melting point. Under such conditions, the SME is no longer obvious because the wire behavior becomes disorganized and dominated by random thermal vibrations. On the other hand, Ni wires with defects can exhibit SME because T_{cr} can be lowered by surface and internal structural defects such as vacancies, kinks, and local lattice distortions. Specifically, the presence of defects lowers the T_{cr} and essentially shifts the SME toward larger wires because higher energies associated with disorders facilitate the initiation of twin boundaries. These defects may result from manufacturing processes and can also be nucleated and annihilated during cyclic loading and unloading. Defects may also affect the stress-strain responses and reduce ε_r by causing incomplete

reorientation, as discussed earlier. However, this effect may be relatively small as shown in Figure 5.1(b), if the initial state of the wires is nearly defect-free. In summary, the material- and size-dependence of T_{cr} suggest a new class of nano building-blocks with an SME useful over a wide range of temperature.

(a)   (b)
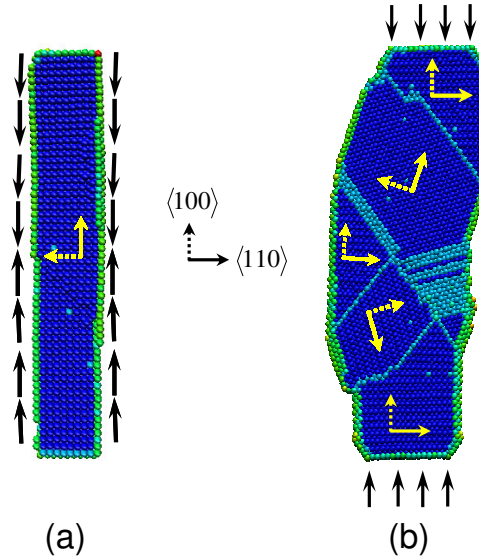
Figure 5.13 Size effect on the shape memory of metal nanowires: (a) a 1.45×1.45 nm Cu wire fully reoriented under surface stress, (b) a 3.6×3.6 nm <100>/{100} Cu wire partially reoriented under external compression, the yellow coordinate axes indicate the different orientations of the grains separated by twin boundaries. Atoms are colored according to their centrosymmetry values.

5.5.2 Effect of Size on SME

FCC metals in bulk have not been known to possess shape memory. One logical question is why FCC nanowires exhibit shape memory and pseudoelasticity but their bulk counterparts do not. The reason lies in their extremely small sizes at the nanometer scale and their unique 1D structure.

First of all, it has been demonstrated that twinning is vital to the pseudoelasticity in the nanowires. Slip is generally favored over twinning in bulk FCC metals under normal loading conditions. Twinning becomes a viable deformation mode only when the dominant size (e.g., grain size or wire size) scale approaches nanometers. Both experiments and simulations have shown that twinning is the primary deformation mechanism in nanocrystalline metals, nanowires, and nano particles (Field et al. 2004). This size dependence of deformation mechanisms may be related to the width of stable stacking faults in FCC metals. Specifically, stable stacking faults are bound by Shockley partial dislocations formed through the dissociation of full $\frac{1}{2}\langle 110 \rangle$ dislocations, as illustrated in equation (5.1). The separation distance between the two partials (d_{sep}) is primarily determined by the balance of two forces, the elastic repulsion between the partials and the attractive "glue" force due to the intrinsic stacking faults. Specifically, the continuum elasticity theory gives the equilibrium separation distance by

$$d_{sep} = \frac{7G|\mathbf{b}_1 \bullet \mathbf{b}_2|}{16\pi\gamma_{sf}} \tag{5.7}$$

where G is the shear modulus, $\mathbf{b}_1$ and $\mathbf{b}_2$ are the Burger's vectors of the two Shockley partials, respectively. In the above equation, the two partials are considered as separate dislocations connected by the intrinsic stacking faults. Alternatively, the whole assembly of the two partials and the stacking fault can be viewed as the extended core of a full dislocation. The core size of the full dislocation is the same as d_{sep}, which is inversely proportional to γ_{sf}. Specifically, d_{sep} is smaller in metals with low γ_{sf}, and larger in metals with high γ_{sf}. Overall, both d_{sep} and the wire sizes considered in this research are of the order of nanometers, see Table 3.2. When d_{sep} is larger than wires, the cores of full

dislocations can not exist in wires, hence slip is unlikely to occur. Conversely, twinning becomes more likely in nanocrystalline metals or nanowires. On the other hand, d_{sep} is far smaller than the characteristic lengths (usually the grain sizes) of bulk metals. Therefore, bulk metals usually deform via slip.

Secondly, nanowires have extremely large surface-to-volume ratios. Specifically, a nanowire has a surface-to-volume ratio 10^6 times that of a macroscopic specimen (Liang and Zhou 2005). The fraction of surface atoms is around 39.5% for a 1.8×1.8 nm nanowire while that for bulk metals approaches zero. As previously discussed, the high surface-to-volume ratios induce high values of internal compressive stress σ which are on the order of GPa, providing the necessary driving force for the reverse reorientation above T_{cr}, even in the absence of externally applied forces, as shown in Figure 5.13(a). On the other hand, σ is only on the order of Pascals in bulk materials, far from being sufficient to initiate spontaneous lattice reorientations. One may still wonder if a bulk FCC crystal with the <110>/{111} configuration would exhibit the lattice reorientation leading to pseudoelasticity and shape memory in nanowires under the condition that an external compressive stress of sufficient magnitude is applied. The answer is still "no" because the reversibility of the reorientation process primarily results from the unique 1D structure at the nanoscale. This structure acts as a channel, limiting the propagation of twin boundaries to the direction of the wire axis. The opposite directions of twin boundary propagation during loading and unloading give rise to the reversible nature of deformations, as shown in Figure 5.13(a). As the lateral dimensions increase, the wire gradually becomes a 3D structure with multiple modes of defect nucleation, propagation and interaction. Such a 3D structure leads to simultaneous twin boundaries and stacking

faults at multiple sites and in multiple directions (Liang and Zhou 2004), as shown in Figure 5.13(b). The entanglement and interactions of these defects reduce the mobility of the twin boundaries and ultimately preclude the occurrence of the pseudoelasticity and the shape memory. Under such conditions, the wires are essentially a polycrystal with grains separated by interlocking twin boundaries.

5.6 Chapter Summary and Insights

The mechanical behavior of Cu, Ni, Au, and Al nanowires with lateral dimensions between 1-5 nm and <110>/{111} configurations are analyzed using MD simulations. Upon tensile loading and unloading, Cu and Ni wires exhibit a novel pseudoelastic behavior with large reversible strains of up to 50%, well beyond the recoverable strains of 5-8% typical for most bulk shape memory alloys (SMAs). In comparison, the tensile deformations of Al wires are irreversible upon unloading. Au wires show a transition of behavior from pseudoelasticity at low temperatures to plasticity at high temperatures and have temperature-dependent reversible strains which decrease with temperature.

The difference in behavior among wires of different materials is due to two competing deformation mechanisms, i.e., twinning and slip. Specifically, FCC metals with high twinnability (such as Cu, Ni, and Au) favor twinning which leads to the pseudoelastic behavior and SME in their nanowires. On the other hand, FCC metals with low twinnability (such as Al) favor slip which leads to irreversible deformations even at the nanoscale.

A temperature-dependent spontaneous lattice reorientation enables wires in the <100>/{100} configuration to revert to the <110>/{111} configuration through heating. This temperature effect leads to an SME in Cu wires and in Au wires at lower

temperatures. Specifically, the <110>/{111} configuration is more stable than the <100>/{100} configuration primarily because {111} surfaces have a lower surface energy than that of {100} surfaces. Driven by the high surface-stress-induced internal stresses at the nanoscale, {100} surfaces spontaneously reconstruct into lower energy {111} surfaces as part of the lattice reorientation process to lower the overall free energy. This spontaneous process only occurs at temperatures above a critical value T_{cr} which is material specific. This is because sufficient thermal energy is required to overcome the energy barrier for initiating the process. For each material, T_{cr} increases with wire size because the driving force is smaller in larger wires and hence a higher amount of thermal energy is needed.

The unique pseudoelasticity and SME only exist in nanowires of FCC metals with high twinnability, but not in their bulk form. This size effect is primarily due to three reasons: (i) the small size scales in FCC metals make twinning the favored deformation mechanism, (ii) the surface-stress-induced internal compressive stress in nanowires is on the order of GPa because of their high surface-to-volume ratios and this internal compressive stress provides the necessary driving force for a spontaneous lattice reorientation without external influence, and (iii) the reversibility of the lattice reorientation process is derived from the unique 1D structure of the nanowires. As their lateral dimensions increase, nanowires become 3D structures. Under such conditions, the interaction and entanglement of twin planes transform the wires into polycrystals and ultimately preclude the occurrence of the lattice reorientation which is the mechanism for the pseudoelasticity at the nanoscale.

CHAPTER 6 A MICROMECHANICAL CONTINUUM MODEL FOR STRESS-INDUCED LATTICE REORIENTATION

The previous chapter has reported a novel shape memory behavior in metal (Cu, Ni, and Au) nanowires, which are associated with a unique reversible lattice reorientation proceeding with twin boundary propagation. This unique transformation mechanism is similar to but not exactly the same as those in bulk SMAs. Specifically, there are clear size effects primarily due to the high surface-to-volume ratios. Moreover, the driving force in bulk SMAs usually comes from the difference of the chemical free energies. In contrast, the driving force for lattice reorientation comes from the surface energy difference between {111} and {100} surfaces. Since most of the previous continuum models on SME do not consider size effects and free surface effects, they can not be directly used to model the SME in metal nanowires.

The principal interest of this chapter is to develop a micromechanical deformation mechanism-based continuum model to characterize the unique behavior of the nanowires under isothermal quasistatic deformations. Based on the first law of thermodynamics, this model treats the twin boundary propagation process as a sequence of static equilibrium (metastable) states superimposed with dissipative twin boundary propagation process. The static equilibrium states are modeled within the framework of strain energy function with multiple local minima (Abeyaratne et al. 2001). The detailed analysis of the mechanism of twin boundary propagation show that the energy dissipation results from the ruggedness of strain energy landscape associated with dislocation nucleation, gliding, and annihilation during lattice reorientation. The model captures the major characteristics of the unique behavior due to lattice reorientation and accounts for the size and temperature effects. The model predictions show excellent agreement with molecular dynamics simulation results.

6.1 Introduction

As previously discussed, the lattice reorientation involves two wire configurations: the <110>/{111} and <100>/{100} configurations. Although both wire configurations have the same FCC structure, <110>/{111} wires have lower free energy than <100>/{100} wires because {111} surfaces have lower energies than {100} surfaces and surface energies dominate the total free energies of nanowires due to the extremely high surface-to-volume ratios. Consequently, the <110>/{111} wires are more stable and have been frequently observed in experiments and computer simulations (Kondo and Takayanagi 1997; Rodrigues et al. 2002; Diao et al. 2004; González et al. 2004; Liang and Zhou 2005; Liang et al. 2005; Liang and Zhou 2006; Park and Zimmerman 2006). Due to the different free energy and stability, we call these two wire configurations as two phases in the following discussions. During lattice reorientation (or phase transformation), the two phases coexist, separated by phase interface, which is a coherent twin boundary. The phase transformation proceeds as the twin boundary propagates along the wire axis.

With regard to modeling of phase transformations, Abeyaratne and Vedantam (2003), Abeyaratne and Knowles (1993), and Abeyaratne and Kim (1994) presented a framework based on theory of the strain energy functions with multiple local minima, with each local energy well corresponding to a phase or variant of the material. As the load is varied, the relative stability of each phase changes and the less stable phase transform into the more stable phase through the propagation of the phase boundary. The initiation of the phase transformation is governed by a nucleation condition, and the rate of transformation or how fast the phase boundary propagates is governed by a kinetic law. In this framework, a thermodynamics driving force is defined by the states at the vicinity of the phase boundary. For example, in one-dimension,

$$f = [\![w]\!] - \langle\sigma\rangle[\![\varepsilon]\!] \tag{6.1}$$

where $[\![w]\!]$ denotes the jump of strain energy density across the phase boundary, $\langle\sigma\rangle$ denotes the average stress at the vicinity of the phase boundary, and $[\![\varepsilon]\!]$ denotes the strain jump across the phase boundary. The kinetic law determines the relation between the speed of phase boundary (v) and the driving force (f), i.e.,

$$f = \varphi(v) \tag{6.2}$$

where the f must satisfy the following inequality of dissipation associated with the phase boundary propagation,

$$fv \geq 0. \tag{6.3}$$

The preceding framework has been successful in modeling the martensitic transformations in bulk SMAs, especially for static problems. However, one difficulty with the framework is the construction of accurate strain energy functions. Many strain energy functions can only qualitatively capture the characteristics of phase transformation, but fail to provide a quantitatively accurate model, primarily because of the restrictive nature of kinematics constraints (Abeyaratne et al. 2001). Moreover, there are more difficulties in using the preceding framework for dynamic problems, e.g. the lack of accurate kinetic law and quantitative information regarding energy dissipation. Accurate kinetic laws are difficult to obtain because they are unrestricted by continuum theory except having to satisfy the dissipation inequality. Usually, lattice-based models are required to analyze the many factors determining kinetic laws (Abeyaratne and Knowles 1991). The dissipation inequality only tells that the energy dissipation must be greater than zero, but it does not give any quantitative information. Nonetheless, the quasistatic phase transformation process has to be analyzed as dynamic processes because the driving force $f \neq 0$.

To avoid the difficulties in the analysis of the dynamic processes within the preceding framework, the present model treats the quasistatic lattice reorientation process as a sequence of static states superimposed with a phase boundary propagation process

73

based on the first law of thermodynamics. Then these two processes are analyzed independently.

The static phase equilibrium problem is studied by constrained strain energy minimization within the preceding framework without the necessity of kinetic laws. Instead of constructing the complete strain energy functions over a full 3D strain space, we only consider the 1D strain energy function because of the 1D wire structure and the 1D nature of uniaxial tensile deformations. Moreover, we neglect the part of strain energy function corresponding to the unstable states and only use the part of strain energy functions around the local energy minima, where phases are stable. Specifically, we only consider the strain energy functions corresponding to the elastic deformations of the two pure phases involved in lattice reorientation. Therefore, the accurate strain energy function can be easily obtained from experiments, MD simulations, and even analytical expressions (discussed later in section 6.2) with the bulk and surface elastic constants. Since the strain energy functions of pure phases already account for the significant surface energies in nanowires, the model will automatically account for the size dependence of the behavior.

For the twin boundary propagation process, our goal is to quantify the associated energy dissipation. Since our interest is quasistatic process, we do not attempt to explicitly calculate the driving force or derive an explicit kinetic law to determine the relation of the driving force and phase boundary propagating speed. Instead, we study the source of energy dissipation by analyzing the lattice scale deformation mechanism in detail. The analysis reveals that the energy dissipation is due to the ruggedness of energy landscape associated with dislocation nucleation, propagation, and annihilation. Moreover, the dissipation energy has a linear relation with the external strain. The temperature dependence of energy dissipation is also analyzed in the perspective of energy barriers for dislocation nucleation.

The organization of this chapter is as follows. Section 6.2 studies the strain energy and stability of nanowires. Specifically, the strain energy of nanowires is modeled as the sum of bulk strain energy and surface free energies. The dominance of surface energies is clearly illustrated. We also demonstrate that the strain energy does not vanish in unstressed wires and there is a surface-stresses-induced compressive stress. In section 6.3, we present the piecewise smooth model with each piece corresponding to one deformation stage. Particularly, we focus on the modeling of quasistatic lattice reorientation process, which is treated as a smooth transition between a sequence of phase-equilibrium states superimposed with a phase boundary propagation process. In subsection 6.3.3, the static problem is solved by constrained minimization of strain energy functions. In section 6.3.4, relation of energy dissipation with strain is derived the from the rugged energy landscape associated with dislocation nucleation, propagation, and annihilation during lattice reorientation. In section 6.4, MD simulations are carried out to verify the model. The model predictions show excellent agreement with MD simulations results. Finally, the chapter is concluded in section 6.5 with a summary of insights.

6.2 Strain Energy in Nanowires

The <110>/{111} and <100>/{100} wire configurations have different elastic constants and strain energies during elastic deformation, although both configurations have FCC crystalline structure. The strain energies of these two phases are critical to the lattice reorientation because the strain energies determine the relative stability of the two phases.

Compared to the strain energy of bulk materials, the strain energy of nanowires is not only a function of strains, but also the wire sizes. Furthermore, the strain energy of nanowires does not vanish at zero strain. These special characteristics primarily originate from the large surface-to-volume ratio of nanowires.
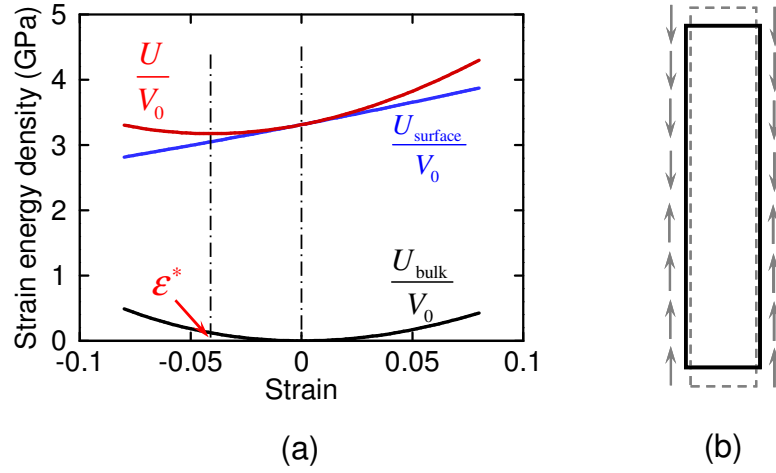
Figure 6.1 (a) the strain energy density function and its bulk and surface components of a 1.9×1.9 nm Cu wire, the reference state is the undeformed bulk lattice, (b) schematic illustration of the contraction of a wire under surface stress

We know atoms on or near free surfaces have different energies from those in the bulk because surface atoms experience a different local environment from those in the bulk of a material. Such surface effects are usually insignificant and negligible in bulk materials because the number of surface atoms is small compared to the total number of atoms. However, these surface effects can be substantial for nanowires because of the extremely large surface-to-volume ratios. For example, the surface-to-volume ratio of a 1.8×1.8 nm nanowire is 10^6 times larger than that of a typical macroscopic tensile specimen (Liang and Zhou 2005). The surface energy constitutes a significant portion of the total strain energy of the wire. Taking surface energies into account, the strain energy of nanowires can be written in the following form (Streitz et al. 1994; Dingreville et al. 2005).

$$U = U_{bulk} + U_{surface} ,$$

(6.4)

where U_{bulk} is the strain energy in the bulk of the wire, and $U_{surface}$ is the surface free energy. Specifically the strain energy for the <110>/{111} wire with lateral size d_0 and length l_0 (see Figure 5.5(a)) is

$$U_{110} = u_{110}(\varepsilon) d_0^2 l_0 \sin\theta + 4\gamma_{111} d_0 l_0 \qquad (6.5)$$

where $u_{110}(\varepsilon)$ is the strain energy of bulk materials stretched in the <110> orientation, $\theta = 70.5°$ is the sharp angle of the rhombic cross-section, and γ_{111} is the surface energy of {111} surfaces. Similarly, the strain energy for a <100>/{100} wire with lateral size d and length l (see Figure 5.5(b)) is

$$U_{100} = u_{100}(\varepsilon) d^2 l + 4\gamma_{100} d l \qquad (6.6)$$

where $u_{100}(\varepsilon)$ is the strain energy of bulk materials stretched in the <100> orientation and γ_{100} is the surface energy of {100} surfaces. Figure 6.1 shows the total strain energy and its two components, U_{bulk} and $U_{surface}$, of a of 1.45×1.45 nm <100>/{100} wire. Clearly, $U_{surface}$ dominates the total strain energy due to the extremely high surface-to-volume ratio.

We can also see that the strain energy function does not vanish at zero strain. This is because the minimum strain energy point, which corresponds to the unstressed self-equilibrium state, is at a compressive strain (Dingreville et al. 2005). The compressive strain at self-equilibrium state is induced by surface stress in nanowires. Consider a wire just cutting from a bulk, the wire will contract in axis direction and expands in lateral direction because of tensile surface stresses, as shown in Figure 6.1(b). The axial contraction causes a compressive stress σ in the core of the wire, which is balanced by the tensile surface stress at equilibrium states. The magnitude of σ is inversely proportional to the lateral size of the wire. In nanowire, σ is of the order of GPa. In contrast, σ is only on the order of Pascals in bulk materials and thus is negligible.

The self-equilibrium strain ε^* can be obtained analytically by minimizing the strain energy in equation (6.4).

$$\left.\frac{\partial U}{\partial \varepsilon}\right|_{\varepsilon=\varepsilon^*} = 0 \qquad (6.7)$$

In MD simulations, ε^* can be obtained by simulating a top-down nanowire fabrication process, which involves cutting a wire from bulk and relaxing the wire at a constant temperature until it reaches the self-equilibrium state. ε^* can then be calculated from the original length and the length at the self-equilibrium state.

ε^* is related to wire size and configurations (wire axis orientation and transverse surfaces). For the wires of the same configuration, ε^* is smaller in larger wires. For the wires of the same size, ε^* of <110>/{111} wires is smaller than that of the <100>/{100} wires. For example, ε^* equal to 0.02 and 0.04, respectively, for a 1.8×1.8 nm <110>/{111} Cu wire and the corresponding <100>/{100} wire at 300 K.
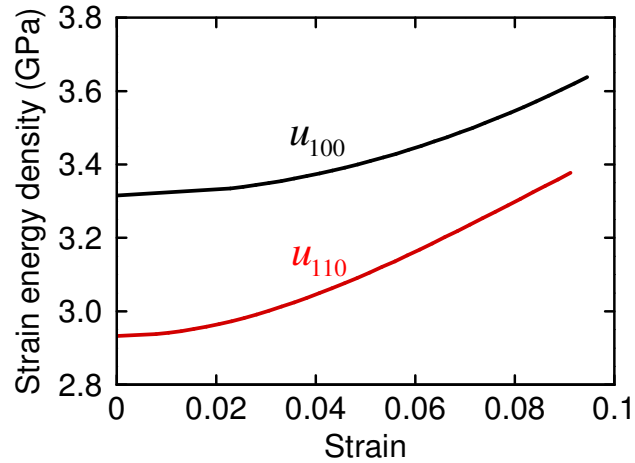
Figure 6.2 The strain energy density functions of a <110>/{111} and a <100>/{100} wires, the reference states are the unstressed states of corresponding phases, respectively.

In calculating ε^*, we have used the undeformed bulk lattices as the reference states to show the axial contraction under surface stress. However, in the following discussions, we use the unstressed self-equilibrium states of nanowires as the reference

78

states of the wires unless otherwise indicated. With these reference states, the stress is zero at zero strain. Moreover, the wire has the minimum strain energy at the reference states. It is important to point out that the actual strain energy values also depend on the selected ground zero energy state. In this study, the ground zero energy state is the undeformed bulk lattice and strain energy of nanowires does not equal to zero at the reference states. As shown in Figure 6.2, the strain energies at the reference states are 2.95 GPa and 3.24 GPa for the <110>/{111} and <100>/{100} phases, respectively. In the next section, the constitutive model will be derived based on the strain energy functions of <110>/{111} and <100>/{100} wires as shown in Figure 6.2.
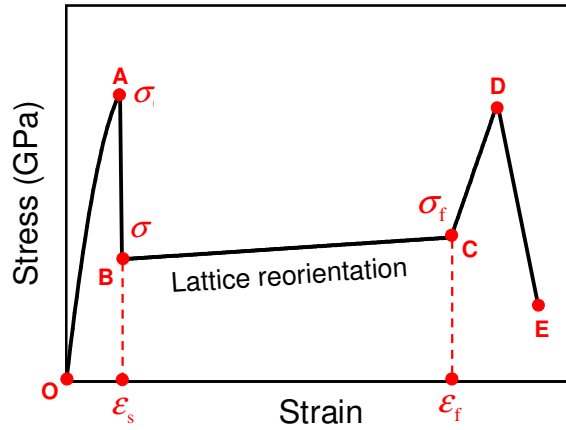
Figure 6.3 A schematic stress-strain curve of a nanowire under isothermal quasi-static tensile deformation

6.3 Mechanism-based Constitutive Model

As discussed in section chapter 5, the tensile deformation behavior of wires can be partitioned into four deformation stages according to underlining deformation mechanisms. We will only discuss the first three stages (till point D in Figure 6.3) because only their associated deformations are reversible upon unloading. The constitutive model is piecewise smooth with each piece associated with a deformation stages. Particularly, this model focuses on the lattice reorientation because it is this

unique deformation mechanism that leads to the novel SME of metal wires with large reversible strains. The model will capture the following major characteristics of unique tensile behavior due to lattice reorientation (see Figure 6.3):

(1) The elastic deformation of the <110>/{111} phase (O→A)

(2) Point A indicating the yielding of the <110>/{111} phase through the nucleation of a Shockley partial dislocation, σ_{s0} is the yielding stress.

(3) The precipitous drop of stress due to the gliding of the partial (A→B). This stress drop also corresponds to the formation of the twin boundary when the partial glides across the wire and annihilates on the free surface.

(4) Lattice reorientation from <110> to <100> through twin boundary propagation (B→C), ε_s and ε_f are the strains at the initiation and completion of the lattice reorientation, respectively. And σ_{s1} and σ_f are the stresses at the initiation and completion of the lattice reorientation, respectively.

(5) The elastic deformation of the <100>/{100} phase (C→D)
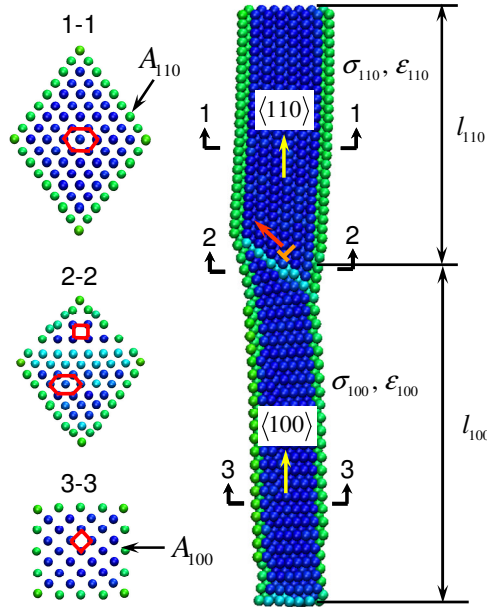
Figure 6.4 A phase-equilibrium state during lattice reorientation

80

Before we introduce the model, it is important to clarify the definitions of the several stresses and strains involved in this analysis. The stress σ and strain ε in the stress-strain curve in Figure 6.3 are the total nominal stress and strain with the assumption that stresses and strains are uniform throughout the wire, although there are actually two phases coexisting during lattice reorientation and the stresses and strains are not necessarily the same in the two phases. Specifically, ε is the nominal engineering strain with the initial unstressed <110>/{111} wire as the reference state. Hence, ε is given by

$$\varepsilon = \frac{\delta}{l_0} \tag{6.8}$$

where δ is the total displacement and l_0 is the length of the initial unstressed <110>/{111} wire at a given temperature. During deformation, the total mechanical work done by external load is given by

$$W = V_0 \int_0^\varepsilon \sigma d\varepsilon \tag{6.9}$$

Accordingly, the total stress σ is given by

$$\sigma = \frac{1}{V_0} \frac{\partial W}{\partial \varepsilon} \tag{6.10}$$

where V_0 is the initial volume of the unstressed <110>/{111} wire.

In the following discussions, we also need to consider the local stresses (σ_{110} and σ_{100}) and strains (ε_{110} and ε_{100}) in the <110>/{111} and <100>/{100} phases, respectively, as shown in Figure 6.4. Specifically, ε_{110} and ε_{100} are engineering strains with the reference states being the unstressed <110>/{111} and <100>/{100} phases, respectively. And σ_{110} and σ_{100} are given by

$$\sigma_{110} = \frac{du_{110}}{d\varepsilon_{110}}, \text{ and} \tag{6.11}$$

$$\sigma_{100} = \frac{du_{100}}{d\varepsilon_{100}}. \tag{6.12}$$

6.3.1 Elastic Deformation of <110>/{111} Phase

Initially, the wire is in a single <110>/{111} phase state. Upon tensile loading, the <110>/{111} wire first go through elastic deformation (Segment OA in Figure 6.3) and all the input mechanical work is stored as strain energy (U_{110}) in the wire, i.e. $U_{110} = W$. Substituting U_{110} into equation (6.10) yields the stress strain relation

$$\sigma = \sigma_{110} = \frac{1}{V_0} \frac{\partial U_{110}}{\partial \varepsilon} = \frac{\partial u_{110}}{\partial \varepsilon}. \tag{6.13}$$

where u_{110} is the strain energy density function in Figure 6.2.
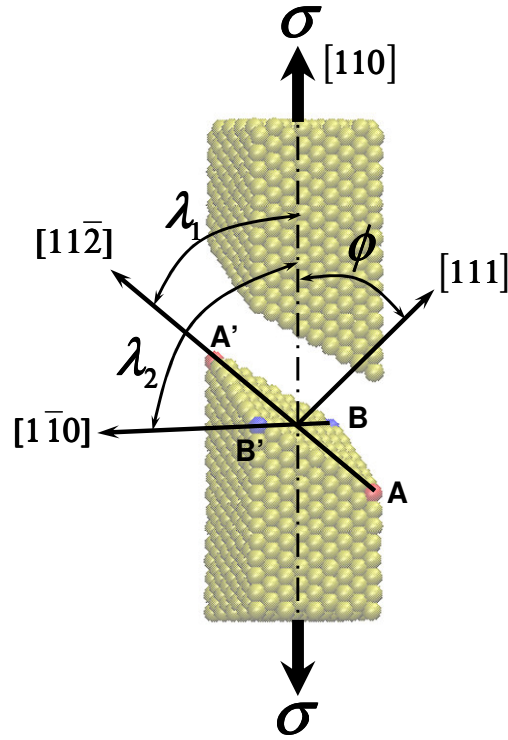

Figure 6.5 Two separated portions of a wire showing a model to calculate the resolved shear stress, σ is the external loading stress, ϕ is the angle between the loading direction and the normal to the {111} slip plane, λ_1 is the angle between the loading

direction and the $[11\bar{2}]$ slip direction for Shockley partial dislocation, and λ_2 is the angle between the loading direction and the $[1\bar{1}0]$ slip direction for full dislocation.

6.3.2 Dislocation Nucleation at the Initiation of Lattice Reorientation

The lattice reorientation begins when the <110>/{111} wire reaches its elastic limit at ε_s, as shown in Figure 6.3. Beyond ε_s, a single dislocation is emitted and glides across the wire, forming a coherent twin boundary. Therefore, the initiation of the lattice reorientation is essentially the same as the initiation of plasticity because both processes involve defect nucleation.

The dislocation nucleation in nanowires is heterogeneous because wires have large free surface-to-volume ratio and sharp interfacet edges due to the rhombic cross-section shape (Dumitrica et al. 2006). Various researchers have shown that that the lowest energy barrier for the nucleation of dislocations corresponds to a path that initiates from the free surface with or without defects (Trushin et al. 2002). Particularly, the four interfacet edges are the most probable nucleation sites because of the weak bonding of atoms. Consider a {111} slip plane shown in Figure 6.5. Vertices A and A' are the likely nucleation sites for $\frac{1}{6}(111)[11\bar{2}]$ Shockley partial dislocations because the long diagonal AA' coincides with the $[11\bar{2}]$ slip direction. Similarly, Vertices B and B' are the likely nucleation sites for $(111)[1\bar{1}0]$ full dislocations because the short diagonal BB' coincides with $[1\bar{1}0]$ slip direction. Using critical resolved shear stress (CRSS) criterion, we demonstrate that partial dislocation slip is more favorable than the full dislocation slip. Specifically, we know that the resolved shear stress (RSS) is given by

$$RSS = \sigma_l \cos\phi\cos\lambda \qquad\qquad (6.14)$$

where σ_l is the local stress at the nucleation sites, and $\cos\phi\cos\lambda$ is the Schmid factor. The Schmid factor for $(111)[1\bar{1}0]$ slip system equals to zero because the loading direction [110] is perpendicular to the slip direction $[1\bar{1}0]$, i.e. $\lambda = 90°$, as shown in Figure 6.5. This

makes the activation of $(111)[1\bar{1}0]$ slip systems highly unlikely. At the same time, the

Schmid factor for $(111)[11\bar{2}]$ is 0.43 with $\phi = 35.3°$ and $\lambda = 53°$. Moreover, the local

stresses σ_l at vertices A and A' is higher than that at vertices B and B' because of the

more atoms at vertices A and A' constitutes a weak spot because of lower coordination

numbers due to sharper angles. Consequently, $(111)[11\bar{2}]$ is more favored for nucleation,

which leads to a twinning deformation mechanism.
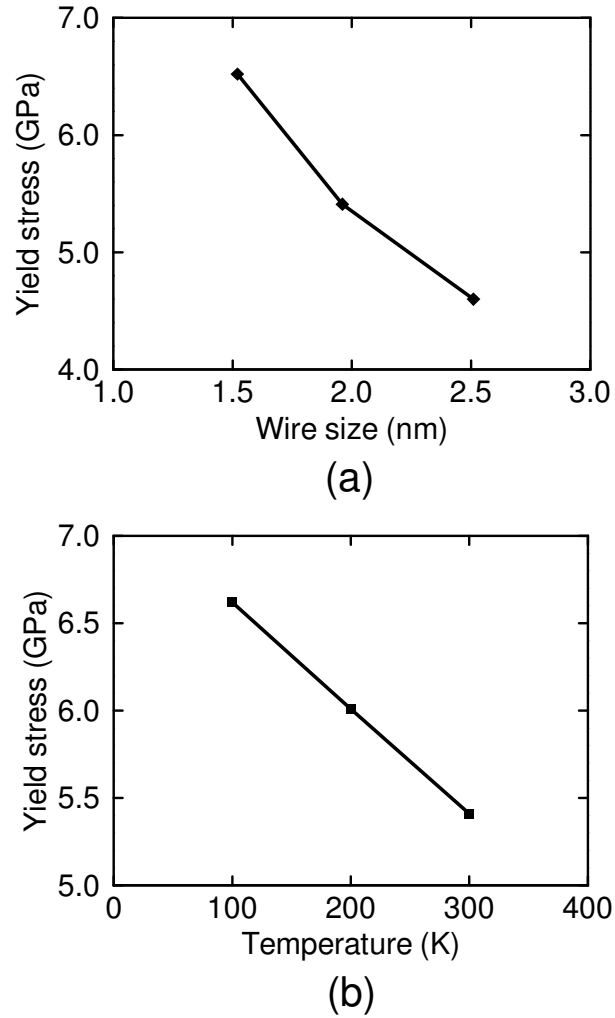
Figure 6.6 Size and temperature dependence of yield stress σ_{s0}, (a) the variation of σ_{s0}

with wire size, (b) the variation of σ_{s0} with temperature

The partial dislocation nucleates when the local RSS at the nucleation site exceeds the CRSS. At the given temperature, the CRSS for the same slip systems are independent of wire sizes. Therefore, the local stresses σ_l at the nucleation sites are identical for wires of different sizes at the yield point. However, σ_l does not equal to the yield stress σ_{s0}, which is the overall stress averaged over the whole cross-sectional area. While σ_l are the same for wires of different sizes, σ_{s0} decreases with increasing wire size, as shown in Figure 6.6(a).

In addition to the wire size dependence, various researchers have shown dislocation nucleation is also a kinetic process which has rate and temperature dependence (Schuh et al. 2005). The rate effect can be neglected here because we only consider quasistatic processes, i.e., the time is sufficiently long. Suppose the nucleation of a dislocation that requires an activation energy u_a, which is closely related to the unstable stacking fault energy. This energy barrier can be lowered through mechanical work, or be overcome by an appropriate thermal fluctuation, or a combination of both. The probability of such an event in a given volume of material is written as (Schuh et al. 2005)

$$\dot{n} = \dot{n}_0 \cdot \exp\left(-\frac{u_a - \sigma V}{kT}\right),$$
$$(6.15)$$

where the attempt frequency for the event is $\dot{n}_0$ per unit volume, the mechanical work is equal to a stress σ acting on an activation volume V, and the thermal energy is Boltzmann's constant k multiplied by temperature T. Clearly, thermal fluctuation facilitates dislocation nucleation, and less mechanical work is necessitated for dislocation nucleation at higher temperature. Therefore, the yielding stresses are lower at higher temperatures, as shown in Figure 6.6(b).

After yielding, the stress drops precipitously because of the energy dissipation and stress relaxation associated with the dislocation nucleation, as shown in Figure 6.3.

Meanwhile, the dislocation moves along the {111} plane across the wire and forms a twin boundary. Subsequently, the wire enters a phase equilibrium state at Point B, which will be discussed in the next section.

6.3.3 Strain Energy Minimization during Lattice Reorientation

During lattice reorientation, the <110>/{111} and <100>/{100} phases coexist in the wire, separated by a coherent twin boundary. During the deformation, the <110>/{111} phase progressively transform into <100>/{100} phase as the twin boundary sweeps through the wire length. The lattice reorientation is a dissipative process even under the condition of the isothermal quasistatic deformation. In this study, the lattice reorientation process is decomposed into a reversible part and an irreversible part. For the reversible part, we assume the wire goes through a sequence of phase-equilibrium states *smoothly*. The corresponding part of the input mechanical work is stored as strain energy in the wire as one phase transform into another. Nonetheless, the actual transitions between equilibrium states are not smooth because there are barriers associated with lattice-scale defect nucleation (discussed later). Hence, the twin boundary propagation has serrated strain energy landscape with local peaks corresponding to unstable states and local minima corresponding to metastable phase-equilibrium states. The wire is periodically brought to unstable states and then settles in the metastable states after overcoming the barrier. Meanwhile, the related part of input work is dissipated to maintain constant temperatures. Applying the first law of thermodynamics, we have

$$W = \Delta U + Q \tag{6.16}$$

where W is the total input mechanical work, Q is the energy dissipation associated with the irreversible process. ΔU is the increase of strain energy, and

$$\Delta U = U - U_0, \tag{6.17}$$

where U is the strain energy at the phase-equilibrium state during deformation, and U_0 is the initial strain energy of the unstressed <110>/{111} wire. From equation (6.10) and (6.16), we have

$$\sigma = \frac{1}{V_0}\left(\frac{\partial(\Delta U)}{\partial\varepsilon} + \frac{\partial Q}{\partial\varepsilon}\right) = \sigma_0 + \sigma_{\text{dissip}}. \tag{6.18}$$

where σ_0 is the stress component associated with phase-equilibrium states. It is determined by the elastic properties of the two phases. Specifically,

$$\sigma_0 = \frac{1}{V_0}\frac{\partial(\Delta U)}{\partial\varepsilon} = \frac{1}{V_0}\frac{\partial(U-U_0)}{\partial\varepsilon} = \frac{1}{V_0}\frac{\partial U}{\partial\varepsilon}, \tag{6.19}$$

σ_{dissip} is the stress components associated with energy dissipation due to twin boundary propagation . It is given by

$$\sigma_{\text{dissip}} = \frac{1}{V_0}\frac{\partial Q}{\partial\varepsilon}. \tag{6.20}$$

In the following discussions, the reversible and irreversible parts of the lattice reorientation will be investigated individually. First, the governing equation for a single phase-equilibrium state will be derived based on the constrained minimization of strain energies. The reversible smooth transition is obtained by solving these governing equations for a series of phase-equilibrium states. Second, the source and quantification of energy dissipation will be investigated based on a detailed analysis of the transformation mechanism and the associated energy landscape.

6.3.3.1 Smooth Transition of Phase-equilibrium States

1. Kinematics

Consider any given phase-equilibrium state corresponding to a nominal strain ε, the two coexisting phases are separated by a twin boundary, as shown in Figure 6.4. Each phase is elastically stretched. Therefore, the following field equations are satisfied.

$$\varepsilon_i = \frac{du_i}{dx} \quad \text{in each phase,} \tag{6.21}$$

$$u^+ = u^- \quad \text{at the twin boundary.} \tag{6.22}$$

where ε_i is the strain in each phase, i.e., ε_{110} and ε_{100} in <110>/{111} and <100>/{100} phases, respectively. u^+ and u^- denote the limiting values of displacements on the twin interface, the limits being taken from either side of the interface. Equations (6.21) and (6.22) essentially point out that the displacement is continuous within each phase and across the twin interface, but the elastic strains are not necessarily the same in the two phases. Generally, there is a strain jump across the twin interface.

It is important to point out that the total strain ε includes not only the contributions from the elastic strain in each phase (ε_{110} and ε_{100}), but also the transformation strain (ε_{tr}) due to phase transformation. Specifically,

$$\varepsilon = \frac{l - l_0}{l_0}, \quad \text{and} \tag{6.23}$$

$$l = l_{110} + l_{100}. \tag{6.24}$$

where l_0 is the initial total length of the stress-free <110>/{111} wire, l is the current length of the wire, l_{110} and l_{100} are the current length of the <110>/{111} and <100>/{100} phases corresponding to the total nominal strain ε, respectively. At the same time,

$$l_{110} = l_{110}^0 \left(1 + \varepsilon_{110}\right) \tag{6.25}$$

$$l_{100} = l_{100}^0 \left(1 + \varepsilon_{100}\right) \tag{6.26}$$

where l_{110}^0 and l_{100}^0 are the lengths of the <110>/{111} and <100>/{100} phases at their unstressed states, respectively. Another condition needed to be satisfied during lattice reorientation is that the sum of the lengths of the untransformed <110>/{111} phase and

the transformed <110>/{111} phase must equal to the total length of the initial undeformed wire, i.e.,

$$l_{110}^0 + \frac{l_{100}^0}{1+\varepsilon_{tr}} = l_0 \qquad (6.27)$$

where $\varepsilon_{tr} = 0.41$ is the transformation strain associated with the lattice reorientation. It is the same as $\varepsilon_{<110>\to<001>}$ discussed in section 5.3. $\dfrac{l_{100}^0}{1+\varepsilon_{tr}}$ is the length of the transformed <110>/{111} phase calculated from the length of the corresponding <100>/{100} phase.

2. Force balance

At phase-equilibrium states, the stresses in the two phases satisfy the following equations:

$$\frac{d\sigma_i}{dx} = 0 \text{ in each phase, and} \qquad (6.28)$$

$$\sigma_{110}A_{110} = \sigma_{100}A_{100} \text{ at the phase boundary.} \qquad (6.29)$$

where σ_i is the stress in each phase, i.e., σ_{110} and σ_{100} in the <110>/{111} and <100>/{100} phases, respectively. A_{110} is the area of the rhombic cross-section of the <110>/{111} phase, and A_{100} is the area of the square cross-section of the <100>/{100} phase. Equations (6.28) and (6.29) point out that the force is continuous within each phase and across the twin interface. The stress is uniform within each phase but not continuous across the twin interface because the cross-sectional areas of the two phases are not the same. Specifically, $A_{110} > A_{100}$.

3. Constrained strain energy minimization

In energy and variation method, a system at the equilibrium state has the minimum strain energy. Therefore, we can obtain the phase equilibrium states of the wire by minimizing the total strain energy, with the preceding force balance and kinematics

89

equations being satisfied. Specifically, the total strain energy of the wire is composed of the strain energy of each phase and the interface energy.

$$U = \int_{V_{110}} u_{110}\left(\varepsilon_{110}\right) dV + \int_{V_{100}} u_{100}\left(\varepsilon_{100}\right) dV + U_{\text{interface}} \qquad (6.30)$$

The strain energy associated with the twin interface is essentially constant because the configuration of the coherent twin interface remains the same during lattice reorientation. Therefore, the twin interface energy does not affect the strain energy minimization.
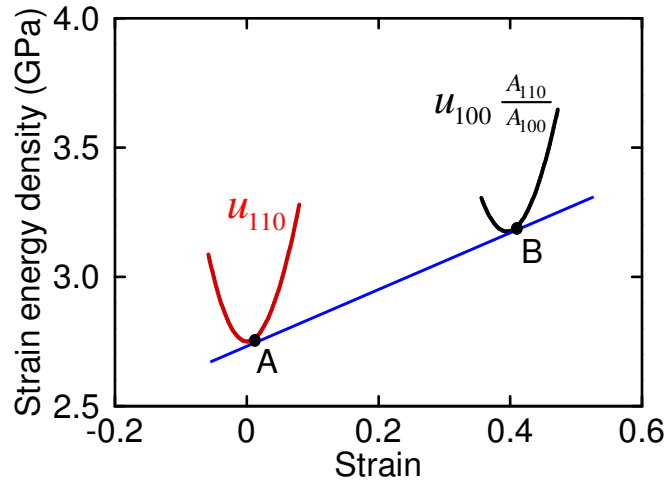
Figure 6.7 Phase equilibrium illustrated by common tangent construction

The constrained energy minimization problem can be illustrated by a common tangent construction between the strain energy density functions of the <110>/{111} and <100>/{100} phases in Figure 6.7, respectively. The tangent points A and B, sharing the comment tangen, have the same stress states because the tangents of strain energy density functions give the stresses at the corresponding tangent points. Therefore, points A and B satisfy the force balance condition, while having the minimum strain energies under the force balance constraints. Consequently, these two tangent points represent the phase-equilibrium states in a binary phase system. Note that in order to compare the forces in the two phases, the strain energy density function of <100>/{100} phase is normalized by the cross-sectional area to account for the difference in cross-sectional areas.
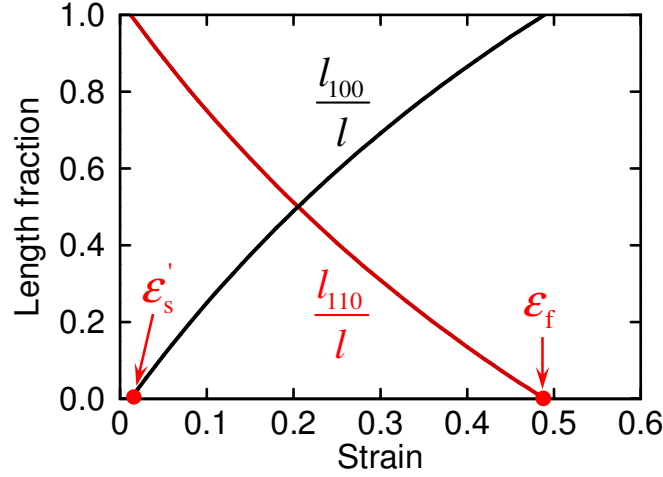
Figure 6.8 The variation of length fractions of the <110>/{111} and <100>/{100} phases during lattice reorientation

　　Solving the constrained energy minimization problems defined by equation (5.4)-(6.30) numerically, we obtain the elastic stresses (σ_{110} and σ_{100}), strains (ε_{110} and ε_{100}), and the length fraction (l_{110}/l and l_{100}/l) of the two phases. Specifically, the stresses and strains of the two phases are constant during lattice reorientation, which can also be seen from the common tangent construction in Figure 6.7. Therefore, the elongation during lattice reorientation solely proceeds with the variation of the length fractions of the two phases, as shown in Figure 6.8. In addition, the length fractions also clearly depict three deformation stages:

(1) Initial elastic deformation of single-phase <110>/{111} wire ($0 \sim \varepsilon_{s}$): $l_{110}/l = 1$ and $l_{100}/l = 0$. Note that actual elastic limit is not $\varepsilon_{s}^{'}$ shown in Figure 6.8, which is predicted by the preceding governing equations for phase-equilibrium states. It is because at the yield point, the wire is not at an equilibrium state but a unstable state. Instead, the actual yield strain ε_{s} is predicted by the dislocation nucleation model described in section 6.3.2.

(2) Lattice reorientation ($\varepsilon_{s} \sim \varepsilon_{f}$): l_{110}/l decreases while l_{100}/l increases with the progress of transformation. The total nominal strain at the completion of lattice

91

reorientation (ε_{f}) corresponds to the state when l_{110}/l is reduced to zero (point C in Figure 6.3).

(3) Elastic deformation of single-phase <100>/{100} wire ($\varepsilon_{\mathrm{f}}\sim$): $l_{110}/l=0$, or $l_{100}/l=1$.

4. The stress component σ_0

With the local stresses obtained from the constrained minimization of strain energies, the stress component σ_e can be derived from the definition by equation (6.19). Specifically, substituting equation (6.30) into equation (6.19), we obtain the stress component σ_0, i.e.,

$$
\begin{aligned}
\sigma_0 &= \frac{1}{V_0}\frac{\partial U}{\partial\varepsilon} \\
&= \frac{1}{V_0}\frac{\partial}{\partial\varepsilon}\left(V_{110}u_{110}+V_{100}u_{100}+U_{\mathrm{interface}}\right) \\
&= \frac{1}{V_0}\left(V_{110}\frac{du_{110}}{d\varepsilon_{110}}\frac{\partial\varepsilon_{110}}{\partial\varepsilon}+V_{100}\frac{du_{100}}{d\varepsilon_{100}}\frac{\partial\varepsilon_{100}}{\partial\varepsilon}\right) \\
&= \left(\frac{V_{110}}{V_0}\frac{\partial\varepsilon_{110}}{\partial\varepsilon}\right)\sigma_{110}+\left(\frac{V_{100}}{V_0}\frac{\partial\varepsilon_{100}}{\partial\varepsilon}\right)\sigma_{100}
\end{aligned}
\tag{6.31}
$$

where $V_0=A_{110}l_0$ is the initial total volume of the wire, $V_{110}=A_{110}l_{110}^0$ and $V_{100}=A_{100}l_{100}^0$ are the volumes of the <110>/{111} and <100>/{100} phases at the unstressed states, respectively. In order to calculate $\dfrac{\partial\varepsilon_{110}}{\partial\varepsilon}$ and $\dfrac{\partial\varepsilon_{100}}{\partial\varepsilon}$, consider a infinitesimal deformation of $d\varepsilon$. The total deformation is the sum of the deformation of the two phases, therefore,

$$
\left(l_{110}^0+l_{100}^0\right)d\varepsilon = l_{110}^0 d\varepsilon_{110}+l_{100}^0 d\varepsilon_{100}.
\tag{6.32}
$$

Also, two phases must satisfy force balance equation (6.29), which can be rewritten in the following form,

$$
\frac{d\sigma_{110}}{d\varepsilon_{110}}d\varepsilon_{110}A_{110} = \frac{d\sigma_{100}}{d\varepsilon_{100}}d\varepsilon_{100}A_{100}.
\tag{6.33}
$$

Solve equations (6.31), (6.32), and (6.33), we obtain

$$\sigma_0 = \lambda_{110}\sigma_{110} + \lambda_{100}\sigma_{100} \tag{6.34}$$

where

$$\lambda_{110} = \frac{l_{110}^0}{l_0} \frac{l_{110}^0 + l_{100}^0}{l_{110}^0 + \left(\dfrac{A_{110}}{A_{100}}\right)\left(\dfrac{d\sigma_{110}}{d\varepsilon_{110}}\Big/\dfrac{d\sigma_{100}}{d\varepsilon_{100}}\right)l_{100}^0} \tag{6.35}$$

and

$$\lambda_{100} = \frac{l_{100}^0}{l_0} \frac{l_{110}^0 + l_{100}^0}{\left(\dfrac{d\sigma_{100}}{d\varepsilon_{100}}\Big/\dfrac{d\sigma_{110}}{d\varepsilon_{110}}\right)l_{110}^0 + \left(\dfrac{A_{110}}{A_{100}}\right)l_{100}^0}. \tag{6.36}$$

At the initiation of lattice reorientation,

$$l_{110}^0 = l_0 \quad \text{and} \quad l_{100}^0 = 0 \tag{6.37}$$

Substituting into equations (6.35) and (6.36) yields

$$\lambda_{110} = 1 \quad \text{and} \quad \lambda_{100} = 0. \tag{6.38}$$

Therefore,

$$\sigma_0 = \sigma_{110}. \tag{6.39}$$

Similarly, at the completion of lattice reorientation,

$$l_{110}^0 = 0 \quad \text{and} \quad l_{100}^0 = l_0\left(1 + \varepsilon_{tr}\right). \tag{6.40}$$

Substituting into equations (6.35) and (6.36) yields

$$\lambda_{110} = 0, \text{ and } \lambda_{100} = \left(1 + \varepsilon_{tr}\right)\left(A_{100}/A_{110}\right). \tag{6.41}$$

Therefore,

$$\sigma_f = \left(1 + \varepsilon_{tr}\right)\left(A_{100}/A_{110}\right)\sigma_{100}. \tag{6.42}$$

From equation (6.29), $\sigma_{110} < \sigma_{100}$ because $A_{110} > A_{100}$. Therefore, σ_0 has the minimum value σ_{110} at the initiation of lattice reorientation, and maximum value $\left(1 + \varepsilon_{tr}\right)\left(A_{100}/A_{110}\right)\sigma_{100}$ at the completion of lattice reorientation. During the lattice reorientation, σ_0 increases gradually as the low stress phase is transformed into high

stress phase. As will be discussed in the next subsection, stress component σ_{dissip} is constant during lattice reorientation. Therefore, the total stress σ increases slowly during lattice reorientation.
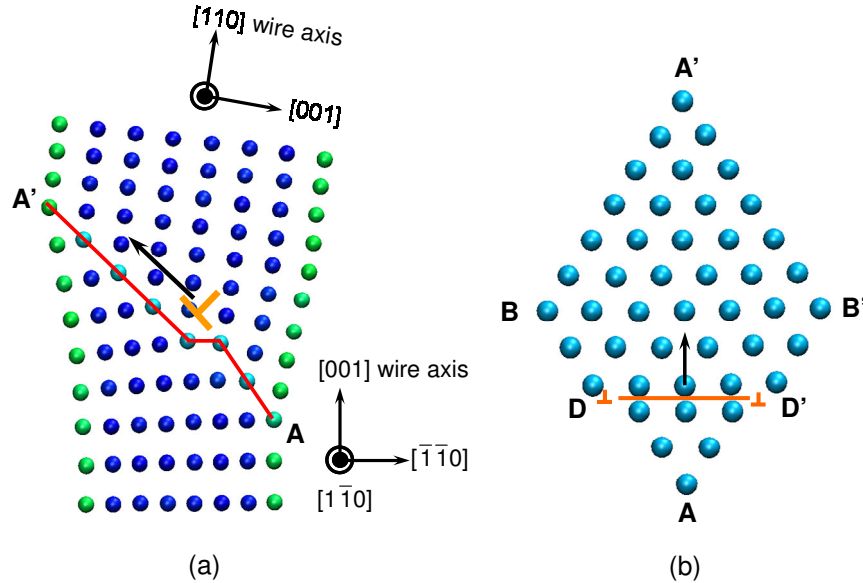
Figure 6.9 Twin boundary propagation through dislocation nucleation, gliding, and annihilation, (a) a side view of details of the {111} twin boundary and the $\frac{1}{6}\{111\}<112>$ Shockley partial dislocation, (b) a perpendicular view of the same {111} twin boundary and the gliding partial dislocation

6.3.3.2 Energy Dissipation

The smooth transition between phase-equilibrium states discussed in the preceding subsection is an ideal process, which is thermodynamically fully reversible without energy dissipation. Nonetheless, the actual lattice reorientation is a dissipative process, no matter how slow the transformation rate is. The energy dissipation is due to the ruggedness of the energy landscape during lattice reorientation, which is associated with the lattice-scale defects nucleation (Truskinovsky and Vainchtein 2003, 2004; Vainchtein and Rosakis 1999; Puglisi and Truskinovsky 2002). Therefore, it is important

to study the detailed lattice-scale transformation mechanism during twin boundary propagation and the associated energy landscape.
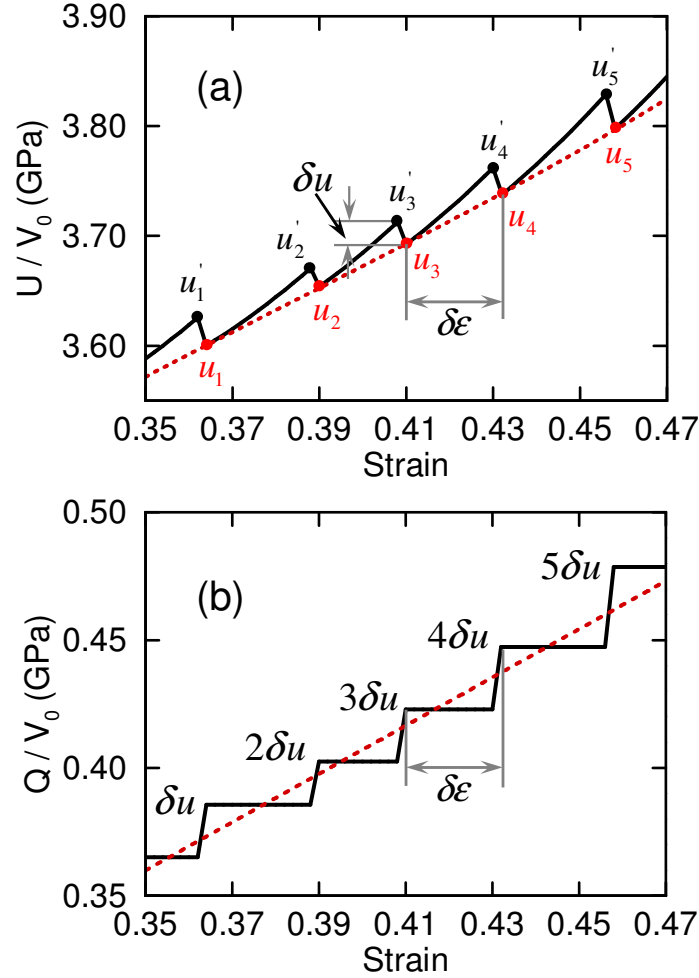
Figure 6.10 (a) the serrated strain energy density curve of a 1.96×1.96 Cu nanowire during lattice reorientation, the local peaks U_i' correspond to the instability upon nucleation of partial dislocation, and the local minima U_i correspond to phase equilibrium states, (b) the step-wise energy dissipation curve

During lattice reorientation, the twin boundary propagates along the wire axis because the atoms on one side go through shear deformation relative to atoms on the other side. However, atoms on one side do not shear simultaneous because the energy

barrier for such a uniform motion is too high. Instead, the shear deformation proceeds through sequential nucleation, gliding, and annihilation of $\frac{1}{6}$<112> Shockley partial dislocations (Abeyaratne and Vedantam 2003), as shown in Figure 6.9. Due to the energy barriers for dislocation nucleation, the strain energy function has a serrated shape with local peaks ($u_i^{'}$) corresponding to unstable states and local minima (u_i) corresponding to metastable states. During lattice reorientation, the wire is periodically brought to unstable states and then settles in the metastable states after overcoming the barrier. Specifically, consider a phase equilibrium state corresponding to local minimum at Point u_1 in Figure 6.10(a). At this state, the twin interface is an atomically smooth {111} plane. The twin boundary propagates in a "stick-slip" manner described below (Vainchtein and Rosakis 1999):

(1) *Elastic stretching*: the strain energy increases along curve $u_1u_2^{'}$ as the wire is stretched.

(2) *Dislocation nucleation*: the wire reaches instability when the strain energy increases to a local energy peak at point $u_2^{'}$. A partial dislocation is then nucleated from one sharp edge (point A in Figure 6.9) on the atomic plane adjacent to the twin plane. The atoms at the nucleation site have lower coordination numbers and thus constitute a weak spot for dislocation nucleation.

(3) *Dislocation gliding*: after the dislocation is nucleated, the dislocation line (DD') forms a step on the twin interface. Hence the twin boundary is not atomically smooth any more. The dislocation step line glides along the long diagonal from point A to A'. Meanwhile, the lattice is relaxed and the strain energy drops precipitously along strain energy curve $u_2^{'}u_2$.

(4) *Dislocation annihilation*: the partial dislocation annihilates when it reaches the sharp edge (indicated by A' in Figure 6.9) on the other side. So far, the twin boundary has advanced an interplanar distance and becomes atomically smooth

96

again. Meanwhile, the wire reaches another metastable phase-equilibrium state with local strain energy minimum at point u_2.

As the wire is further stretched, the process described in step (1)-(4) repeats itself. At each cycle, the wire is brought to an unstable state through elastic stretching and then settles in a local metastable phase-equilibrium state through dislocation nucleation, gliding, and annihilation. At the same time, the twin interface advances by an inter-planar distance between two {111} planes. Consequently, the strain energy curve exhibits a serrated shape with local minima u_i corresponding to metastable states and local maxima u_i' corresponding to unstable states. It is important to point out that dotted line in Figure 6.10(a) illustrates the reversible smooth transition path between metastable states governed by the equations in preceding subsection 6.3.3.1. On the other hand, the serrated strain energy density curve shows the actual change of strain energy density during lattice reorientation. Each time when a dislocation is nucleated and glides across the wire, the strain energy drops precipitously from the local maximum u_i' to minimum u_i, and the strain energy difference $\delta u = u_i' - u_i$ is dissipated through heat transfer or acoustic waves. During the elastic stretching described in step (1), all input energy is stored as strain energy of the wire and there is no energy dissipation. Therefore, the energy dissipation shows a stepwise increase with the strain, as shown in Figure 6.10(b). Without considering the thermal fluctuation, δu is essentially constant because the energy barriers for dislocation nucleation are the same during lattice orientation. Therefore, the total dissipation energy is given by

$$Q = V_0 n \delta u . \tag{6.43}$$

where n is the number of cycles of the dislocation activities described in step (1)-(4). The stepwise change of dissipation Q can also be approximated by a straight line (the dotted line in Figure 6.10(b)), which is given by

$$Q = V_0 \frac{n-0.5}{n} \frac{\delta u}{\delta \varepsilon} \varepsilon \approx V_0 \frac{\delta u}{\delta \varepsilon} \varepsilon . \tag{6.44}$$

where $\delta \varepsilon$ is the strain corresponding to one cycle of dislocation nucleation and annihilation described in step (1)-(4). It is essentially constant. Substituting equation (6.44) into (6.20), we have

$$\sigma_{\text{dissip}} = \frac{\delta u}{\delta \varepsilon} \tag{6.45}$$
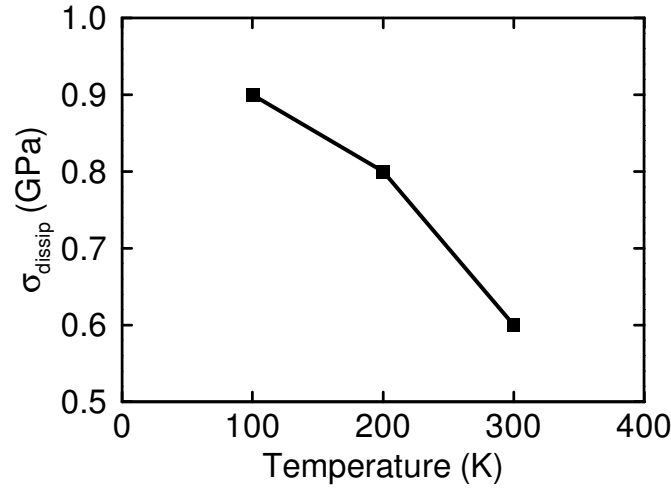
Figure 6.11 The variation of σ_{dissip} with temperatures

Therefore, σ_{dissip} remains constant throughout the lattice reorientation because both δu and $\delta \varepsilon$ are essentially constant. Moreover, σ_{dissip} is proportional to δu, which is closely related to the energy barrier for dislocation nucleation, similar to what is described in subsection 6.3.2. The difference is that dislocation nucleation discussed in subsection 6.3.2 is associated with the *formation* of twin interface and is nucleated from a perfect crystal without initial defects. In contrast, the dislocation nucleation here is associated with the *propagation* of the twin interface and is nucleated near an existing defect, i.e., the twin interface. Therefore, the latter has a lower the energy barrier, but there is a similar temperature effect. From equation (6.15), less mechanical work is necessitated for dislocation nucleation at higher temperatures because thermal fluctuations facilitate to

overcome energy barrier. Therefore, δu and σ_{dissip} are smaller at higher temperatures, as shown in Figure 6.11. This indicates less mechanical work is necessitated to move the twin interface at higher temperatures.

6.3.4 Elastic Deformation of <100>/{100} Phase

At the completion of the lattice reorientation, the wire is transformed into a single <100>/{100} phase. The subsequent deformation is pure elastic deformation without any energy dissipation. Therefore, all the input mechanical work is stored in the wire as strain energy, i.e.,

$$W = U_{100}. \tag{6.46}$$

From equation (6.10) and (6.46), the stress strain relation is given by

$$\sigma = \frac{1}{V_0} \frac{\partial U_{100}}{\partial \varepsilon_{100}} = \frac{\partial u_{100}}{\partial \varepsilon_{100}}. \tag{6.47}$$

where u_{100} is the strain energy density of single-phase <110>/{111} wires in Figure 6.2, ε_{100} is the strain with the reference state being the unstressed <100>/{100} phase. As previously mentioned, the reference state for nominal strain ε is the unstressed <110>/{111} phase. We know that if the length of the unstressed <110>/{111} phase is l_{110}^0, then the length of corresponding <100>/{100} phase is $l_{110}^0 (1 + \varepsilon_{\text{tr}})$. Hence, considering $\varepsilon = \varepsilon_{\text{f}}$ at the beginning of the elastic deformation of <100>/{100} wire, the relation between ε and ε_{100} is given by

$$\varepsilon = \varepsilon_{\text{f}} + \varepsilon_{100}(1 + \varepsilon_{\text{tr}}) \tag{6.48}$$

So far, we have obtained the stress-strain relation for all three deformation stages including the pure elastic deformations of <110>/{111} and <100>/{100} phases and the lattice reorientation in between. Putting them together, we obtain a complete piecewise smooth model for the stress-strain behavior of metal nanowires under the conditions of isothermal quasistatic tensile deformations.

6.4 Comparison to MD Simulations

6.4.1 MD Simulation Methods

The application of the preceding continuum model requires the strain energy density functions for <110>/{111} and <100>/{100} pure phases as inputs. These strain energy functions can be obtained by either MD simulations or analytical method described in section 6.2, providing the bulk and surface elastic constants are known. Here the strain energy density functions are obtained by performing elastic deformations in MD simulations. Specifically, two unit cells are created out of perfect bulk lattice with the same cross-sections as the corresponding phases. Periodical boundary conditions are applied in the axial directions only. First, the unit cells are relaxed under constant zero pressure conditions. Due to the tensile surface stress, the unit cells contract in axial direction and reaches self-equilibrium states, as discussed in section 6.2. Then the previously described displacement-controlled tensile loading is applied on the unit cells until yielding occurs. Suppose there are N atoms in a unit cell and the total internal energy of unit cell obtained from MD simulations is U_i at a given temperature, and the total energy per atom in the bulk is U_b at the same temperature. Then the total strain energy of the unit cell can be calculated by

$$U = U_i - NU_b \tag{6.49}$$

Applying equation (6.49) at each step, we can obtain the strain energy functions for the <110>/{111} and <100>/{100} pure phases within the elastic regime.

With the strain energy functions, we can then apply the continuum model. The model predictions are compared to the stress-strain behaviors of Cu nanowires under isothermal quasistatic tensile deformation obtained from MD simulations. The model predictions show excellent agreement with MD simulation results. They not only capture the major characteristics of the unique behavior due to lattice reorientation, but also account for size and temperature effects of the behavior.
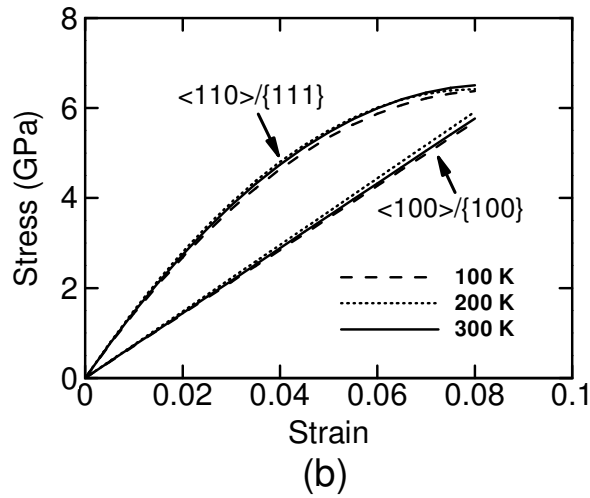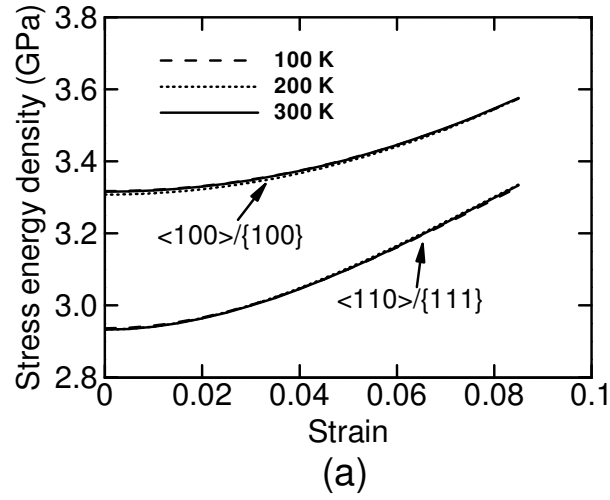
Figure 6.12 The elastic behaviors of single-phase <110>/{111} and <100>/{100} Cu wires with lateral size of 1.96×1.96 nm at temperatures of 100 K, 200 K, and 300 K, respectively, (a) the strain energy density functions at different temperatures, (b) the stress-strain relations at different temperatures

6.4.2 Temperature Effects

The elastic behaviors of single-phase wires are essentially independent of temperatures. As shown in Figure 6.12, the strain energy density functions and stress-strain curves essentially coincide with each other within the considered temperature range

(100 – 300 K). However, MD simulation results show lattice reorientation is temperature dependent. Specifically, both the yield stress σ_{s0} the stress during lattice reorientation decreases with increasing temperatures. This temperature effect can be explained by the model.
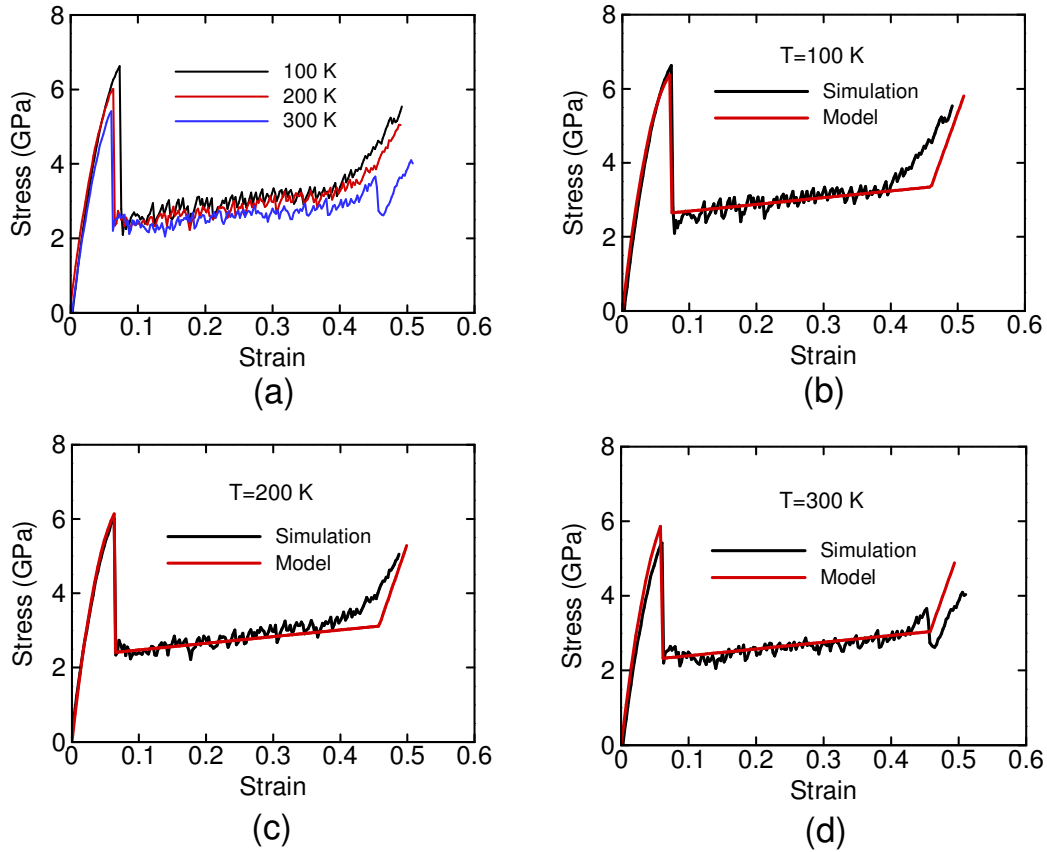
Figure 6.13 Temperature effects: (a) the stress-strain behaviors of a 1.96×1.96 nm <110>/{111} Cu wire at temperatures of 100 K, 200K, and 300 K obtained from MD simulations, figures (b), (c), and (d) show the comparisons of the MD simulation results with the model predictions at T = 100 K, 200K, and 300 K, respectively.

As discussed previously, the stress during lattice reorientation consists of two components: σ_0 associated with the phase equilibrium states and σ_{dissip} associated with energy dissipation. As discussed in subsection 6.3.3.1, σ_0 is primarily determined by the elastic behaviors of the two pure phases. Therefore, it is essentially independent of

temperatures (see Table 6.1) because the elastic behaviors of the pure phases are essentially identical at different temperatures.

The temperature effect is primarily due to the variation of σ_{dissip} with temperatures. Specifically, σ_{dissip} is smaller at higher temperatures because thermal fluctuations facilitate to overcome the energy barrier for dislocation nucleation. For the same reason, the yield stress is lower at higher temperatures. As shown in Figure 6.13, the model prediction capture the temperature effect and are in excellent agreement with MD results at different temperatures.

Table 6.1 Continuum model parameters for a 1.96×1.96 nm Cu nanowire at different temperatures

Temperature	ε_s	σ_{s0} (GPa)	ε_{110}	σ_{110} (GPa)	ε_f	ε_{100}	σ_{100} (GPa)	σ_{dissip} (GPa)
100 K	0.073	6.62	0.0119	1.82	0.46	0.0322	2.29	0.9
200 K	0.061	6.01	0.0112	1.80	0.457	0.0306	2.26	0.8
300 K	0.059	5.41	0.0116	1.81	0.459	0.0317	2.29	0.6

6.4.3 Size Effects

Due to the higher surface-to-volume ratios, smaller wires have higher strain energy densities, as shown in Figure 6.14(a). For the same reason, smaller wires are stiffer than larger wires, which can be seen from the stress-strain relations in Figure 6.14(b). The results of MD simulations regarding single-phase wires are consistent with results of experiments and first principle calculations (Dingreville et al. 2005). Similarly, there are significant size effects in the behavior of <110>/{111} wires with lattice reorientation. Specifically, both the yield stress σ_{s0} and the stresses during lattice reorientation decrease with increasing wire size, see Table 6.2 and Figure 6.15. The model predictions show excellent agreement with MD simulation results for wires of different sizes. Moreover, it also helps to explain why the behavior is size-dependent.
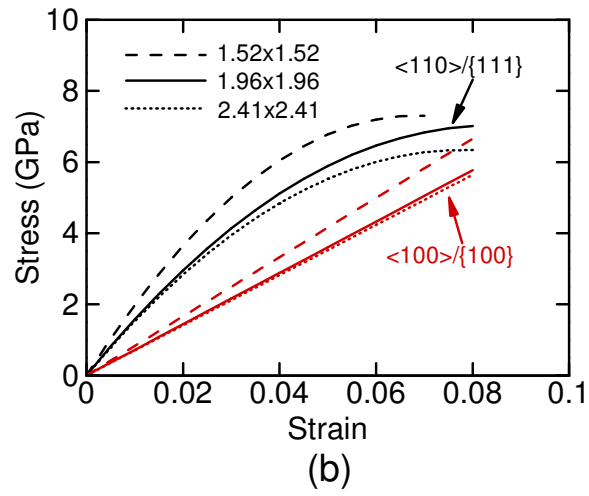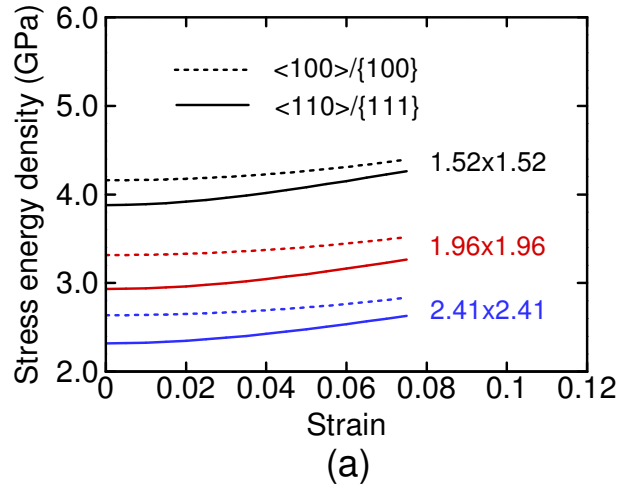
Figure 6.14 The elastic behaviors of single-phase <110>/{111} and <100>/{100} Cu wires of different sizes T=300 K, (a) the strain energy density functions, (b) the stress-strain relations
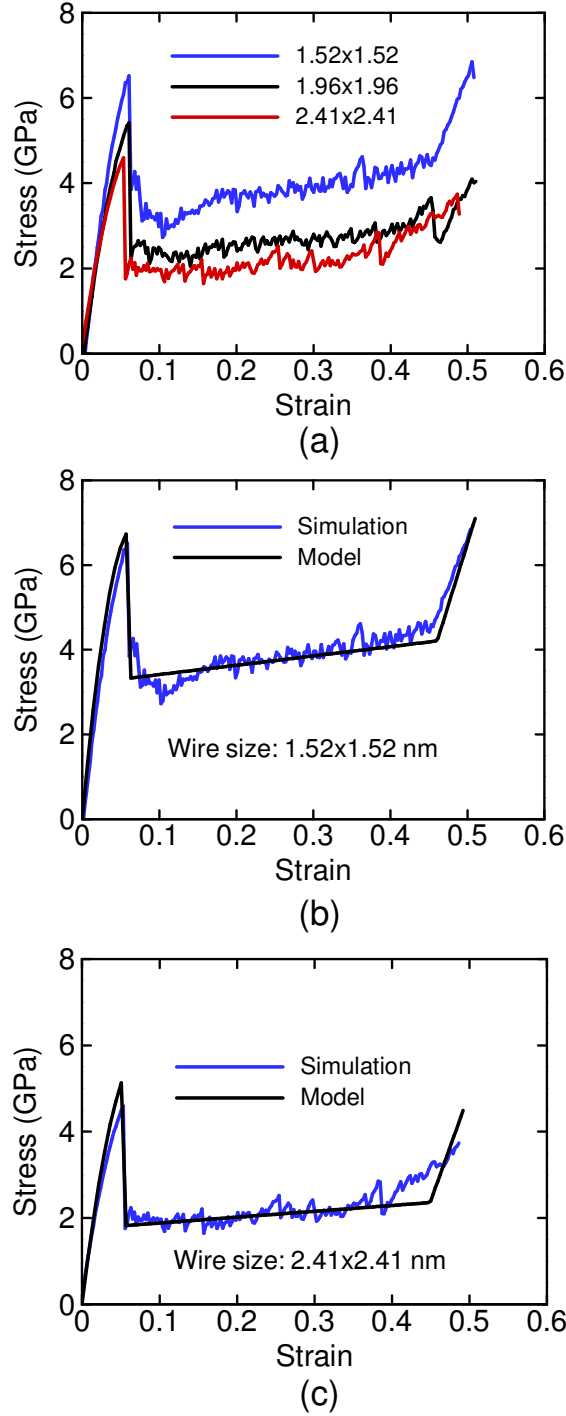
Figure 6.15 Size effects: (a) the stress-strain behaviors of <110>/{111} Cu wires of different sizes at T=300 K obtained from MD simulations, figures (b) and (c) and figure (d) show the comparisons of the MD simulation results with the model predictions for wires of sizes of 1.52×1.52, 1.96×1.96, and 2.41×2.41 nm, respectively.

First, σ_{s0} is closely related to CRSS for the nucleation of the first partial dislocation. Since the activated slip systems are identical in wires of all sizes, the CRSS should be independent of wire size at a given temperature. Therefore, the local yield stress σ_l at the nucleation sites should be independent of wire sizes. However, σ_l is not the same as σ_{s0}, which is the overall stress averaged over the whole cross-section at the yield point. Therefore, for the same σ_l, σ_{s0} is higher in smaller wires because the stress concentration area constitutes a larger portion of the total cross-sectional area.

Table 6.2 Continuum model parameters for Cu wires of different sizes at T = 300 K

Wire size (nm)	ε_s	σ_{s0} (GPa)	ε_{110}	σ_{110} (GPa)	ε_f	ε_{100}	σ_{100} (GPa)	σ_{dissip} (GPa)
1.52×1.52	0.059	6.52	0.0112	2.20	0.459	0.0322	2.68	1.3
1.96×1.96	0.059	5.41	0.0116	1.81	0.459	0.0317	2.29	0.7
2.41×2.41	0.052	4.60	0.0088	1.35	0.449	0.0247	1.74	0.6

Second, the stress component σ_0 at phase-equilibrium is primarily determined by the elastic properties of the single-phase wires. Since both <110>/{111} and <100>/{100} single-phase wires are stiffer at smaller sizes, σ_0 is higher in smaller wires. On the other hand, according to equation (6.45), σ_{dissip} is proportional $\delta u = \delta U / V_0$, where δU is the unit energy dissipation induced by a single dislocation nucleation and annihilation. Since δU is essentially identical in wires of different sizes, σ_{dissip} is inversely proportional to the wire volume. Hence σ_{dissip} is higher in smaller wires due to smaller volumes. Therefore, the stress during lattice reorientation decreases with increasing wire sizes because both components σ_0 and σ_{dissip} decrease with increasing wire sizes.

6.5 Chapter Summary and Insights

A continuum model is developed to characterize the unique behavior of single-crystalline FCC metal nanowires under isothermal quasistatic tensile deformation. This model focuses on the unique lattice reorientation process, which is responsible for a shape memory behavior. The lattice reorientation initiates when the <110>/{111} wire reaches its elastic limit and a dislocation is nucleated. There are two competing slip systems under the loading condition: {111}<110> and {111}<112> slip systems, associated with the nucleation of full dislocation and Shockley partial dislocation, respectively. A CRSS analysis shows that the {111}<112> slip systems is more favored. First, {111}<112> slip systems has higher Schmid factor. Particularly, the Schmid factor for the {111}<110> slip system is zero because the loading direction is perpendicular to the slip direction. Second, atoms at the sharper interfacet edges constitute a weaker spot for the nucleation of partial dislocation. After the nucleation, the partial dislocation glides across the wire and forms a coherent twin interface, separating the <110>/{111} phase and the new <100>/{100} phase. The twin interface then propagates along the wire axis as the lattice reorientation proceeds.

Based on the first law of thermodynamics, the lattice reorientation process is divided into two parts: a reversible smooth transition between metastable phase-equilibrium states superimposed with an irreversible, dissipative twin boundary propagation process. These two parts are studied individually.

The smooth transition between static metastable states is modeled using strain energy functions with multiple local minima. Specifically, at any given strain, the wire adopts the configuration with minimum strain energy while the kinematics constraints and force balance are satisfied. Numerical results show that the stress and strain states in either phase are constant during lattice reorientation. Hence, the elongation of the wire is solely accommodated by the transformation from <110>/{111} to <100>/{100} phase. The force is continuous within each phase and across the phase interface. However, the

107

stresses in the two phases are not the same because of the different cross-sectional areas. The slow increase of total stress during lattice reorientation is due to the increase of volume fraction of the high stress phase.

The dissipative nature of the twin boundary propagation is due to the ruggedness of strain energy curves associated with dislocation nucleation, gliding, and annihilation. Specifically, each time a dislocation is nucleated and annihilated, the difference in the strain energies between the unstable state and phase equilibrium state is dissipated. Furthermore, the dissipation energy increases proportionally to the total strain. Therefore the stress component associated with dissipation is constant at a given temperature. Its magnitude is lower at higher temperatures because thermal fluctuations facilitate dislocation nucleation.

The model predictions show excellent agreement with MD simulation results. They capture the major characteristics of the unique behavior due to lattice reorientation and account for the size and temperature dependence. The temperature dependence is primarily because thermal fluctuations facilitate to overcome the energy barriers for dislocation nucleation. Therefore, the yield stress and the stress during lattice reorientation decrease with increasing temperatures. The size dependence of yield and lattice reorientation is primarily because the elastic behaviors of single-phase wires are size dependent. For both the <110>/{111} and the <100>/{100} wires, smaller wires are stiffer. Therefore, the yield stress and the stress during lattice reorientation decrease with increasing wire sizes.

CHAPTER 7 CONCLUSIONS

This research focuses on the characterization of the structure and mechanical behavior of metal nanowires. Molecular dynamics simulations with EAM interatomic potentials have been carried out. A novel SME and pseudoelastic behavior are discovered in single-crystalline FCC metal (Cu and Ni) nanowires. Upon tensile loading and unloading, these wires can recover elongations of up to 50%, well beyond the recoverable strains of 5-8% typical for most bulk SMAs. Results of atomistic simulations and evidences from experiments show that this phenomenon only exists at the nanometer scale and is associated with a reversible lattice reorientation driven by the high surface-stress-induced internal stresses at the nanoscale. This novel SME exists over a wide range of temperature and is associated with response times on the order of nanoseconds, making the nanowires attractive functional components for a new generation of biosensors, transducers, and interconnects in NEMS

It is found that not all metal wires show shape memory. Only FCC metals with high twinnability (such as Cu, Ni, and Au) show shape memory. On the other hand, FCC metals with low twinnability (such as Al) do not show shape memory. Au wires show a transition of behavior from pseudoelasticity at low temperatures to plasticity at high temperatures. The difference in behavior among wires of different materials is due to two competing deformation mechanisms, i.e., twinning and slip. Specifically, pseudoelastic behavior of Cu and Ni wires is associated with a reversible lattice reorientation through twinning. On the other hand, the irreversible tensile deformation of Al wires is due to crystalline slip. The transitional behavior of Au wires is due to a change in deformation mechanism from twinning at low temperatures to slip at high temperatures.

The novel shape memory behavior only exists at the nanoscale but not in bulk metals. This explains why this novel has not been discovered before because extensive

research on nanowires just started about a decade ago. This size effect is primarily due to three reasons: (i) the small size scales in FCC metals make twinning the favored deformation mechanism, (ii) only at the nanoscale, the surface-stress-induced internal compressive stress is high enough to initiate a spontaneous lattice reorientation without external influence, and (iii) the reversibility of the lattice reorientation process is derived from the unique 1D structure of the nanowires. As their lateral dimensions increase, nanowires become 3D structures. Under such conditions, the interaction and entanglement of twin planes transform the wires into polycrystals and ultimately preclude the occurrence of the lattice reorientation which is the mechanism for the pseudoelasticity at the nanoscale.

Under tensile loading, wires with <110>/{111} configurations transform into a new <100>/{100} configuration through a lattice reorientation process. A temperature-dependent spontaneous lattice reorientation enables wires in the <100>/{100} configuration to revert to the <110>/{111} configuration through heating. This temperature effect leads to an SME in Cu wires and in Au wires at lower temperatures. Specifically, the <110>/{111} configuration is more stable than the <100>/{100} configuration primarily because {111} surfaces have a lower surface energy than that of {100} surfaces. Driven by the high surface-stress-induced internal stresses at the nanoscale, {100} surfaces spontaneously reconstruct into lower energy {111} surfaces as part of the lattice reorientation process to lower the overall free energy. This spontaneous process only occurs above a critical temperature because sufficient thermal energy is required to overcome the energy barrier for initiating the process. For each material, the

critical temperature increases with wire size because the driving force is smaller in larger wires and hence a higher amount of thermal energy is needed.

A micromechanical continuum model is developed for the unique stress-strain behavior of nanowires during quasistatic tensile loading. In the model, the lattice reorientation process is treated as a reversible smooth transition between phase-equilibrium states superimposed with a dissipative twin boundary propagation process. Specifically, the smooth transition between static metastable states is modeled using strain energy functions with multiple local minima, i.e., at any given strain, the wire adopts the configuration with minimum strain energy while the kinematics constraints and force balance are satisfied. It is also illustrated that the dissipative nature of twin boundary propagation is due to the ruggedness of strain energy curves associated with dislocation nucleation, gliding, and annihilation. Specifically, each time a dislocation is nucleated and annihilated, the strain energy difference between the unstable state upon nucleation and phase equilibrium state after annihilation is dissipated through heat transfer. Furthermore, the dissipation energy essentially increases with proportion to the strain. Hence, the stress component associated with dissipation is constant throughout the lattice reorientation process at a given temperature. The model captures the major characteristics of the novel behavior and accounts for the size and temperature dependence, yielding results which are in excellent agreement with MD simulation results.

This research has focused on the analysis of transformation mechanism, driving force, energy barrier, and size and temperature effects, quantification of the large transformation strains, and micromechanical continuum modeling of the behavior. Since this is a completely new phenomenon, continuing research can focus on the following aspects.

(1) A shape memory behavior has been found in Cu, Ni, and Au wires. It is highly likely that similar behavior also exists in nanowires of other metals, especially those metals with high twinnabilities, such as Pt and Pb. MD simulations or experiments should be carried out on these metal nanowires. Accurate interatomic potentials are important in this endeavor. Furthermore, one may even study materials other than metals which traditionally are not regarded as shape memory materials. These materials may exhibit a shape memory behavior through other unique transformation mechanisms existing only at the nanoscale.

(2) This research has primarily focused on the behavior under the quasistatic conditions. However, dynamic response can be very important because the applications of SMAs have been significantly limited by the slow response of most SMAs. Some of our preliminary research has shown that the nanowires have very short response times of the order of nanoseconds because the wire dimension is extremely small and the barrier for phase boundary propagation is low. This makes the shape memory nanowires promising materials for building high peed sensors, actuators, and even computer chips. More research should be done to study the lattice reorientation under dynamic conditions, such as the relation between the driving force and the propagation speed of twin boundaries and the inertia effect during the propagation.

(3) The lattice reorientation can be induced by either unloading or heating. However, it is difficult to precisely control the stress or temperature of nanowires because of their small sizes. Recent research reveals that surface charges can change the surface stress and induce macroscopic deformation of the order of millimeters in nanoporous gold (Weissmüller et al. 2003; Kramer et al. 2004). Since the spontaneous lattice reorientation is driven by surface-stress-induced internal stresses, it is possible to use electric charges to control the initiation of the transformation. Compared to stress and temperature, surface charges are much

easier to control. Therefore, further research should be carried out on the quantitative relation between surface charges and surface stresses. The results can be important for applications of shape memory nanowires.

REFERENCES

Abeyaratne, R., K. Bhattacharya, et al., Eds. (2001). <u>Strain-energy functions with multiple local minima:modeling phase transformations using finite thermoelasticity</u>. Nonlinear elasticity: Theory and applications, Cambridge Univ. Press.

Abeyaratne, R. and S.-J. Kim (1994). "A one-dimenional continuum model for shape-memory alloys " <u>International Journal of Solids and Structures</u> **31**: 2229-2249.

Abeyaratne, R. and J. K. Knowles (1990). "On the driving traction acting on a surface of strain discontinuity in a continuum." <u>Journal of the Mechanics and Physics of Solids</u> **38**(3): 345-360.

Abeyaratne, R. and J. K. Knowles (1991). "Kinetic relations and propagation of phase boundaries in solids." <u>Arch. Rational. Mech. Analysis</u> **114**: 119-154.

Abeyaratne, R. and J. K. Knowles (1993). "A continuum model of a thermoelastic solid capable of understanding phase transitions " <u>Journal of the Mechanics and Physics of Solids</u> **41**: 541-571.

Abeyaratne, R. and S. Vedantam (2003). "A lattice-based model of the kinetics of twin boundary motion." <u>Journal of the Mechanics and Physics of Solids</u> **51**: 1675-1700.

Arnold, M. S., P. Avouris, et al. (2003). "Field-Effect Transistors Based on Single Semiconducting Oxide Nanobelts." <u>J. Phys. Chem. B </u>**107**: 659-663.

Ball, J. M. and R. D. James (1987). "Fine phase mixtures as minimizers of energy." <u>Archives of Rational Mechanics and Analysis</u> **100**: 13-52.

Balluffi, R. W. (1978). <u>Journal of Nuclear Materials</u> **69&70**: 240.

Barrett, C. S. (1976). "Transformations at Low Temperatures." <u> Transactions of the Japan Institute of Metals</u> **17**(8): 465-475.

Baskes, M. I. (1992). "Modified embedded-atom method potentials for cubic materials and impurities." <u>Phys. Rev. B</u> **46**: 2727-2742.

Bekker, A. and L. C. Brinson (1997). "Thermo-induced transformation in a prestressed 1-D SMA polycrystalline body] phase diagram kinetics approach." <u>Journal of the Mechanics and Physics of Solids</u> **45**: 949-988.

Bertotti, G. (1996). "Energetic and Thermodynamic Aspects of Hysteresis." <u>Physical Review Letters</u> **76**(10): 1739-1742.

Bhadeshia, H. K. D. H. (2001). <u>Worked Examples in the Geometry of Crystals</u>. London, the Institute of Materials.

Bhattacharya, K., S. Conti, et al. (2004). "Crystal symmetry and the reversibility of martensitic transformations." <u>Nature</u> **428**: 55-59.

Bilalbegović, G. (1998). "Structure and stability of finite gold nanowires." <u>Physical Review B</u> **58**: 15412-5.

Bilalbegović, G. (2000). "Metallic nanowires: multi-shelled or filled?" <u>Comput. Mater. Sci.</u> **18**: 333.

Bilalbegović, G. (2001). "Multi-shell gold nanowires under compression." <u>Journal of Physics: Condensed Matter</u> **13**: 11531-9.

Binnig, G. K., H. Rohrer, et al. (1984). "Real-space observation of the reconstruction of Au(100)." <u>Surf. Sci.</u> **144**: 321-335.

Bowles, J. S. and J. K. Mackenzie (1954a). "The crystallography of martensite transformation I." <u>Acta Metallurgica</u> **2**: 129-137.

Bowles, J. S. and J. K. Mackenzie (1954b). "The crystallography of martensite transformation II." <u>Acta Metallurgica</u> **2**: 138-147.

Büttgenbach, S., S. Bütefish, et al. (2001). "Shape memory microactuators." <u>Microsystem Technologies</u> **7**: 165-170.

Cahn, R. W. (1995). "Metallic rubber bounces back." <u>Nature</u> **374**: 120-121.

Carter, C. B. and I. L. F. Ray (1977). <u>Philosophical Magazine</u> **35**: 189.

Clements, K. (2003). Wireless technique for microactivation. US, Technology Innovations, LLC**:** 6.

Comini, E., G, G. S. Faglia, et al. (2002). "Stable and highly sensitive gas sensors based on semiconducting oxide nanobelts." <u>Applied Physics Letters</u> **81**(10): 1869-1871.

Cui, Y., Q. Wei, et al. (2001). "Nanowire Nanosensors for Highly Sensitive and Selective Detection of Biological and Chemical Species." <u>Science</u> **293**(5533): 1289.

Daw, M. S. and M. I. Baskes (1984). "Embedded-atom method: derivation and application to impurities, surfaces, and other defects in Metals." <u>Physical Review B (Condensed Matter)</u> **29**(12): 6443-53.

Daw, M. S., S. M. Foiles, et al. (1993). "The embedded-atom method: a review of theory and applications." <u>Material Science Reports</u> **9**(7-8): 251-310.

Diao, J., K. Gall, et al. (2003). "Surface-stress-induced Phase Transformation in Metal Nanowires." Nature Materials **2**: 656-660.

Diao, J., K. Gall, et al. (2004). "Surface Stress Driven Reorientation of Gold Nanowires." Physical Review B **70**: 075413.

Dingreville, R., J. Qu, et al. (2005). "Surface free energy and its effect on the elastic behavior of nano-sized particles, wires and films." Journal of the Mechanics and Physics of Solids **53**: 1827-1854.

Duan, X., Y. Huang, et al. (2003a). "Single-nanowire electrically driven lasers." Nature **421**: 241 - 245.

Duan, X., Y. Huang, et al. (2003b). "Indium phosphide nanowires as building blocks for nanoscale electronic and optoelectronic devices." Nature **409**: 66-69.

Dumitrica, T., M. Hua, et al. (2006). "Symmetry-, time-, and temperature-dependent strength of carbon nanotubes." Proceedings of the National Academy of Sciences of the United States of America **103**(16): 6105-6109.

Falk, F. (1983). "Ginzburg-Landau theory of static domain walls in shape-memory alloys." Z. Physik B-Condensed Matter **51**: 177-185.

Falvo, M. R., G. J. Clary, et al. (1997). "Bending and buckling of carbon nanotubes under large strain." Nature **389**: 582-584.

Field, D. P., B. W. True, et al. (2004). "Observation of twin boundary migration in copper during deformation." Materials Science and Engineering A **372**: 173-179.

Fiorentini, V., M. Methfessel, et al. (1993). "Reconstruction Mechanism of fcc Transition Metal (001) Surfaces." Physical Review Letters **71**(7): 1051-1054.

Fischer, F. D. and K. Tanaka (1992). "A micromechanical model for the kinetics of martensitic transformation." International Journal of Solids and Structures **29**: 1723-1728.

Foiles, S. M. (2005). EAM potential for Au.

Foiles, S. M., M. I. Baskes, et al. (1986). "Embedded-atom-method Functions for the fcc Metals Cu, Ag, Ni, Pd, Pt, and Their Alloys." Physical Review B **33**(12): 7983-7991.

Gall, K., J. Diao, et al. (2004). "The strength of gold nanowires." Nano Letters **4**(12): 2431-2436.

Gao, T., G. Meng, et al. (2002). "Electrochemical synthesis of copper nanowires." <u>J. Phys.: Condens. Matter</u> **14**: 355-63.

Gilbertson, R. G. and J. D. Busch (1996). "A survey of micro-actuator technologies for future spacecraft missions " <u>The Journal of The British Interplanetary Society</u> **49**: 129-138.

González, J. C., V. Rodrigues, et al. (2004). "Inication of unusual pentagonal structures in atomic-size Cu nanowires." <u>Physical Review Letters</u> **93**(12): 126103-1.

Gross, V. A. (2003). <u>Theoretical Surface Science - A Microscopic Perspective</u>. New York, Springer.

Gülseren, O., F. Ercolessi, et al. (1998). "Nanocrystalline structures of ultrathin unsupported nanowires." <u>Physical Review Letters</u> **80**: 3775-3778.

Gutie´rrez, G. and B. Johansson (2002). "Molecular dynamics study of structural properties of amorphous Al2O3." <u>Physical Review B</u> **65**: 104202):1-9.

Hasmy, A. and E. Medina (2002). "Thickness induced structural transition in suspended fcc metal nanofilms." <u>Physical Review Letters</u> **88**(9): 096103.

Hertzberg, R. W. (1989). <u>Deformation and Fracture Mechanics of Engineering Materials</u>. New York, Wiley.

Hong, B. H., S. C. Bae, et al. (2001). "Ultrathin single-crystalline silver nanowire arrays formed in an ambient solution phase." <u>Science</u> **294**: 348-351.

Hove, M. A. V., R. J. Koestner, et al. (1981). "The surface reconstructions of the (100) crystal faces of Iridium, Platinum and Gold:: I. Experimental Observations and Possible Structural Models." <u>Surf. Sci.</u> **103**: 189-217.

Huang, M. H., S. Mao, et al. (2001). "Room-temperature ultraviolet nanowire nanolas." <u>Science</u> **292**(5523): 1897-1899.

Huang, M. S. and L. C. Brinson (1998). "A multivariant model for single crystal shape memory alloy behavior." <u>J. Mech. Phys. Solids.</u> **46**(8): 1379-1409.

Humphrey, W., A. Dalke, et al. (1996). "VMD - visual molecular dynamics." <u>J. Molec. Graphics</u> **14**(1): 33-38.

Iijima, S. and L.-C. Qin (2002). "Electron microscopic characterization of silver nanowire arrays." <u>Science</u> **296**: 611-612.

Ikeda, H., Y. Qi, et al. (1999). "Strain rate induced amorphization in metallic nanowires." <u>Physical Review letters</u> **82**(14): 2900-3.

Ivshin, Y. and T. J. Pence (1994). "A constitutive model for hysteretic phase transition behavior." <u>Int. J. Eng. Sci.</u> **32**: 681-704.

Kang, J. W. and H. J. Hwang (2002). "Pentagonal multi-shell Cu nanowires." <u>Journal of Physics: Condensed Matter</u> **14**: 2629-2636.

Kang, J. W., J. J. Seo, et al. (2002). "Structures of ultrathin copper nanotubes." <u>Journal of Physics: Condensed Matter</u> **14**: 8997-9005.

Kelchner, C. L., S. J. Plimpton, et al. (1998). "Dislocation nucleation and defect structure during surface indentation." <u>Physical Review B (Condensed Matter)</u> **58**(17): 11085-8.

Kondo, Y., Q. Ru, et al. (1999). "Thickness induced structural phase transition of gold nanofilm." <u>Physical Review Letters</u> **82**(4): 751-754.

Kondo, Y. and K. Takayanagi (1997). "Gold nanobridge stabilized by surface structure." <u>Physical Review Letters</u> **79**(18): 3455-3458.

Kondo, Y. and K. Takayanagi (2000). "Sythesis and Characterization of Helical Multi-Shell Gold Nanowires." <u>Science</u> **289**(5479): 606.

Konishi, Y., M. Motoyama, et al. (2003). "Electrodeposition of Cu nanowire arrays with a template." <u>Journal of Electroanalytical Chemistry</u> **559**: 149-153.

Kramer, D., R. N. Viswanath, et al. (2004). "Surface-stress induced macroscopic bending of nanoporous gold cantilevers." <u>Nano Letters</u> **4**(5): 793-796.

Kuekes, P. J., D. R. Stewart, et al. (2005). "The crossbar latch: Logic value storage, restoration, and inversion in crossbar circuits." <u>Journal of Applied Physics</u> **97**: 034301-(1-5).

Landman, U., R. N. Barnett, et al. (1997). "Nanowires: size evolution, reversibility, and one-atom contacts." <u>Zeitschrift für Physik D</u> **40**: 282-287.

Landman, U., W. D. Luedtke, et al. (1990). "Atomistic Mechanisms and Dynamics of Adhesion, Nanoindentation, and Fracture." <u>Science</u> **248**(4954): 454-461.

Landman, U., W. D. Luedtke, et al. (1996). "Reversible manipulations of room temperature mechanical and quantum transport properties in nanowire junctions." <u>Physical Review Letters</u> **77**(7): 1362-1365.

Leeuwen, J. M. J. v., J. Groeneveld, et al. (1959). "New method for the calculation of the pair correlation function. I." <u>Physica</u> **25**: 792-808.

Liang, C. and C. A. Rogers (1990). "One-dimensional thermomechanical constitutive relations for shape memory materials." J. of Intell. Mater. Syst. and Struct. **1**: 207-234.

Liang, W., V. Tomar, et al. (2003). Simulation and Modeling of Mechanical Deformation of Nanowires. Nanowires and Nanobelts : Materials, Properties and Devices. Z. L. Wang. New York, Springer**:** 125-155.

Liang, W. and M. Zhou (2004). "Response of copper nanowires in dynamic tensile deformation." Journal of Mechanical Engineering Science **218**(6): 599-606.

Liang, W. and M. Zhou (2005). "Pseudoelasticity of Single Crystalline Cu Nanowires through Reversible Lattice Reorientations." Journal of Engineering Materials and Technology **127**(4): 423-433.

Liang, W. and M. Zhou (2006). "Atomistic simulations reveal shape memory of fcc metal nanowires." Physical Review B **73**: 115409.

Liang, W., M. Zhou, et al. (2005). "Shape memory effect in Cu nanowires." Nano Letters **5**(10): 2039-2043.

Lieber, C. M. (2003). "Nanoscale science and technology: Building a big future from small things." MRS Bulletin **28**(7): 486-491.

Lieberman, D. S., M. S. Wechsler, et al. (1955). "Cubic to Orthorhombic Diffusionless Phase Change - Experimental and Theoretical Studies of AuCd." Journal of Applied Physics **26**(4): 473-484.

Liu, Z. and Y. Bando (2003). "A Novel Method for Preparing Copper Nanorods and Nanowires." Advanced Materials **15**(3): 303-305.

Liu, Z., Y. Yang, et al. (2003). "Synthesis of Copper Nanowires via a Complex-Surfactant-Assisted Hydrothermal Reduction Process." Journal of Physical Chemistry B **107**: 12658-12661.

Lu, S. and B. Panchapakesan (2004). A platinum nanowire actuator: Metallic nano-muscles. 2004 International Conference on MEMS, NANO and Smart Systems, ICMENS 2004, 2004, p 36-40, Banff, Alta., Canada.

Lu, Z. K. and G. J. Weng (1997). "Martensitic transformation and stress-strain relations of shape-memory alloys." Journal of Mechanics and Physics of Solids **45**: 1905-1928.

Meyers, C. (1984). Mechanical Metallurgy Principle and Applications, Printice-Hall Inc.

Mishin, Y., D. Farkas, et al. (1999). "Interatomic potentials for monoatomic metals from experimental data and *ab initio* calculations." Physical Review B **59**(5): 3393-3407.

Mishin, Y., M. J. Mehl, et al. (2001). "Structural stablility and lattice defects in copper: ab initio, tight-binding, and embedded-atom calculations." Physical Review B **63**: 224106.

Molares, M. E. T., V. Buschmann, et al. (2001). "Single-Crystalline Copper Nanowires Produced by Electrochemical Deposition in Polymeric Ion Track Membranes." Adv. Mater. **13**: 62-65.

Murr, L. E. (1975). Interfacial Phenomena in Metals and Alloys. Reading, MA, Addison-Wesley.

Nakanishi, N. (1980). "Elastic Constants as They Relate to Lattice Properties and Martensite Formation." Progress in Materials Science **24**: 143-265.

Ohnishi, H., Y. Kondo, et al. (1998). "Quantized conductance through individual rows of suspended gold atoms." Nature **395**: 781.

Ölander, A. (1932). "An electrochemical investigation of solid cadmium-gold alloys." J. Am. Chem. Soc. **56**: 3819-3833.

Ooi, N. E. K. (2005). Theoretical study of aluminum-ceramic interfaces, ARIZONA STATE UNIVERSITY. **Ph.D.**

Otsuka, K. and T. Kakeshita (February 2002). "Science and Technology of Shape-Memory Alloys: New Developments." MRS Bulletin: 91-98.

Otsuka, K. and X. Ren (1999). "Recent developments in the research of shape memory alloys." Intermetallics **7**: 511-528.

Otsuka, K. and C. M. Wayman, Eds. (1998). Shape Memory Materials. New York, Cambridge University Press.

Park, H. S. and J. A. Zimmerman (2005). "Modeling inelasticity and failure in gold nanowires." Physical Review B **72**: 054106.

Park, H. S. and J. A. Zimmerman (2006). "Stable nanobridge formation in <110> gold nanowires under tensile deformation." Scripta Materialia **54**(6): 1127-1132.

Patolsky, F. and C. M. Lieber (2005). "Nanowire nanosensors." Materials Today **8**(4): 20-28.

Payne, M. C., M. P. Teter, et al. (1992). "Iterative minimisation techniques for ab initio total-energy calculations: molecular dynamics and conjugate gradients." <u>Reviews of Modern Physics</u> **64**: 1045–1097.

Plimpton, S. J. (1995). "Fast Parallel Algorithms for Short-Range Molecular Dynamics." <u>J. Comp. Phys.</u> **117**: 1-19.

Puglisi, G. and L. Truskinovsky (2002). "A mechanism for transformational plasticity." <u>Continuum mechanics of thermodynamics</u> **14**: 437-457.

Raniecki, B., C. Lexcellent, et al. (1992). "Thermodynamic models of pseudoelastic behaviour of shape memory alloys." <u>Arch. Mech.</u> **44**(3): 261-284.

Rautioaho, R. H. (1982). <u>Phys. Status Solidi B</u> **112**: 83.

Rego, L. G. C., A. R. Rocha, et al. (2003). "Role of structure evolution in the quantum conductance behavior of gold nanowires during stretching." <u>Physical Review B</u> **67**: 045412.

Ren, X. and K. Otsuka (1997). "Origin of rubber-like behavior in metal alloys." <u>Nature</u> **389**: 579-582.

Rice, J. R. (1992). "Dislocation nucleation from a crack tip: an analysis based on the Peierls concept." <u>Journal of the Mechanics and Physics of Solids</u> **40**(2): 239-271.

Rittner, J. D. and D. N. Seidman (1996). "<110> symmetric tilt grain-boundary structures in fcc metals with low stacking-fault energies." <u>Physical Review B</u> **54**(10): 6999-7015.

Rodrigues, V., J. Bettini, et al. (2002). "Quantum conductance in silver nanowires: Correlation between atomic structure and transport properties." <u>Physical Review B</u> **65**: 153402.

Rodrigues, V. and D. Ugarte (2002). "Metal nanowires: atomic arrangement and electrical transport properties." <u>Nanotechnology</u> **13**: 404-408.

Rodrigues, V. and D. Ugarte (2003). Structural Study of Metal Nanowires. <u>Nanowires and Nanobelts : Materials, Properties and Devices</u>. Z. L. Wang. New York, Springer**:** 177-209.

Rubio-Bollinger, G., S. R. Bahn, et al. (2001). "Mechanical Properties and Formatioin Mechanisms of a Wire of Single Gold Atoms." <u>Physical Review Letters</u> **87**(2): 026101-1~4.

Sato, Y. and K. Tanaka (1988). "Estimation of energy dissipation in alloys due to stress!induced martensitic transformation." <u>Res. Mech.</u> **23**: 381-393.

Sauer, G., G. Brehm, et al. (2002). "Highly ordered monocrystalline silver nanowire arrays." Journal of Applied Physics **91**(5): 3243-3247.

Schuh, C. A., J. K.Mason, et al. (2005). "Quantitative insight intodislocation nucleation fromhigh-temperature nanoindentation experiment." Nature Materials **4**: 617-621.

Shin, D. D., K. P. Mohanchandra, et al. (2004). "High frequency actuation of thin film NiTi." Sensors and Actuators A **111**: 166-171.

Siegel, D. J., J. Louis G. Hector, et al. (2001). "First-principles study of metal–carbide/nitride adhesion: Al/VC vs. Al/VN." Acta Materialia **50**(3): 619-631.

Stalder, A. and U. Durig (1995). "Study of yielding mechanics in nanometer-sized Au contacts." Applied Physics Letters **68**(5): 637-9.

Stobbs, W. M. and C. H. Sworn (1971). Philosophical Magazine **24**: 1365.

Streitz, F. H., R. C. Cammarata, et al. (1994). "Surface-stress effects on elastic properties. I. Thin metal films." Phys. Rev. B **49**: 10699-10706.

Swygenhoven, H. V., P. M. Derlet, et al. (2004). "Stacking fault energies and slip in nanocrystalline metals." Nature Materials **3**: 399-403.

Tadmor, E. B. and N. Bernstein (2004). "A first-principle measure for the twinnability of FCC metals." Journal of the Mechanics and Physics of Solids **52**(11): 2507-2519.

Tadmor, E. B. and S. Hai (2003). "A Peierls criterion for the onset of deformation twinning at crack tips." Journal of the Mechanics and Physics of Solids **51**: 765-793.

Takeuchi, O., C. T. Chan, et al. (1991). "Reconstruction of the (100) surfaces of Au and Ag." Physical Review B **43**: 14363–14370.

Terabe, K., T. Hasegawa, et al. (2005). "Quantized conductance atomic switch." Nature **433**: 47-50.

Trimble, T. M., R. C. Cammarata, et al. (2003). "The stability of fcc (111) metal surfaces." Surf. Sci. **531**: 8-20.

Trushin, O., E. Granato, et al. (2002). "Minimum energy paths for dislocation nucleation in strained epitaxial layers." Physical Review B **65**: 241408-1~4.

Truskinovsky, L. and A. Vainchtein (2003) "Peierls-Nabarro landscape for martensitic phase transitions." Physical Review B **67**(17): 172103-1-4

Truskinovsky, L. and A. Vainchtein (2004) "The origin of nucleation peak in transformational plasticity", Journal of the Mechanics and Physics of Solids **52**(6): 1421-1446

Vainchtein, A. and P. Rosakis (1999). "Hysteresis and stick-slip motion of phase boundaries in dynamic models of phase transitions." Journal of Nonlinear Science **9**: 697-719.

Vitos, L., A. V. Ruban, et al. (1998). "The surface energy of metals." Surface Science **411**: 186-202.

Walter, E. C., R. M. Penner, et al. (2002). "Sensors from electrodeposited metal nanowires." Surface and Interface Analysis **34**: 409-412.

Wang, B., S. Yin, et al. (2001). "Novel Structures and Properties of Gold Nanowires." Physical Review Letters **86**(10): 2046-9.

Wang, J., Y. L. Fan, et al. (1999). "Surface relaxation and stress of fcc metals: Cu, Ag, Au, Ni, Pd, Pt, Al and Pb." Modeling Simul. Mater. Sci. Eng. **7**: 189-206.

Wang, J., H. Huang, et al. (2004a). "Diffusion barriers on Cu surfaces and near steps." Modelling Simul. Mater. Sci. Eng. **12**: 1209-1225.

Wang, J., M. Tian, et al. (2004b). "Microtwinning in Template-Synthesized Single-Crystal Metal Nanowires." J. Phys. Chem. B **108**: 841-845.

Wang, Y., J. Yang, et al. (2004c). "Thermal expansion of Cu nanowire arrays." Nanotechnology **15** 1437-1440.

Wang, Z. L., R. P. Gao, et al. (2000). "Surface Reconstruction of the Unstable {110} Surface in Gold Nanorods." Journal of Physical Chemistry B **104**: 5417-5420.

Weissmüller, J., R. N. Viswanath, et al. (2003). "Charge-Induced reversible strain in a metal." Science **300**(5617): 312.

Westmacott, K. H. and R. L. Peck (1971). Philosophical Magazine **23**: 611.

Wu, Y., J. Xiang, et al. (2004). "Sing-crystal Metallic Nanowires and Metal/Semiconductor Nanowire Heterostructures." Nature **430**: 61-64.

Yakobson, B. I., C. J. Brabec, et al. (1996). "Nanomechanics of carbon nanotubes: Instabilities beyond linear response." Physical Review Letters **76**(14): 2511-2514.

Yang, P. (2002). "Wired for success." Nature **419**: 553-555.

Yanson, A. I., G. R. Bollinger, et al. (1998). "Formation and manipulation of a metallic wire of single gold atoms." <u>Nature</u> **395**: 783-785.

Zhang, J. M., F. Ma, et al. (2004). "Calculations of the Surface Energy of FCC Metals with Modified Embedded-Atom Method." <u>Applied Surface Science</u> **229**: 34-42.

Zhong, Z., D. Wang, et al. (2003). "Nanowire Crossbar Arrays as Address Decoders for Integrated Nanosystems." <u>Science</u> **302**(5649): 1377.

Zimmerman, J. A., H. Gao, et al. (2000). "Generalized stacking fault energies for embedded atom FCC metals." <u>Modelling Simulation of Materials Science and Engineering</u> **8**: 103-115.